Conservative Chaotic Systems and Conservative-Chaos-Based Engineering Applications

Lead Guest Editor: Shijian Cang
Guest Editors: Zenghui Wang, Yue Li, and Yanxia Sun

Conservative Chaotic Systems and Conservative-Chaos-Based Engineering Applications

Conservative Chaotic Systems and Conservative-Chaos-Based Engineering Applications

Lead Guest Editor: Shijian Cang
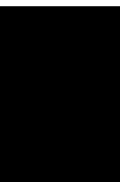Guest Editors: Zenghui Wang, Yue Li, and Yanxia Sun

Contents

WILEY | Hindawi

Research Article

A Simple Conservative Chaotic Oscillator with Line of Equilibria: Bifurcation Plot, Basin Analysis, and Multistability

Dhinakaran Veeman [iD],[1] **Hayder Natiq** [iD],[2] **Ahmed M. Ali Ali** [iD],[3] **Karthikeyan Rajagopal** [iD],[4] **and Iqtadar Hussain** [iD][5]

[1]*Centre for Additive Manufacturing, Chennai Institute of Technology, Chennai, India*
[2]*Information Technology Collage, Imam Ja'afar Al-Sadiq University, Baghdad 10001, Iraq*
[3]*Department of Electronics Techniques, Babylon Technical Institute, Al-Furat Al-Awsat Technical University, Babylon 51001, Iraq*
[4]*Centre for Nonlinear Systems, Chennai Institute of Technology, Chennai, India*
[5]*Mathematics Program, Department of Mathematics, Statistics and Physics, College of Arts and Sciences, Qatar University, Doha 2713, Qatar*

Correspondence should be addressed to Karthikeyan Rajagopal; rkarthiekeyan@gmail.com

Here, a novel conservative chaotic oscillator is presented. Various dynamics of the oscillator are examined. Studying the dynamical properties of the oscillator reveals its unique behaviors. The oscillator is multistable with symmetric dynamics. Equilibrium points of the oscillator are investigated. Bifurcations, Lyapunov exponents (LEs), and the Poincare section of the oscillator's dynamics are analyzed. Also, the oscillator is investigated from the viewpoint of initial conditions. The study results show that the oscillator is conservative and has no dissipation. It also has various dynamics, such as equilibrium point and chaos. The stability analysis of equilibrium points shows there are both stable and unstable fixed points.

1. Introduction

Chaotic dynamics have been an interesting topic for many years. The chaotic Lorenz oscillator was proposed to model the atmosphere in 1963 [1]. There was a hypothesis that the chaotic attractors are associated with saddle equilibria. So, many well-known chaotic oscillators contain a saddle equilibrium [2, 3]. In 2011, Wei proposed a chaotic oscillator without an equilibrium point [4]. Also, in 2012, Wang and Chen presented a novel chaotic oscillator with one stable equilibrium [5]. These works have shown that a flow can have chaotic dynamics with any equilibria or without it [6, 7]. Many studies have discussed chaotic oscillators with lines of equilibria [8, 9]. Lyapunov exponent is a valuable measure in the study of chaos, and its calculation has been a hot topic [10].

Many research studies have been focused on proposing chaotic flows with various features [11–13]. Multiscroll

dynamics were discussed in [14]. Hyperchaotic oscillators are attractive because of their complex dynamics [15]. The hyperchaotic dynamics are efficient in secure communications so that it is not possible to retrieve hidden messages [16]. These oscillators also have two positive LEs and high sensitivity to initial values [17]. In [18], a hyperchaotic oscillator with no equilibria was studied. Oscillators with self-excited and hidden attractors were discussed in [19, 20]. In [21], hidden dynamics in a piecewise linear oscillator were studied. Synchronization and control of chaotic flows have attracted much attention [22]. Multistability is a significant feature of dynamical systems [23]. The final circumstance of a multistable oscillator is determined by initial conditions in a constant set of parameters [24]. In case of undesirable multistability, the final state can be controlled by selecting the proper parameters to transform to monostability [25]. The multistability of a piecewise linear oscillator with various types of attractors was investigated in [26]. A

multistable chaotic oscillator with different dynamics was proposed in [27]. In [28], a megastable system with a particular term was studied. A megastable system and its dynamics were discussed in [29]. The application of chaotic dynamics in encryption [30], secure communication [31], and robotics [32] has been a hot topic.

Chaotic dynamics can be classified as dissipative or conservative ones. In the dissipative dynamics, the phase space volume approaches zero when time goes to infinity; however, in conservative dynamics, volume is constant by changing time [33]. Conservative oscillators can conserve energy and display chaos without damping (although energy is not conserved in real mechanics) [33]. Studying conservative chaotic oscillators has been a hot topic [34]. Conservative dynamics of a chaotic oscillator based on Sprott A were discussed in [35, 36]. In [37], various groups of conservative oscillators were studied. The conservative flows were categorized into four groups based on their dissipation [37].

Here, a novel conservative oscillator with a line of equilibria is presented. The oscillator is a simple one with five terms. The oscillator is symmetric, which shows two symmetric coexisting dynamics. From the mathematical and computational point of view, there has been a noticeable interest in chaotic systems with special features [1–3]. The proposed chaotic system has some important features:

(a) It is conservative, and 3D conservative chaotic systems are rare [4–6]

(b) It has a line of equilibria, and 3D chaotic systems with a line of equilibria are rare [7–9]

(c) It is multistable, making the system more interesting in some applications [10]

The proposed system has all the features above, and we are aware of no other system with those properties combined. As far as we know, there is only one 4D conservative chaotic system with a line of equilibria in [11]. Therefore, the system itself is interesting and deserves attention. In Section 2, the oscillator is proposed, and its chaotic sea is discussed. Also, the symmetry of the oscillator and its line of equilibria are studied. In Section 3, various dynamics of the oscillator are discussed. The Poincare section, bifurcation diagram, Lyapunov exponents (LEs), and initial conditions are studied. In Section 4, the results are concluded.

2. The Conservative Oscillator

Here, a conservative oscillator is proposed as

$$
\begin{aligned}
\dot{x} &= y, \\
\dot{y} &= -ax + yz, \\
\dot{z} &= x^2 - by^2.
\end{aligned}
\tag{1}
$$

The system is a three-dimensional quadratic oscillator containing five terms; thus, it can be considered a simple chaotic oscillator. The oscillator shows a conservative chaotic dynamic in $a = 1, b = 0.68$, and $(x_0, y_0, z_0) = (-0.57, -0.99, -0.71)$. The time series and state space of the chaotic sea are plotted in

Figure 1. The LEs of the oscillator in the mentioned parameters are calculated with a run time of 120000. The LEs are obtained as $(0.0055, 0, -0.0055)$; therefore, the Kaplan–Yorke dimension (D_{KY}) is 3. The chaotic dynamic is conservative since D_{KY} is 3 and the sum of LEs is zero. As a result, the oscillator has no dissipation; i.e., energy is conserved when time goes to infinity.

Considering the equations of the oscillator, the system has symmetry by changing (x, y, z) to $(-x, -y, z)$. The two coexisting conservative dynamics are plotted in Figure 2 with two initial conditions $(-0.57, -0.99, -0.71)$ and $(0.57, 0.99, -0.71)$. The ranges of the two chaotic seas show that the two chaotic seas are entangled with each other. In other words, the variable intervals of the two multistable chaotic dynamics are approximately the same.

Calculating the equilibria of the oscillator reveals that it has a line of equilibria at $x = 0, y = 0$. To analyze the equilibria's stability, the Jacobian matrix and eigenvalues of the oscillator are calculated as equations (2)–(4) by considering parameters $a = 1$ and $b = 0.68$:

$$
J = \begin{bmatrix} 0 & 1 & 0 \\ -1 & z & y \\ 2x & -1.36y & 0 \end{bmatrix},
\tag{2}
$$

$$
|\lambda I - J| = \begin{vmatrix} \lambda & -1 & 0 \\ 1 & \lambda - z & 0 \\ 0 & 0 & \lambda \end{vmatrix} = 0,
\tag{3}
$$

$$
\lambda(\lambda^2 - z\lambda + 1) = 0.
\tag{4}
$$

Eigenvalues are obtained as $\lambda_1 = 0$ and $\lambda_{2,3} = z \pm \sqrt{z^2 - 4}/2$. So, the stability of equilibrium points is dependent on their location of z. The real and imaginary parts of eigenvalues by changing z are shown in Figure 3. In positive z, the real parts of λ_2 and λ_3 are positive. So the equilibrium points with positive z are unstable. In negative z, there is not any positive eigenvalue. However, the type of equilibria cannot be determined in that interval using the eigenvalues. Numerical analysis shows that the equilibrium points are stable in negative z. The imaginary part of the eigenvalues reveals that the equilibria are spirals in the interval $z \in [-2, 2]$.

3. Dynamical Behavior

Various methods can be used to show a three-dimensional chaotic flow in two dimensions. One of the useful methods is the Poincare section [33]. The Poincare section of the oscillator with $a = 1, b = 0.68$, and $(x_0, y_0, z_0) = (-0.57 - 0.99 - 0.71)$ by selecting a section $= \{(x, y) \in R^2 | z = 0\}$ is presented in Figure 4. The values of the Poincare section are the values of trajectories crossing the plane $z = 0$. The symmetry of the oscillator's dynamics can be seen in this figure.

Bifurcation diagram is one important method to investigate various dynamics of chaotic oscillators. The bifurcation diagram of the oscillator by varying parameter a in the interval $[1, 1.28]$ is plotted in Figure 5(a). The bifurcation values are obtained using the maximum value of the x
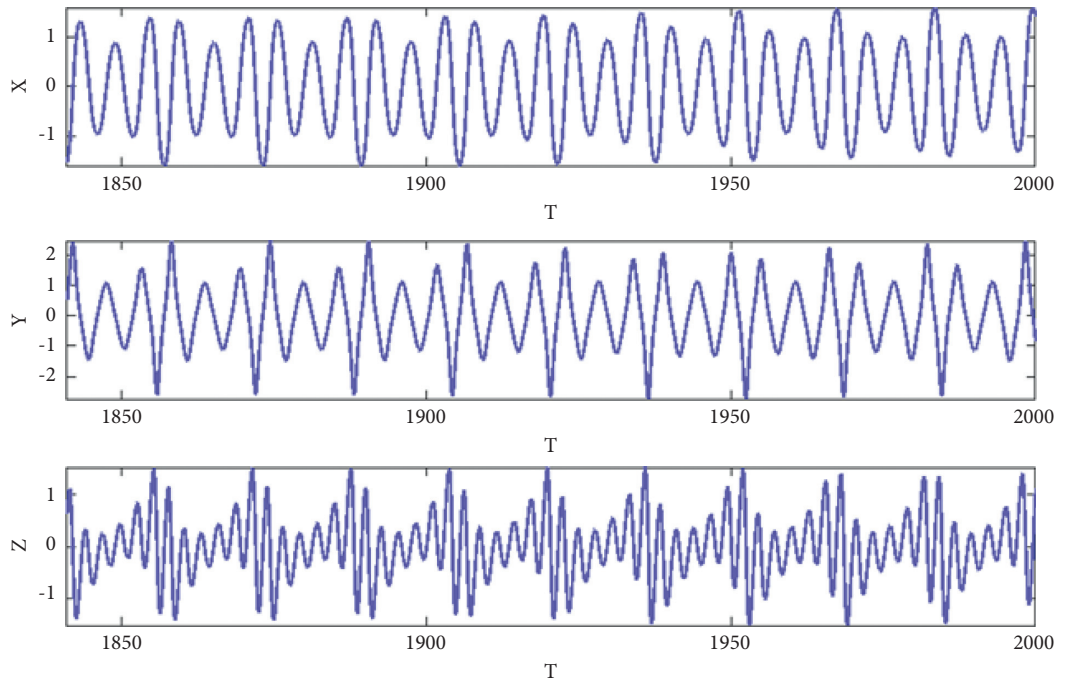
(a)
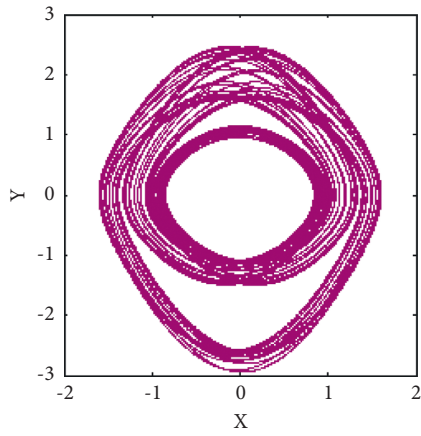
(b)
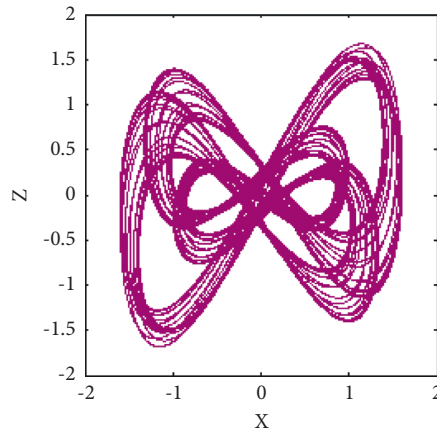
(c)
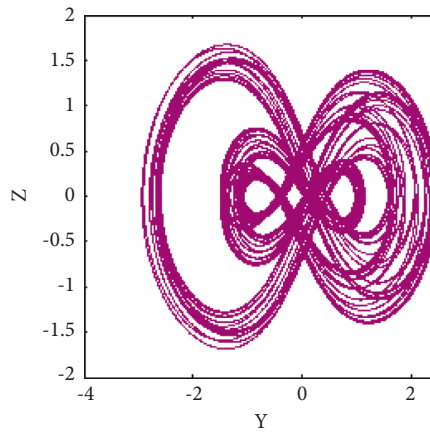
(d)
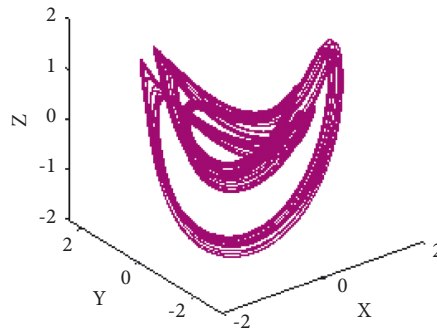
(e)

Figure 1: Time series (a) and chaotic sea with initial condition $(x0, y0, z0) = (-0.57 - 0.99 - 0.71)$ and parameters $(a, b) = (1, 0.68)$ in (b)X_Y, (c)$X - Z$, (d)$Y - Z$, and (e)X_Y_Z.
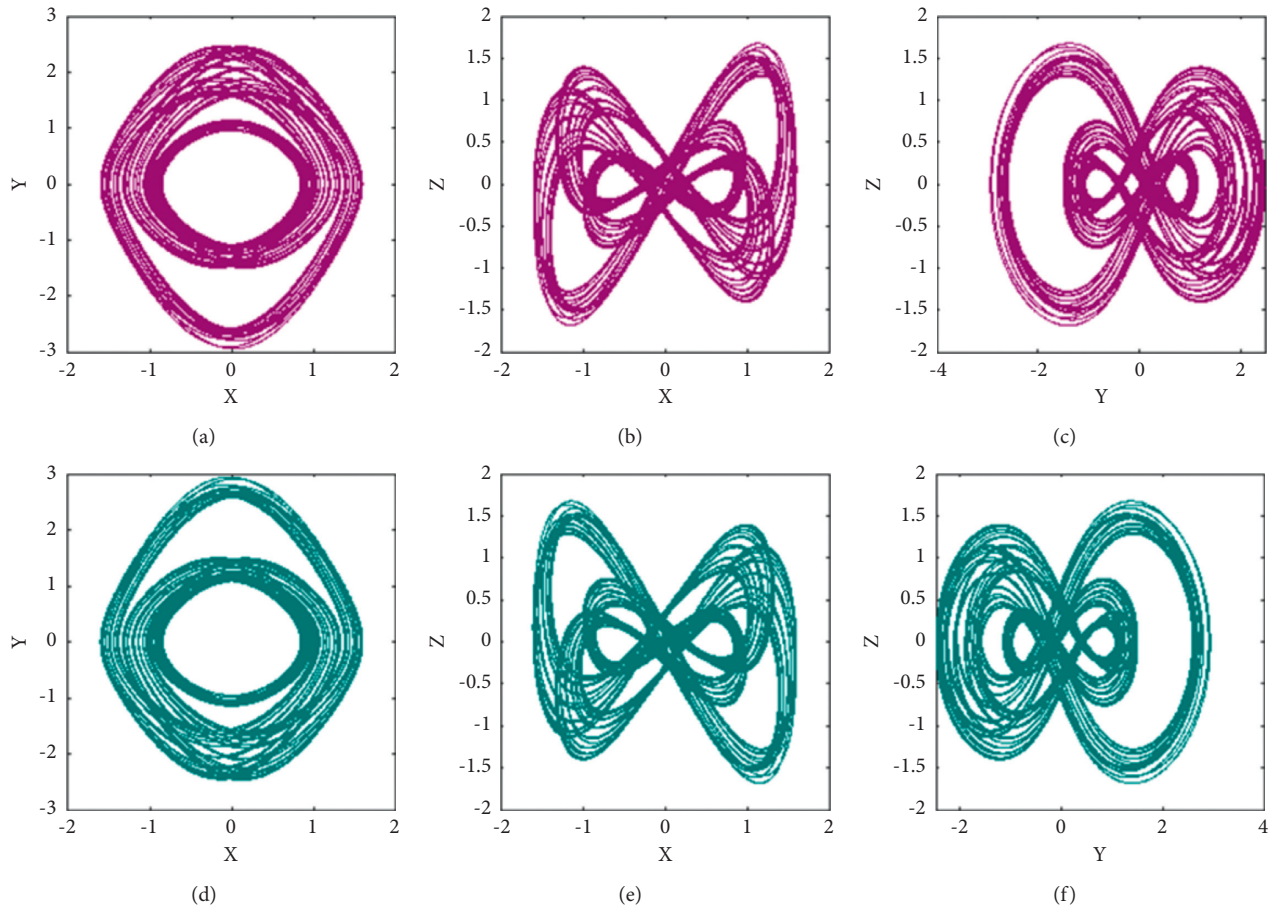
FIGURE 2: Chaotic sea of the oscillator with initial conditions $(-0.57, -0.99, -0.71)$, (a) in $X - Y$, (b) in $X - Z$, and (c) in $Y - Z$, and with initial conditions $(0.57, 0.99, -0.71)$, (d) in $X - Y$, (e) in $X - Z$, and (f) in $Y - Z$. The two dynamics are symmetric.
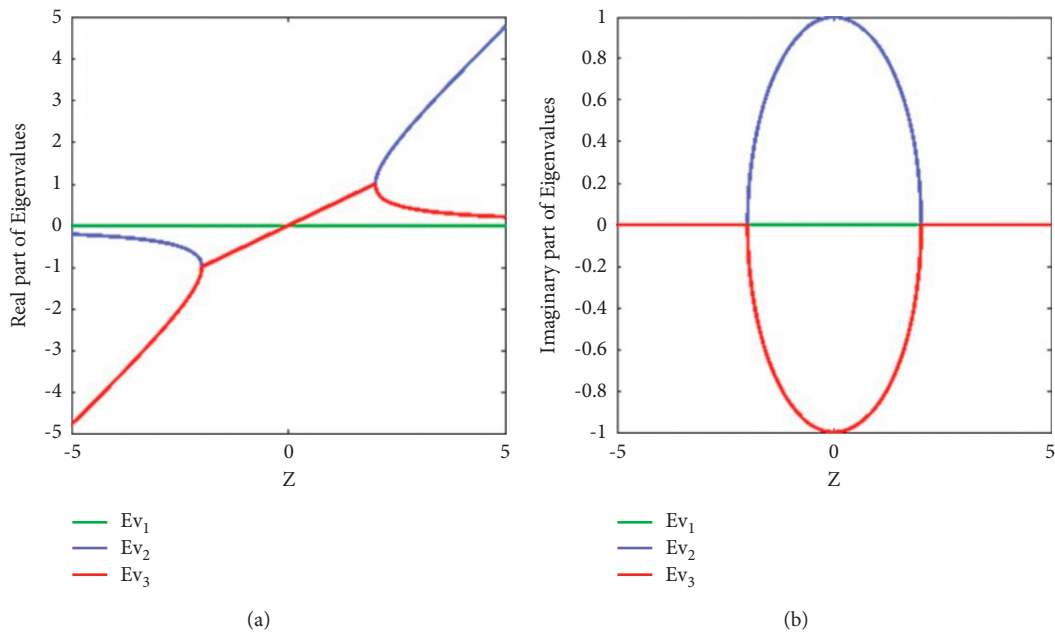
FIGURE 3: (a) Real and (b) imaginary part of eigenvalues for oscillator (1) with parameters $(a, b) = (1, 0.68)$.
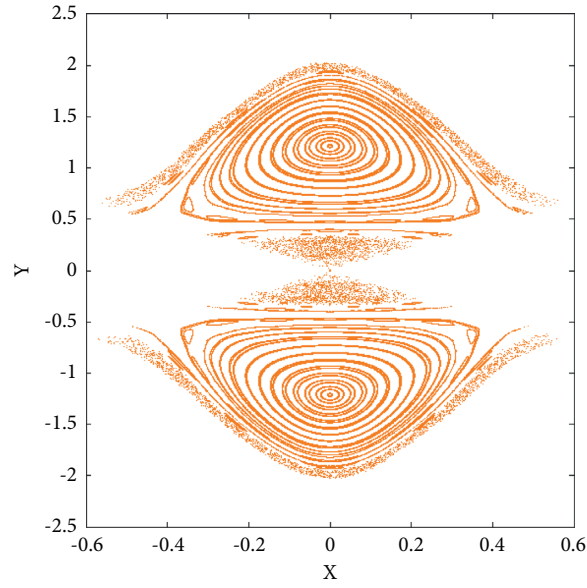
FIGURE 4: The Poincare section with crossing section.

(a)

(b)
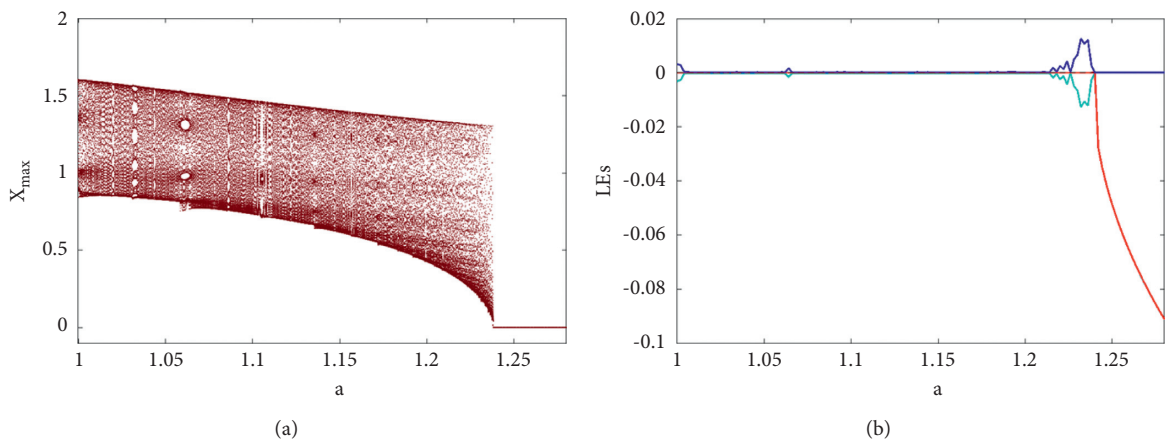
FIGURE 5: (a) Bifurcation diagram and (b) LEs of oscillator (1) by changing parameter a, with constant initial conditions $(x_0, y_0, z_0) = (-0.57, -0.99, -0.71)$.

(a)

(b)
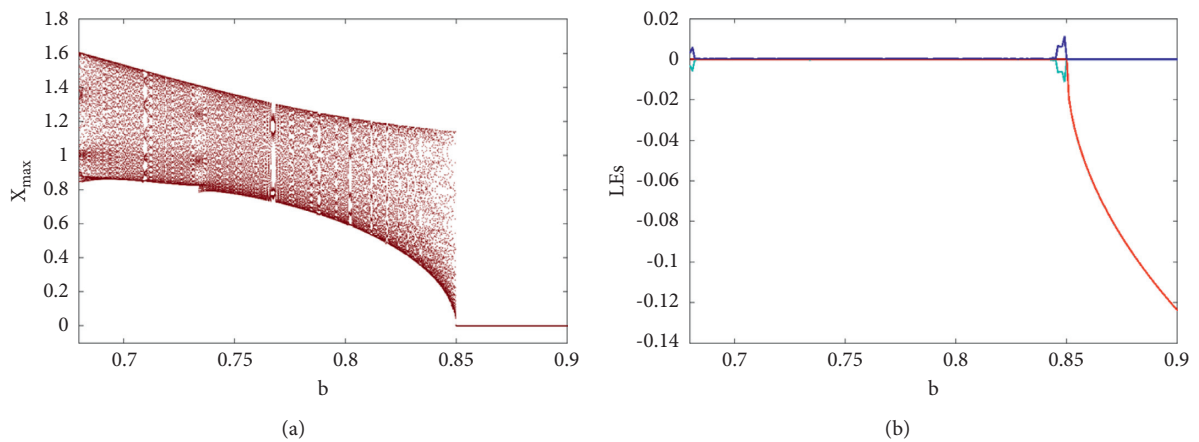
FIGURE 6: (a) Bifurcation diagram and (b) LEs of oscillator (1) by changing parameter b with constant initial conditions $(x_0, y_0, z_0) = (-0.57, -0.99, -0.71)$.

(a)

(b)

(c)
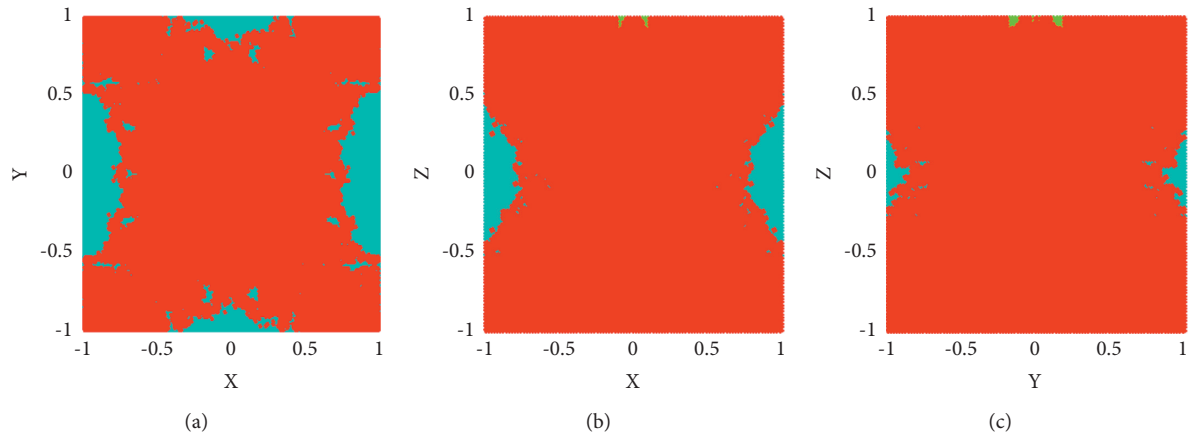
FIGURE 7: Initial values for various dynamics of the proposed oscillator in (a) *X-Y* plane, (b) *X-Z* plane, and (c) *Y-Z* plane. The oscillatory region is cyan, the equilibrium points are red, and the unbounded points are green.

variable in (1) with $b = 0.68$. The other variables show the same dynamics, so only x_{max} is presented. To analyze another parameter, x_{max} is plotted by changing b in the interval $[0.68, 0.9]$ with parameter $a = 1$ in Figure 6(a). The initial conditions for both diagrams are considered constant values as $(x_0, y_0, z_0) = (-0.57, -0.99, -0.71)$. The corresponding LEs by changing the parameters a and b are shown in Figures 5(b) and 6(b), respectively. The LEs are calculated with run time 50000 using the wolf method [10]. According to the bifurcation diagram and LEs, various dynamics can be seen by changing parameters. In $a = 1.239$ and $b = 0.85$, there is a sudden change in the dynamics of the oscillator in which the chaotic dynamics collapse.

Basin of attraction reveals the initial conditions that are attracted to various attractors of an oscillator. Figure 7 shows the initial values in the region of different dynamics. In Figure 7(a), the initial values of x and y variables are changing in the interval $x \in [-1, 1]$, $y \in [-1, 1]$. The initial value of the variable z is constant and is equal to zero. In addition, initial values in *X-Z* and *Y-Z* planes are investigated where y_0 and x_0 are equal to zero, respectively. Cyan color demonstrates the oscillatory region while red color shows equilibrium points. Moreover, there are unbounded points that are shown with green color. The system has symmetry by changing (x, y, z) to $(-x, -y, z)$. The symmetric regions are consistent with the oscillator's symmetry, which was also seen in the Poincare section.

4. Conclusion

Here, an oscillator with conservative chaotic dynamics was proposed. By calculating LEs and D_{KY}, the dissipation of the oscillator was investigated. The summation of LEs was equal to zero, and D_{KY} was 3, which presented the conservative dynamics of the oscillator. The oscillator had a line of equilibria. Half of the line was unstable, while the other half was stable. The oscillator was symmetric. This symmetry reveals that the oscillator had a pair of the conservative chaotic sea. The symmetry of the oscillator's dynamics also was seen in the Poincare section. The bifurcation diagram of

the oscillator was studied by changing parameters. The diagrams have shown the collapse of the chaotic dynamics by changing the bifurcation parameter. The dynamics of the bifurcation diagram were proved by LEs. The initial conditions that have resulted in various dynamics of the oscillator were also discussed. This study has revealed the uniqueness of the proposed conservative oscillator.

Data Availability

All the data used for the numerical analysis are mentioned within the article.

Conflicts of Interest

The authors declare that there are no conflicts of interest.

Acknowledgments

References

[1] E. N. Lorenz, "Deterministic nonperiodic flow," *Journal of the Atmospheric Sciences*, vol. 20, no. 2, pp. 130–141, 1963.

[2] O. E. Rössler, "An equation for continuous chaos," *Physics Letters A*, vol. 57, pp. 397-398, 1976.

[3] G. Chen and T. Ueta, "Yet another chaotic attractor," *International Journal of Bifurcation and Chaos*, vol. 09, no. 7, pp. 1465-1466, 1999.

[4] Z. Wei, "Dynamical behaviors of a chaotic system with no equilibria," *Physics Letters A*, vol. 376, no. 2, pp. 102–108, 2011.

[5] X. Wang and G. Chen, "A chaotic system with only one stable equilibrium," *Communications in Nonlinear Science and Numerical Simulation*, vol. 17, no. 3, pp. 1264–1272, 2012.

[6] K. Rajagopal, A. Karthikeyan, and A. K. Srinivasan, "FPGA implementation of novel fractional-order chaotic systems with two equilibriums and no equilibrium and its adaptive

sliding mode synchronization," *Nonlinear Dynamics*, vol. 87, no. 4, pp. 2281–2304, 2017.

[7] F. Nazarimehr, K. Rajagopal, J. Kengne, S. Jafari, and V.-T. Pham, "A new four-dimensional system containing chaotic or hyper-chaotic attractors with no equilibrium, a line of equilibria and unstable equilibria," *Chaos, Solitons & Fractals*, vol. 111, pp. 108–118, 2018.

[8] F. Nazarimehr and J. C. Sprott, "Investigating chaotic attractor of the simplest chaotic system with a line of equilibria," *The European Physical Journal - Special Topics*, vol. 229, no. 6-7, pp. 1289–1297, 2020.

[9] J. P. Singh and B. K. Roy, "The simplest 4-D chaotic system with line of equilibria, chaotic 2-torus and 3-torus behaviour," *Nonlinear Dynamics*, vol. 89, no. 3, pp. 1845–1862, 2017.

[10] A. Wolf, J. B. Swift, H. L. Swinney, and J. A. Vastano, "Determining Lyapunov exponents from a time series," *Physica D: Nonlinear Phenomena*, vol. 16, no. 3, pp. 285–317, 1985.

[11] X. Zhang, C. Li, F. Min, H. H. Iu, and H. Gao, "Broken Symmetry in a Memristive Chaotic Oscillator," *IEEE Access*, vol. 8, 2020.

[12] S. He, S. Banerjee, and K. Sun, "Complex dynamics and multiple coexisting attractors in a fractional-order microscopic chemical system," *The European Physical Journal - Special Topics*, vol. 228, no. 1, pp. 195–207, 2019.

[13] S. He and S. Banerjee, "Epidemic outbreaks and its control using a fractional order model with seasonality and stochastic infection," *Physica A: Statistical Mechanics and Its Applications*, vol. 501, pp. 408–417, 2018.

[14] E. Campos-Cantón, J. G. Barajas-Ramirez, G. Solis-Perales, and R. Femat, "Multiscroll attractors by switching systems," *Chaos: An Interdisciplinary Journal of Nonlinear Science*, vol. 20, Article ID 013116, 2010.

[15] A. Karthikeyan, S. Çiçek, K. Rajagopal, P. Duraisamy, and A. Srinivasan, "New hyperchaotic system with single nonlinearity, its electronic circuit andencryption design based on current conveyor," *Turkish Journal of Electrical Engineering and Computer Sciences*, vol. 29, pp. 1692–1705, 2021.

[16] T. Banerjee, D. Biswas, and B. Sarkar, "Design of chaotic and hyperchaotic time-delayed electronic circuit," *Bonfring International Journal of Power Systems and Integrated Circuits*, vol. 2, no. 4, pp. 13–17, 2012.

[17] R. Tchitnga, B. A. Mezatio, T. F. Fozin, R. Kengne, P. H. Louodop Fotso, and A. Fomethe, "A novel hyperchaotic three-component oscillator operating at high frequency," *Chaos, Solitons & Fractals*, vol. 118, pp. 166–180, 2019.

[18] Z. Wang, S. Cang, E. O. Ochola, and Y. Sun, "A hyperchaotic system without equilibrium," *Nonlinear Dynamics*, vol. 69, no. 1-2, pp. 531–537, 2012.

[19] C. K. Volos, S. Jafari, J. M. Munoz-Pacheco, J. Kengne, and K. Rajagopal, "Nonlinear dynamics and entropy of complex systems with hidden and self-excited attractors II," *Entropy*, vol. 22, no. 12, p. 1428, 2020.

[20] R. Escalante-González and E. Campos, "Generation of self-excited and hidden multiscroll attractors in multistable systems," in *Recent Trends in Chaotic, Nonlinear and Complex Dynamics*, pp. 40–78, World Scientific, Singapore, 2021.

[21] J. R. Pulido-Luna, J. A. López-Rentería, N. R. Cazarez-Castro, and E. Campos, "A two-directional grid multiscroll hidden attractor based on piecewise linear system and its application in pseudo-random bit generator," *Integration*, vol. 81, 2021.

[22] I. Koyuncu, K. Rajagopal, M. Alcin, A. Karthikeyan, M. Tuna, and M. Varan, "Control, synchronization with linear quadratic regulator method and FFANN-based PRNG application on FPGA of a novel chaotic system," *The European Physical Journal - Special Topics*, vol. 230, pp. 1–17, 2021.

[23] A. Karthikeyan, M. E. Cimen, A. Akgul, A. F. Boz, and K. Rajagopal, "Persistence and coexistence of infinite attractors in a fractal Josephson junction resonator with unharmonic current phase relation considering feedback flux effect," *Nonlinear Dynamics*, vol. 103, no. 2, pp. 1979–1998, 2021.

[24] A. N. Pisarchik and U. Feudel, "Control of multistability," *Physics Reports*, vol. 540, no. 4, pp. 167–218, 2014.

[25] P. R. Sharma, M. D. Shrimali, A. Prasad, N. V. Kuznetsov, and G. A. Leonov, "Control of multistability in hidden attractors," *The European Physical Journal - Special Topics*, vol. 224, no. 8, pp. 1485–1491, 2015.

[26] R. d. J. Escalante-González and E. Campos, "Multistable systems with hidden and self-excited scroll attractors generated via piecewise linear systems," *Complexity*, vol. 2020, Article ID 7832489, 12 pages, 2020.

[27] K. Rajagopal, Y. Shekofteh, F. Nazarimehr, C. Li, and S. Jafari, "A new chaotic multi-stable hyperjerk system with various types of attractors," *Indian Journal of Physics*, pp. 1–7, 2021.

[28] D. Veeman, H. Natiq, N. M. Al-Saidi, K. Rajagopal, S. Jafari, and I. Hussain, "A new megastable chaotic oscillator with blinking oscillation terms," *Complexity*, vol. 2021, Article ID 5518633, 12 pages, 2021.

[29] H. Lu, K. Rajagopal, F. Nazarimehr, and S. Jafari, "A new multi-scroll megastable oscillator based on the sign function," *International Journal of Bifurcation and Chaos*, vol. 31, no. 8, Article ID 2150140, 2021.

[30] B. B. Cassal-Quiroga and E. Campos-Cantón, "Generation of dynamical S-boxes for block ciphers via extended logistic map," *Mathematical Problems in Engineering*, vol. 2020, Article ID 2702653, 12 pages, 2020.

[31] J. Sun, Y. Shen, Q. Yin, and C. Xu, "Compound synchronization of four memristor chaotic oscillator systems and secure communication," *Chaos: An Interdisciplinary Journal of Nonlinear Science*, vol. 23, no. 1, Article ID 013140, 2013.

[32] X. Zang, S. Iqbal, Y. Zhu, X. Liu, and J. Zhao, "Applications of chaotic dynamics in robotics," *International Journal of Advanced Robotic Systems*, vol. 13, no. 2, p. 60, 2016.

[33] J. C. Sprott, *Elegant Chaos: Algebraically Simple Chaotic Flows*, World Scientific, Singapore, 2010.

[34] Y. Li, Z. Chen, Z. Wang, and S. Cang, "Nonlinear dynamics analysis of cluster-shaped conservative flows generated from a generalized thermostatted system," *Chinese Physics B*, vol. 31, Article ID 010501, 2021.

[35] S. Cang, Y. Li, W. Xue, Z. Wang, and Z. Chen, "Conservative chaos and invariant tori in the modified Sprott A system," *Nonlinear Dynamics*, vol. 99, no. 2, pp. 1699–1708, 2020.

[36] S. Cang, Y. Li, Z. Kang, and Z. Wang, "Generating multi-cluster conservative chaotic flows from a generalized Sprott-A system," *Chaos, Solitons & Fractals*, vol. 133, Article ID 109651, 2020.

[37] S. Jafari, J. C. Sprott, and S. Dehghan, "Categories of conservative flows," *International Journal of Bifurcation and Chaos*, vol. 29, no. 2, Article ID 1950021, 2019.

WILEY | Hindawi

Research Article

Spiral Motion Enhanced Elite Whale Optimizer for Global Tasks

GuoChun Wang,[1] Wenyong Gui,[2] Guoxi Liang [ID],[3] Xuehua Zhao,[4] Mingjing Wang [ID],[5] Majdi Mafarja,[6] Hamza Turabieh,[7] Junyi Xin [ID],[8] Huiling Chen [ID],[2] and Xinsheng Ma [ID][9]

[1]College of Applied Technology, Changchun University of Technology, Changchun, Jilin 130012, China
[2]College of Computer Science and Artificial Intelligence, Wenzhou University, Wenzhou, Zhejiang 325035, China
[3]Department of Information Technology, Wenzhou Polytechnic, Wenzhou 325035, China
[4]School of Digital Media, Shenzhen Institute of Information Technology, Shenzhen 518172, China
[5]Institute of Research and Development, Duy Tan University, Da Nang 550000, Vietnam
[6]Department of Computer Science, Birzeit University, Birzeit, State of Palestine
[7]Department of Information Technology, College of Computers and Information Technology, P.O. Box 11099, Taif University, Taif 21944, Saudi Arabia
[8]School of Information Engineering, Hangzhou Medical College, Hangzhou 311300, Zhejiang, China
[9]Department of Mathematics, Zhejiang International Studies University, Hangzhou 310023, China

Correspondence should be addressed to Junyi Xin; xinjunyi@hmc.edu.cn, Huiling Chen; chenhuiling.jlu@gmail.com, and Xinsheng Ma; xsma@zisu.edu.cn

The whale optimization algorithm (WOA) is a high-performance metaheuristic algorithm that can effectively solve many practical problems and broad application prospects. However, the original algorithm has a significant improvement in space in solving speed and precision. It is easy to fall into local optimization when facing complex or high-dimensional problems. To solve these shortcomings, an elite strategy and spiral motion from moth flame optimization are utilized to enhance the original algorithm's efficiency, called MEWOA. Using these two methods to build a more superior population, MEWOA further balances the exploration and exploitation phases and makes it easier for the algorithm to get rid of the local optimum. To show the proposed method's performance, MEWOA is contrasted to other superior algorithms on a series of comprehensive benchmark functions and applied to practical engineering problems. The experimental data reveal that the MEWOA is better than the contrast algorithms in convergence speed and solution quality. Hence, it can be concluded that MEWOA has great potential in global optimization.

1. Introduction

Optimization tasks can be classified into many forms according to the relation and number of objectives or hybrid methods, such as robust optimization [1], large scale optimization [2, 3], multiobjective [4], fuzzy optimization [5], and many objectives [6, 7]. One of the classes of the optimizers is based on an iteration-based evolution of the swarm. At present, metaheuristic methods have attracted more and more attention from the public [8–22]. Because optimization problems appear in many fields of science, and

they can be a solution to many fields like support vector machines [20, 23], feature selection [17, 24–28], extreme learning machine (ELM) [29–34], bankruptcy prediction [19, 35–38], engineering design [16, 18, 39–43], optimal resource allocation [44], monitoring [45–48], parameters optimization [49], temperature optimization [50], intelligent damage detection [51, 52], smart grid [53], image enhancement optimization [54], image and video handling [55–60], medical image recognition [61], and image segmentation [62, 63], its randomness, diversification, and strengthening ability can effectively solve high nonlinearity

and multilocal optimization problems. It can maximize the relationship between resources and interests and create maximum benefits under the condition of limited resources.

Swarm methods have emerged in many fields as they can deal with a wide variety of problems in a flexible way. Some well-distributed techniques are slime mould algorithm [64], Harris hawks optimization (HHO) [65], naked mole-rat algorithm (NMR) [66], hunger games search (HGS) [67], moth search algorithm (MSA) [68], monarch butterfly optimization (MBO) [69], krill herd algorithm (KH) [70], teaching-learning-based optimizer (TLBO) [71], differential evolution (DE) [72], and differential search (DS) [73]. The exploratory and exploitative abilities of the swarm-based method can be a good evolutionary basis to be applied to areas such as computer vision [74], deployment optimization [75], enhancement of the transportation networks [76], optimization of the tasks of deep learning [77–79], improvement of the prediction methods [80, 81], and decision-making technique [82–84]. One of the possible methods is the whale optimization algorithm (WOA), which is an intelligent optimization algorithm presented by Mirjalili and Lewis [85] in 2016. The algorithm mainly focuses on the whale's hunting behavior and the prey's predatory behavior to seek the optimal solution to the problem. Although WOA has the advantages of fewer parameters and strong global convergence, the standard WOA still possesses the problems of slow convergence speed and low convergence accuracy. Thus, many improved versions can be found in the literature. Wang et al. [86] devised the MOWOA, an opposition-based multiobjective WOA using global grid ranking, using multiple parts to improve optimization performance. In order to solve the problems of poor exploration and local optimal stagnation of WOA, Salgotra et al. [87] proposed an improved WOA based on mechanisms such as opposition-based learning, exponentially decreasing parameters, and elimination or reinitialization of the worst particles. The improved algorithm has been experimentally demonstrated to have a large improvement in performance. Sun et al. [88] enhanced the WOA with the strategy of quadratic interpolation (QIWOA). The algorithm introduced new parameters to effectively search for solution spaced and handled premature convergence and adopted the quadratic interpolation around the best individual to enhance its exploitation capability and solution precision. Agrawal et al. [89] combined quantum concepts with the WOA, adopting the quantum bit representation of population agents and the quantum rotation gate operator as mutation operators to improve the exploration and exploitation ability of classical WOA. Hussein et al. [90] handled binary optimization problems by using the basic version of WOA and devising two transfer functions (S-shaped and V-shaped) to map the continuous search space into binary ones. Luo et al. [91] integrated three strategies with the original approach to obtain a better balance between exploration and exploitation trends. Firstly, the chaos initialization phase is utilized to start a group of chaos-triggered whales at the initial phase. Then, the diversity level of the evolutionary population is enhanced by the Gaussian mutation. Finally, the chaotic local search, combined with the "narrowing" strategy, is utilized to raise the original optimizer's utilization tendency. The effect of the signal is due to the base concepts in chaos theory [59, 92–94]. Sun et al. [95] proposed a nonlinear dynamic control parameter updating strategy based on cosine function and integrated this strategy and Lévy flight strategy into WOA (MWOA). Hemasian-Etefagh and Safi-Esfahani et al. [96] introduced a new idea (called GWOA) in whale grouping to overcome the early convergence problem. Elaziz and Mirjalili [97] integrated chaotic mapping and opposition-based learning into the algorithm and used the differential evolution (DE) algorithm to automatically select the chaotic graph and part of the population to alleviate the defects (DEWCO). Guo [98] devised an enhanced WOA by using the strategy of social learning and wavelet mutation. A new linear incremental probability is designed to increase the capability of global search. According to the principle of social learning, an individual's social network is constructed by using social hierarchy and social influence. So as to learn the exchange and sharing of information among groups, they established an adaptive neighborhood learning strategy on the basis of the network relationship. The Morlet wavelet mutation mechanism is adopted to learn the dynamic adjustment of mutation space, thus enhancing the capability of the algorithm to get rid of the local optimum.

WOA and its improved versions are often used to solve some practical application problems. Revathi et al. [99] devised an optimization scheme with the brainstorm WOA (BS-WOA) to identify the key used to improve the data structure's privacy and practicability by amending the database. Gong et al. [100] used an improved edition of the WOA to determine the optimal features and amend the classification's artificial neural network weights. The model is simulated on FLAIR, T1, and T2 data sets, showing that the presented model has a robust diagnostic capability. The model was then used to diagnose common diseases such as breast cancer, diabetes, and erythema squamous epithelium. Zhang et al. [101] utilized the best convolutional neural network (CNN) to process the skin disease image and adopted the improved WOA to optimize the CNN. Xiong et al. [102] devised an enhanced WOA, called IWOA, to accurately optimize different PV models' parameters, a typical complex nonlinear multivariable strong coupling optimization problem. Petrović et al. [103] analyzed the scheduling problem of a single mobile robot, and the best transportation method of raw materials, goods, and parts in an intelligent manufacturing system was found through WOA. Li et al. [104] used WOA to modify the input weight and hidden layer bias of extreme learning machine (ELM) and used this model to assess the aging of insulated gate bipolar transistor module. Akyol and Alatas [105] adopted WOA for emotional analysis, which is a multiobjective problem. Qiao [106] introduced adaptive search and encircling mechanism, spiral position, and jump behavior to enhance the efficiency of WOA and used the improved algorithm to predict short-term gas consumption. Lévy flight and pattern search were embedded into WOA for parameter estimation of solar cell and photovoltaic system [107].

Although WOA has significantly improved its performance and robustness compared with other metaheuristics algorithms, it is still not free from the dilemma of easily falling into local optimal solutions and other problems, and the same phenomenon of low solution accuracy and slow convergence exists when solving function problems. So, this paper proposes an improved variant of WOA, which is named MEWOA. We introduce two strategies: elite strategy and spiral motion from moth flame optimization (MFO) [12, 108, 109], which significantly strengthens the convergence accuracy and speed of the basic WOA easier to jump out of local optimum. To further verify the performance of MEWOA, the algorithm is also utilized to solve practical engineering problems. The results reveal that MEWOA is superior to the other algorithms with high solution quality and convergence speed.

The main contributions of this study can be summarized as follows:

(i) Aiming at overcoming the problems of WOA, we introduce elite strategies as well as spiral motion into WOA to improve the diversity of populations while enhancing optimal solution selection and finally propose an improved WOA (MEWOA)

(ii) The MEWOA is compared with some with metaheuristic algorithms and advanced algorithms on function test sets such as CEC2017 and CEC2014, respectively, and satisfactory results are obtained

(iv) The proposed MEWOA has achieved excellent results in three typical engineering problems

This paper is structured as follows. Section 2 briefly introduces WOA, elite strategy, and MFO. Section 3 describes MEWOA. In Section 4, a range of experiments is conducted based on MEWOA to demonstrate the proposed algorithm's performance. In Section 5, the full content is summarized, and the future research direction is pointed out.

2. Background Knowledge

2.1. Whale Optimization Algorithm (WOA). WOA is a new metaheuristic algorithm devised by Mirjalili and Lewis [85] based on the Bubble-net behavior of humpback whales during hunting. In this algorithm, each humpback's position represents a feasible solution. Humpback whales hunt by producing unique bubbles along with a circular or "9" shaped path. According to such a phenomenon, the authors' mathematical models include the following three steps: random search, encircling prey, and attacking prey.

2.1.1. Random Search. Each agent's position is randomly generated to find prey. Moreover, the specific process is as follows:

$$\vec{D} = \left| \vec{C} \, \vec{X}_{\text{rand}}^{d} - \vec{X}^{d}(t) \right|, \tag{1}$$

$$\vec{X}^{d}(t+1) = \vec{X}_{\text{rand}}^{d} - \vec{A} \cdot \vec{D}, \tag{2}$$

where $\vec{X}_{\text{rand}}^{d}$ is the position of the d-th dimension in the randomly selected whale, $\vec{X}^{d}$ denotes the position of the current individual in d-th dimension, t means the current number of iterations, the calculation result of $\vec{D}$ denotes the distance between the random individual and the current individual, and $\vec{A}$ and $\vec{C}$ are the coefficients as shown in the following formulas.

$$\begin{aligned} \vec{A} &= 2\vec{a} \cdot \vec{r}_{1} - \vec{a}, \\ \vec{C} &= 2 \cdot \vec{r}_{2}, \end{aligned} \tag{3}$$

where $\vec{a}$ is a constant that will linearly lessen from 2 to 0, and $\vec{r}_{1}$ and $\vec{r}_{2}$ are random numbers in $[0, 1]$.

2.1.2. Encircling Prey. When searching for the prey, the mathematical model is as follows:

$$\vec{D} = \left| \vec{C} \, \vec{X}_{\text{best}}^{d}(t) - \vec{X}^{d}(t) \right|, \tag{4}$$

$$\vec{X}^{d}(t+1) = \vec{X}_{\text{best}}^{d}(t) - \vec{A} \cdot \vec{D}, \tag{5}$$

where $\vec{X}_{\text{best}}^{d}(t)$ reveals the position of the d-th dimension in the best individual so far, $\vec{X}^{d}$ denotes the position of the current individual in d-th dimension, and the calculation result of D denotes the distance between the best individual and the current individual.

2.1.3. Attacking Prey. On the basis of the hunting behavior of humpback whale, it swims in a spiral motion, so the mathematical model of hunting behavior is devised as follows:

$$\vec{X}^{d}(t+1) = \vec{X}_{\text{best}}^{d}(t) + \vec{D}_{p} \cdot e^{bl} \cdot \cos(2\pi l), \tag{6}$$

where $\vec{D}_{p} = |\vec{X}_{\text{best}}^{d}(t) - \vec{X}^{d}(t)|$ denotes the distance between the whale and its prey, b is a constant utilized to define the shape of the spiral, and l is a random number in $[-1, 1]$.

As the whale approaches its food in a spiral shape, it also shrinks its encircling circle. Therefore, P_{i} is adopted to realize this synchronous behavior model, and Mirjalili sets P_{i} as 0.5 to change the position of the whale between the constricted encircling mechanism or the spiral model. The concrete model is shown as follows:

$$\vec{X}^{d}(t+1) = \begin{cases} \vec{X}_{*}^{d}(t) - \vec{A} \cdot \vec{D}, & p < P_{i}, \\ \vec{X}_{\text{best}}^{d}(t) + \vec{D}_{p} \cdot e^{bl} \cdot \cos(2\pi l), & p \geq P_{i}, \end{cases} \tag{7}$$

where p is a random number in $[-1, 1]$. When $|\vec{A}| < 1$ and $p < P_{i}$, the current position of $\vec{X}_{*}^{d}(t)$ means the $\vec{X}_{\text{best}}^{d}(t)$, and the whale updates the formula of encircling its prey.

Otherwise, the agent updates the position by the randomly selected reference whale.

2.2. Elite Strategy.

According to the position of the original population $\vec{X}$, we introduce a new population $\vec{X_1}$, according to the value of fitness $Fitness_1$. Then, $\vec{X}$ and $\vec{X_1}$ are combined to form the population $\vec{X_2}$ sorted by fitness $Fitness_2$, and the top N is selected. The pseudocode of elite strategy is shown in Algorithm 1.

We know that the population obtained by random initialization can satisfy the search in the global solution, but such a search is not targeted. If the invalidity of some spatial regions has been proved during the first initialization, it is still possible to search for these useless regions when the random search is performed again, which leads to a waste of resources. The addition of the elite strategy can solve this problem better. While satisfying the global search, the population search will not search the invalid solution space again after the population search again but search again in the space where the optimal solution may exist, which can improve the efficiency of the algorithm to a greater extent. Through the elite strategy, new populations are generated by ranking the original populations according to their fitness values, after which the two are combined and from which the optimal top N populations of individuals are then selected. Doing so is the selection of the optimal individuals each time and ultimately improves the overall population quality.

2.3. Moth Flame Optimization (MFO).

MFO is a new swarm intelligence optimization algorithm proposed by Xu et al. [12, 108, 109]. It is inspired by the unique flight mode of moth named transverse orientation for navigation at night. In this algorithm, the set of moths M can be illustrated as

$$\vec{M} = \begin{bmatrix} \vec{M}_{11} & \cdots & \vec{M}_{1j} \\ \vdots & \cdots & \vdots \\ \vec{M}_{i1} & \cdots & \vec{M}_{ij} \end{bmatrix}, \qquad (8)$$

where $\vec{M}_{ij}$ is the j-th position corresponding to the i-th moth. Assuming the flame set is $\vec{F}$, $\vec{F}_{ij}$ is the j-th position corresponding to the i-th flame, and the flame set can be expressed as follows:

$$\vec{F} = \begin{bmatrix} \vec{F}_{11} & \cdots & \vec{F}_{1j} \\ \vdots & \cdots & \vdots \\ \vec{F}_{i1} & \cdots & \vec{F}_{ij} \end{bmatrix}. \qquad (9)$$

Each agent updates its position according to the following expression:

$$\vec{M}_i = \vec{S}\left(\vec{M}_i, \vec{F}_i\right), \qquad (10)$$

where $\vec{M}_i$ is the i-th moth, $\vec{F}_i$ is the i-th flame, and $\vec{S}$ is the helix function.

$$\vec{S}\left(M_i, F_j\right) = \vec{D}_i \cdot e^{bt} \cdot \cos(2\pi t) + \vec{F}_j, \qquad (11)$$

where $\vec{D}_i$ denotes the linear distance between the i-th moth and the j-th flame; b means the defined helix shape constant; t denotes a random number in the interval $[-1, 1]$.

To help the moth escape from the local optimum, the number of flames will decrease during the iteration:

$$\text{flame.no} = \text{round}\left[N - l \times \frac{N-1}{T}\right], \qquad (12)$$

where l denotes the number of the current iteration; N means the maximum quantity of flames; T means the maximum quantity of iterations.

The process of MFO is summarized as follows:

(1) Initialize the population and calculate the fitness values of the population

(2) The fitness values are sorted; calculate the location of the flame and its fitness value

(3) Calculate the number of flames according to equation (12)

(4) Calculate the linear distance between the moth and the corresponding flame and substitute it into equation (11) to obtain the updated value

(5) Calculate the fitness value according to the updated moth population

(6) Judge whether the termination condition is met; otherwise, jump to Step 2

The strategies in the MFO give good access to the most optimal population individuals, i.e., the corresponding flame positions. Because the flame position is obtained with respect to the moth population, the flame position is obtained after the fitness value is calculated and ranked for the moth individuals, and with iteration, the flame position is selected only for the better individuals in the moth population. Therefore, applying MFO to WOA can effectively enhance the local search capability of the algorithm.

3. Proposed Method

In this section, the MEWOA is illustrated in detail. The flowchart of the proposed MEWOA is presented in Figure 1. MEWOA incorporates the elite strategy and MFO algorithm for balancing the capability of exploration and exploitation. The algorithm first uses an elite strategy to generate a high-quality candidate population. Based on this population, the MFO algorithm is used to form a better population, which can help the algorithm possess the fast convergence, find out the optimal solution, and effectively avoid premature stagnation. The pseudocode of MEWOA is illustrated in Algorithm 2.

The computational complexity of MEWOA is due to the population size (N), dimension size (Dim), and maximum evaluation iterations (Max_FEs). Iteration number (l) is related to the maximum evaluation number and population size, $l = Max\_FEs/N$. Time complexity expression: $O(\text{MEWOA}) = O(\text{evaluation of the fitness}) + t \times (O(\text{elite}$

Calculate the fitness of the original population $Fitness_1$;
Sort $Fitness_1$ and rearrange $\overrightarrow{X}$ by serial number to get $\overrightarrow{X}_1$;
Combine $\overrightarrow{X}$ and $\overrightarrow{X}_1$ to form $\overrightarrow{X}_2$;
Calculate the fitness of the population $\overrightarrow{X}_2$ recorded as $Fitness_2$;
Sort $Fitness_2$ and select the top N;

ALGORITHM 1: Pseudocode of elite strategy.
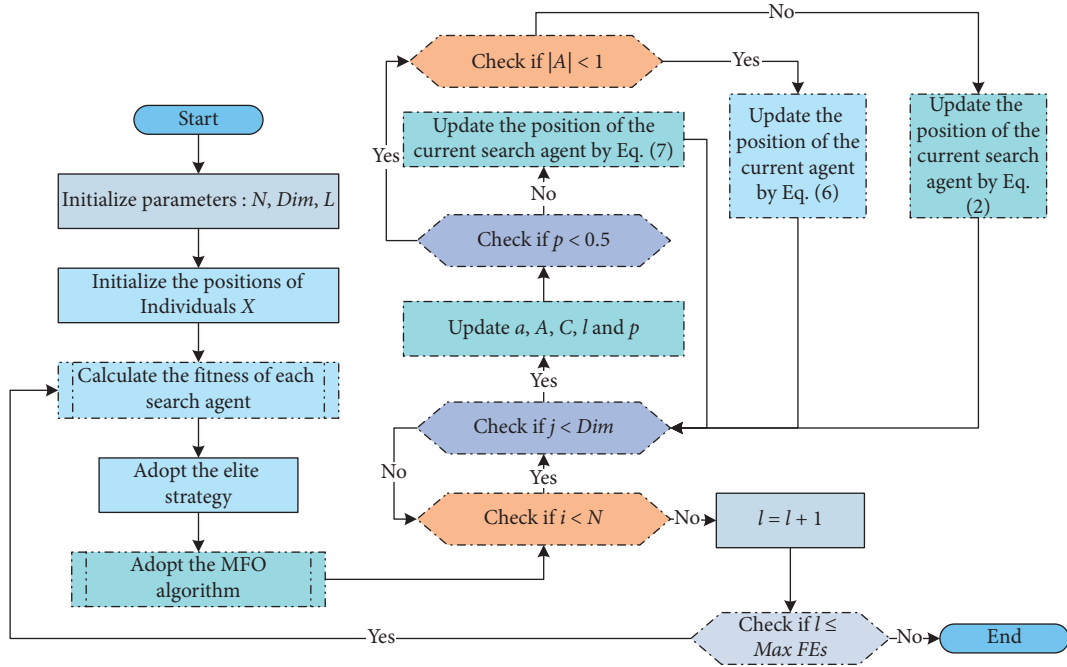
FIGURE 1: Flowchart of MEWOA.

Initialize the population $\overrightarrow{X}_i\,(i = 1, 2, \ldots, N)$, N, l, dim, Max_FEs
Calculate the fitness of each search agent
$\overrightarrow{X}^*$ = the best search agent
while ($l \leq Max\_FEs$)
    Adopt the Elite strategy
    Adopt the MFO algorithm
    for each whale
        Update $\overrightarrow{a}$, $\overrightarrow{A}$, $\overrightarrow{C}$, l and p
        if ($p < 0.5$)
            if ($|\overrightarrow{A}| < 1$)
                Update the position of the current agent by the equation (5)
            elseif ($|\overrightarrow{A}| \geq 1$)
                Select a random search agent ($\overrightarrow{X}_{rand}$)
                Update the position of the current search agent by equation (2)
            end if
        elseif ($p \geq 0.5$)
            Update the position of the current search agent by equation (6)
        end if
    end for
Check if any search agent goes beyond the search space and amend it
Calculate the fitness of each search agent
Update $\overrightarrow{X}^*$ if there is a better solution $l = l + 1$
end while
return $\overrightarrow{X}^*$

ALGORITHM 2: Pseudocode of MEWOA algorithm.

strategy) $+ O(MFO) + O($ estimation of the fitness $) + O(WOA))$. The complexity of the estimation of the fitness is $O(N)$, the complexity of elite strategy is $O(0)$, the complexity of MFO is $O(N \times Dim)$, and the complexity of WOA is $O(N \times Dim)$. So, the whole time complexity is $O(MEWOA) = O(N) + O(2 \times N \times Dim + N) \times t$. The time complexity of the original WOA is $O(WOA) = t \times (O($evaluation of the fitness$) + O(WOA))$. So, the whole complexity of the original WOA is $O(WOA) = t \times (O(N) + O(N \times Dim))$. The increased complexity compared to the two is $O(N) + O(N \times Dim) \times t$.

4. Experimental Studies

In this section, we further verify the performance of MEWOA. Firstly, the combination of strategies and the stability of the algorithm is analyzed. Next, on the CEC 2017 competition data set, we adopt several advanced versions of WOA as a comparison. At last, the algorithm is applied to three practical engineering problems.

The related experiments are conducted under the Windows Server 2012 R2 operating system adopting MATLAB R2014a software, and the hardware platform is configured with Intel (R) Xeon (R) Sliver 4110 CPU (2.10 GHz) and 16 GB RAM.

4.1. Benchmark Functions and Performance Evaluation Measures. This experiment adopts the IEEE CEC 2017 competition data set as a test function, which can effectively estimate the algorithm's ability. To ensure the experiment's fairness, the involved algorithms are evaluated under the same conditions: the overall scale and the maximal iteration numbers are set as 300000 and 150000, respectively. This is to ensure there is no bias and unfair setting that make the tests toward a specific method, as per artificial intelligence works [110–112]. The related algorithms are estimated 30 times on each benchmark function independently. Friedman's test [113] is a nonparametric statistical comparison test that can evaluate the experimental results. It is usually utilized to seek the difference between multiple test results and rank all algorithms' average performance to make a statistical comparison and get the ARV value (average ranking value). For the statistical test, paired Wilcoxon signed-rank test [114] is also adopted in this experiment. Wilcoxon signed-rank test can compare the performance between two algorithms. When the p value is less than 0.05, it indicates that the performance of MEWOA is statistically significantly improved compared to another algorithm.

4.2. Impacts of Components. MEWOA is a novel group intelligence algorithm introducing the two mechanisms of the MFO [108] algorithm and Elite Opposition-Based Learning (EOBL) [115] into the basic WOA. To better understand the influence of each mechanism on the performance of the WOA, we compare the model MWOA after the MFO algorithm, the EWOA model after the EOBL mechanism, and the MEWOA model after the two mechanisms which are integrated at the same time to study the

TABLE 1: Various WOAs with seven strategies.

	M	O
WOA	0	0
MWOA	1	0
EWOA	0	1
MEWOA	1	1

impact of each mechanism on the algorithm. In Table 1, "M" represents the MFO algorithm, and "E" represents the EOBL mechanism. Furthermore, "1" indicates that this mechanism is used in the WOA algorithm, and "0" indicates that the corresponding mechanism is not used. Table 2 reveals the test data of the four algorithms in the CEC2017 [116] functions. This experiment is carried out under the same condition. The dimension is set to 30, the number of particles is set to 30, and the maximum number of evaluations is set to 150,000 times. For obtaining the average results, each algorithm is run 30 times independently.

We test the impact of different mechanisms on the algorithm on 30 benchmark functions in CEC2017. Table 2 shows the comparison results of various models. We have listed the average results and standard deviations of different algorithms running on the test function 30 times, and the optimal values are shown in bold. On 30 test functions, the improved algorithm MEWOA has achieved the optimal solutions on most functions. MEWOA has significant advantages compared with MWOA and EWOA. The experimental results reveal that the MFO algorithm and EOBL mechanism added to the WOA algorithm can effectively enhance the performance of the original WOA and enhance the ability to search for optimal solutions.

To further study the improved MEWOA algorithm's performance, we performed the following analytical experiments on the CEC2017 functions. Figure 2 demonstrates the results of the feasibility analysis of MEWOA, where the original WOA algorithm is chosen for comparison. The graph in the first column (a) shows the three-dimensional location distribution of the MEWOA search history. The second column (b) graph reveals the two-dimensional location distribution of the MEWOA search history. The graph in the third column (c) shows the trajectory of MEWOA during the iterative process. The graph in the fourth column (d) shows the average fitness variation over the iterative process. The graph in the fifth column (e) demonstrates the convergence curve of the algorithm.

The black dots in Figure 2(b) show the algorithm's historical search positions, and the red dots show the optimal solutions' positions. It can be visualized from the figure that most of the black dots are clustered around the red dots, and a small portion of the black dots are scattered all over the solution space. The individual trajectories in Figure 2(c) show that the individuals fluctuate significantly in the first and middle stages and gradually stabilize in the later stages. Both data show that the algorithm can search the whole solution space as much as possible and then determine the region where the optimal solution is located for further exploitation. Figure 2(d) shows that the algorithm's average fitness curve maintains a constant decline throughout the

TABLE 2: Comparison results of MEWOA and other variants.

Fun	Item	MEWOA	EWOA	MWOA	MFO	WOA
F1	AVG	$1.1402E + 05$	$6.2606E + 09$	$5.1740E + 07$	$1.1003E + 10$	$2.8434E + 07$
	STD	$3.3373E + 05$	$3.1034E + 09$	$6.9757E + 07$	$8.7195E + 09$	$2.4863E + 07$
F2	AVG	$1.0140E + 13$	$2.8712E + 36$	$8.7045E + 26$	$4.5123E + 37$	$8.1117E + 25$
	STD	$2.1249E + 13$	$1.3645E + 37$	$4.7319E + 27$	$1.6948E + 38$	$4.0528E + 26$
F3	AVG	$1.3903E + 04$	$2.5163E + 05$	$2.1779E + 05$	$7.4876E + 04$	$2.0430E + 05$
	STD	$6.9178E + 03$	$9.5273E + 04$	$6.2175E + 04$	$6.8751E + 04$	$7.3817E + 04$
F4	AVG	$5.3104E + 02$	$1.4024E + 03$	$5.8750E + 02$	$1.5023E + 03$	$5.6894E + 02$
	STD	$5.0035E + 01$	$8.0323E + 02$	$3.9813E + 01$	$8.8614E + 02$	$3.5987E + 01$
F5	AVG	$7.0209E + 02$	$8.4901E + 02$	$7.9324E + 02$	$7.1606E + 02$	$7.8909E + 02$
	STD	$5.8959E + 01$	$6.3694E + 01$	$5.7745E + 01$	$6.4386E + 01$	$6.8153E + 01$
F6	AVG	$6.4492E + 02$	$6.7827E + 02$	$6.7206E + 02$	$6.3434E + 02$	$6.7004E + 02$
	STD	$1.1187E + 01$	$1.5775E + 01$	$1.2419E + 01$	$1.2633E + 01$	$9.8938E + 00$
F7	AVG	$9.6106E + 02$	$1.3466E + 03$	$1.2272E + 03$	$1.1855E + 03$	$1.2408E + 03$
	STD	$7.5270E + 01$	$7.6342E + 01$	$6.9796E + 01$	$2.1546E + 02$	$7.6205E + 01$
F8	AVG	$9.9622E + 02$	$1.0891E + 03$	$1.0221E + 03$	$1.0117E + 03$	$1.0283E + 03$
	STD	$4.8523E + 01$	$5.7098E + 01$	$4.4966E + 01$	$5.7584E + 01$	$5.3755E + 01$
F9	AVG	$5.3323E + 03$	$1.5001E + 04$	$9.0558E + 03$	$7.5359E + 03$	$9.2026E + 03$
	STD	$2.2701E + 03$	$6.2589E + 03$	$3.4108E + 03$	$1.6460E + 03$	$4.3758E + 03$
F10	AVG	$5.3003E + 03$	$7.9193E + 03$	$6.3360E + 03$	$5.7461E + 03$	$6.5544E + 03$
	STD	$6.1006E + 02$	$7.5830E + 02$	$7.4958E + 02$	$8.7887E + 02$	$8.6284E + 02$
F11	AVG	$1.2985E + 03$	$5.7913E + 03$	$2.3611E + 03$	$6.5666E + 03$	$2.4914E + 03$
	STD	$5.9662E + 01$	$2.8798E + 03$	$1.2251E + 03$	$5.7601E + 03$	$1.3764E + 03$
F12	AVG	$2.8637E + 06$	$1.8066E + 08$	$1.0806E + 08$	$4.1075E + 08$	$6.9061E + 07$
	STD	$1.8477E + 06$	$1.2913E + 08$	$6.0636E + 07$	$7.4554E + 08$	$5.6292E + 07$
F13	AVG	$3.1678E + 04$	$8.7338E + 07$	$1.7061E + 05$	$3.8575E + 07$	$1.4739E + 05$
	STD	$2.2382E + 04$	$2.9375E + 08$	$1.1901E + 05$	$1.9330E + 08$	$7.3276E + 04$
F14	AVG	$6.1824E + 04$	$1.9699E + 06$	$1.3829E + 06$	$2.1637E + 05$	$1.1689E + 06$
	STD	$3.6973E + 04$	$2.6824E + 06$	$1.8840E + 06$	$3.7891E + 05$	$1.1808E + 06$
F15	AVG	$1.7080E + 04$	$3.5083E + 06$	$9.6559E + 04$	$6.0508E + 04$	$9.2638E + 04$
	STD	$1.2528E + 04$	$5.9417E + 06$	$7.1048E + 04$	$5.7199E + 04$	$8.3603E + 04$
F16	AVG	$2.7163E + 03$	$4.0865E + 03$	$3.6880E + 03$	$3.2619E + 03$	$3.6476E + 03$
	STD	$3.2745E + 02$	$7.3533E + 02$	$4.0789E + 02$	$4.4991E + 02$	$4.8167E + 02$
F17	AVG	$2.2809E + 03$	$2.9371E + 03$	$2.5306E + 03$	$2.5576E + 03$	$2.5618E + 03$
	STD	$1.9868E + 02$	$4.9570E + 02$	$2.3127E + 02$	$2.9339E + 02$	$3.1216E + 02$
F18	AVG	$8.2210E + 05$	$1.2431E + 07$	$2.9497E + 06$	$4.0601E + 06$	$2.9801E + 06$
	STD	$8.9710E + 05$	$1.2645E + 07$	$4.0345E + 06$	$7.8932E + 06$	$2.5286E + 06$
F19	AVG	$2.2487E + 04$	$1.5354E + 07$	$5.5705E + 06$	$1.8640E + 07$	$5.6004E + 06$
	STD	$2.0128E + 04$	$5.8271E + 07$	$4.0800E + 06$	$4.0707E + 07$	$4.8343E + 06$
F20	AVG	$2.7115E + 03$	$3.0666E + 03$	$2.8007E + 03$	$2.6387E + 03$	$2.7859E + 03$
	STD	$2.2438E + 02$	$2.3437E + 02$	$2.1679E + 02$	$2.1030E + 02$	$1.4944E + 02$
F21	AVG	$2.4777E + 03$	$2.6424E + 03$	$2.5940E + 03$	$2.4995E + 03$	$2.5964E + 03$
	STD	$4.7650E + 01$	$8.0860E + 01$	$6.7087E + 01$	$5.0812E + 01$	$6.4482E + 01$
F22	AVG	$6.4893E + 03$	$9.1461E + 03$	$6.1745E + 03$	$6.6092E + 03$	$7.2471E + 03$
	STD	$1.6129E + 03$	$8.4869E + 02$	$2.2847E + 03$	$1.2145E + 03$	$1.6189E + 03$
F23	AVG	$2.8732E + 03$	$3.1343E + 03$	$3.0388E + 03$	$2.8338E + 03$	$3.0702E + 03$
	STD	$6.2221E + 01$	$8.9745E + 01$	$1.2308E + 02$	$5.2984E + 01$	$1.0063E + 02$
F24	AVG	$3.0054E + 03$	$3.2910E + 03$	$3.1764E + 03$	$2.9872E + 03$	$3.1805E + 03$
	STD	$5.8026E + 01$	$9.0717E + 01$	$8.1690E + 01$	$3.0441E + 01$	$8.1683E + 01$
F25	AVG	$2.9082E + 03$	$3.2249E + 03$	$2.9964E + 03$	$3.3361E + 03$	$2.9930E + 03$
	STD	$2.0562E + 01$	$1.6505E + 02$	$3.8915E + 01$	$5.1024E + 02$	$4.4618E + 01$
F26	AVG	$5.8834E + 03$	$8.6678E + 03$	$7.9037E + 03$	$5.8878E + 03$	$7.7769E + 03$
	STD	$5.5664E + 02$	$8.9188E + 02$	$1.2502E + 03$	$5.5639E + 02$	$7.8980E + 02$
F27	AVG	$3.4081E + 03$	$3.8352E + 03$	$3.4215E + 03$	$3.2540E + 03$	$3.3830E + 03$
	STD	$1.1014E + 02$	$3.2857E + 02$	$1.0341E + 02$	$2.9023E + 01$	$9.0797E + 01$
F28	AVG	$8.8194E + 03$	$7.5059E + 03$	$3.3450E + 03$	$4.4173E + 03$	$3.3436E + 03$
	STD	$1.0576E + 03$	$1.5877E + 03$	$3.7885E + 01$	$1.0738E + 03$	$3.3948E + 01$
F29	AVG	$4.0622E + 03$	$5.1185E + 03$	$5.0380E + 03$	$3.9958E + 03$	$5.0393E + 03$
	STD	$2.5075E + 02$	$4.3072E + 02$	$4.9458E + 02$	$2.2794E + 02$	$5.9330E + 02$
F30	AVG	$3.7243E + 04$	$8.7945E + 06$	$2.2134E + 07$	$1.0549E + 06$	$1.6396E + 07$
	STD	$2.6056E + 04$	$7.8295E + 06$	$1.9372E + 07$	$1.9420E + 06$	$1.9789E + 07$
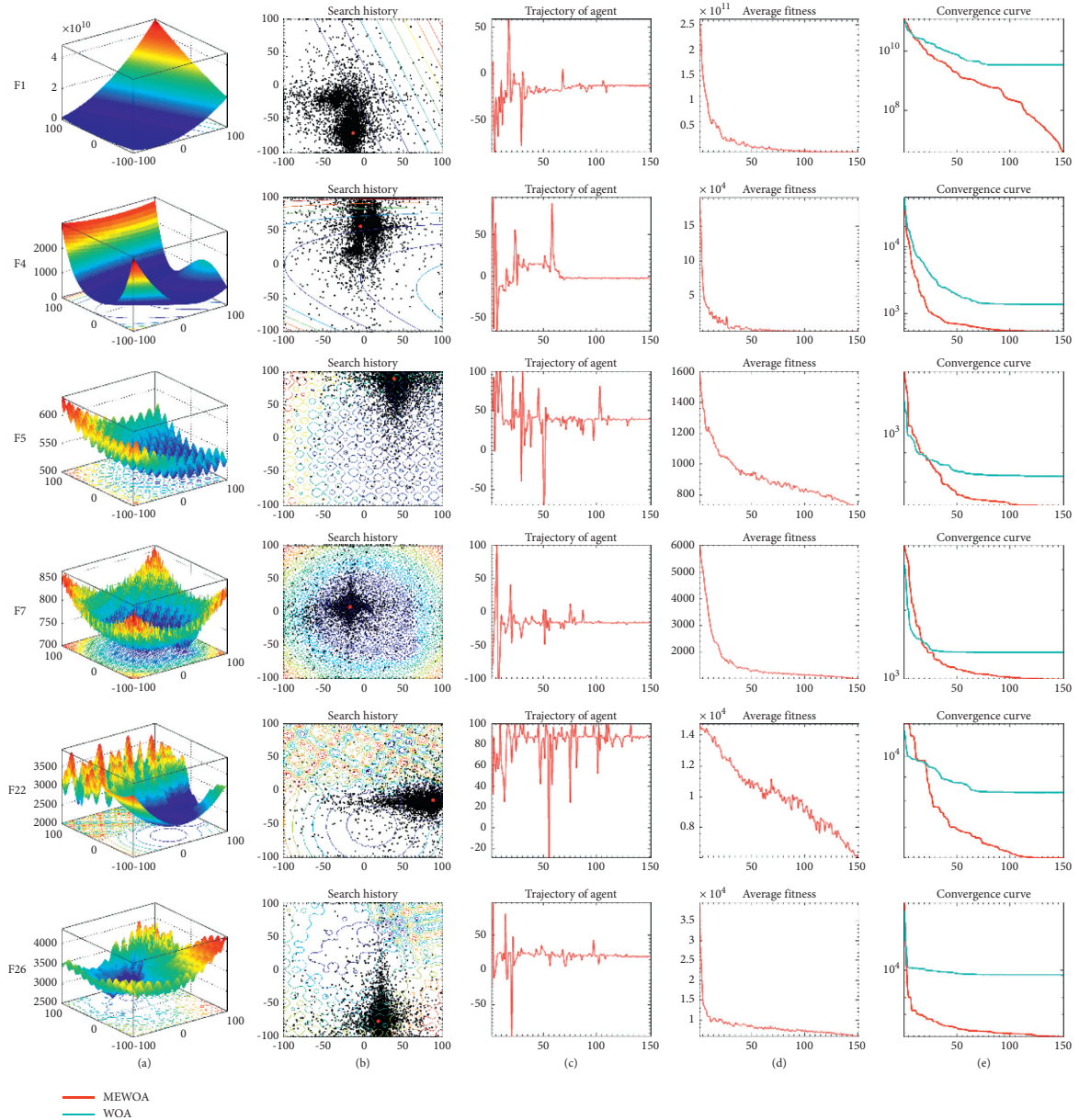
FIGURE 2: (a) Three-dimensional location distribution of MEWOA, (b) two-dimensional location distribution of MEWOA, (c) trajectory of MEWOA in the first dimension, (d) average fitness of MEWOA, and (e) convergence curves of algorithms.

iterations. F1, F4, F7, and F26 fall to lower fitness values early in the iteration. It shows that the algorithm exhibits good convergence ability on these functions. In Figure 2(e), it is more evident from the convergence curves of the two algorithms that MEWOA can find solutions with better quality.

This paper also analyzes the balance and diversity of these two algorithms on the CEC 2017 functions. Figure 3 demonstrates the results of the balanced analysis of MEWOA and WOA. The red and blue curves in the figure represent the exploration effect and exploitation effect, respectively. The higher the value of the curve, the more dominant the corresponding effect. A third curve is added to visualize the relationship between the two effects more clearly. When the value of the exploration effect is higher than or equal to the exploitation

effect, the curve increases. Otherwise, the curve decreases. When the curve decreases to a negative value, it is set to zero.

The general algorithm always performs a global search first and then develops the target area locally after the target area is identified. Therefore, in the algorithm's balance analysis curve, the exploration curve always starts with a higher value, and MEWOA has no exception. From Figure 3, we can see that the exploration and exploitation curves of both algorithms fluctuate considerably. The exploitation effect occupies most of the time in both. On the selected functions, the exploration phase of MEWOA ends significantly earlier than that of WOA. The exploitation curves have been increasing since then, indicating that MEWOA spends more time exploiting the target area.

Figure 4 reveals the change of the algorithm diversity during the optimization process. From the figure, we can

clearly see that the algorithm shows high population diversity at the beginning due to its random initialization. As the iterations progress, the algorithm keeps narrowing the search and reduces the population diversity. From the figure, we can see that the diversity curves of MEWOA and WOA are relatively similar. We know that both elite selection and MFO will make the algorithm converge faster in the early stage, and the population diversity will decline rapidly. However, the encircling mechanism, random search mechanism, and unique update method of WOA fluctuate between global and local during exploration. This success prevents MEWOA from converging too quickly in the early stage.

4.3. Scalability Test.
To test the MEWOA algorithm's performance for searching the optimal solution in different dimensions, we conducted the test in two dimensions of 50 and 100 and compared it with six other algorithms. In the experiment, the number of particles is set to 30. The maximum number of evaluations is set to 150,000 times. Each algorithm is independently run 30 times to take the average, and the CEC2017 test function is selected. The related results are demonstrated in Table 3, where AVG denotes the results' average, and STD means the standard deviation. Compared with other algorithms, the data shows that MEWOA has excellent advantages in processing single-mode functions in 50 and 100 dimensions. The improved MEWOA possesses more excellent performance than the other six improved WOA algorithms and also has a powerful ability to search for optimal solutions.

4.4. Comparison with Well-Established Methods.
To investigate the improved MEWOA algorithm's performance and advantages in this paper, a comparative test is made with several improved WOA. These algorithms are very successful improved WOA with excellent search performance. In the test, the dimension of the particles is set to 30, the number of particles is set to 30, the maximum number of evaluations is set to 150,000 times, each algorithm is independently run 30 times to take the average, and the test function selects the CEC2017 test function. Table 4 lists the involved algorithms' comparison results using the average and standard deviation of each algorithm running 30 times on different test functions. The table reveals that the average and standard deviations obtained from the improved MEWOA in this paper are smaller than other comparison algorithms.

We use the Friedman [113] test to rank the algorithms' performance and the Friedman test to find the difference between the results of multiple tests, which are nonparametric statistical comparative tests. The Friedman test ranks the average scores of the involved algorithms and then conducts further statistical comparisons to obtain ARV (average ranking values) from the results. It can be realized from Table 4 that the enhanced algorithm in this paper possesses better performance than other comparison algorithms in test functions except for F22, F27, and F28. Wilcoxon's [114] rank-sum test is also utilized in this paper to test whether MEWOA is superior to the comparison algorithm. As the p value is less than 0.05, we can realize that the MEWOA is significantly better than the

comparison algorithm in the current test function. As shown in Table 4, the p value of MEWOA is less than 0.05 on most test functions, so the improved algorithm in this paper is better than other compared algorithms on most test functions.

Convergence speed and convergence accuracy are important indicators for investigating the performance of evolutionary algorithms. We have selected six representative test functions for learning the algorithm's effectiveness and search trends more quickly and clearly, which are shown in Figure 5, namely, F1, F10, F12, F18, F26, and F30. It can be seen that on test functions F1, F12, F18, and F30, the improved algorithm in this paper has not converged to the optimal value after 150,000 evaluations, and the convergence trend is much higher than other comparison algorithms. In all cases, the convergence accuracy of the MEWOA is greater than the peers.

4.5. Comparison with Representative Metaheuristic Algorithms.
To better verify the performance of MEWOA, in this section, we will select some representative metaheuristics to compare with MEWOA. Among the algorithms involved in the comparison, there are classical algorithms, such as DE, as well as algorithms with good results proposed in the past years, such as MFO, and new algorithms proposed in recent years, such as SMA. The details are shown as follows.

(i) HHO

(ii) SMA

(iii) Hunger games search (HGS) [67]

(iv) DE

(v) MFO

(vi) Cuckoo search (CS) [117]

(vii) Grasshopper optimization algorithm (GOA) [118]

The parameters of the experiments were set approximately the same as the previous experiments. The dimension of particles was set to 30, the number of particles was set to 30, and the maximum number of evaluations was set to 300,000. The test function is IEEE CEC2017. Table 5 lists the experimental results of this experiment. In Table 5, AVG denotes the average value obtained for each algorithm after 30 independent tests on the corresponding function, STD denotes the corresponding standard deviation, and Rank denotes the ranking of the algorithm on each function. In addition, we used the Wilcoxon singed-rank test to calculate the p value on the algorithms, the purpose of which is to obtain whether there is variability in the comparison results of the two algorithms. If the p value is less than 0.05, it means that the comparison between MEWOA and the corresponding algorithm is statistically significant, and vice versa, it means that the results do not have any significance.

There are 30 functions in the CEC2017 test set, which are divided into 4 categories, among which, F1–F3 are Unimodal functions, F4–F10 are Multimodal functions, F11–F20 are Hybrid functions, and F21–F30 are Composition functions. In Figure 6, we have selected two functions from each class and depicted the convergence curves of MEWOA with other metaheuristic algorithms.
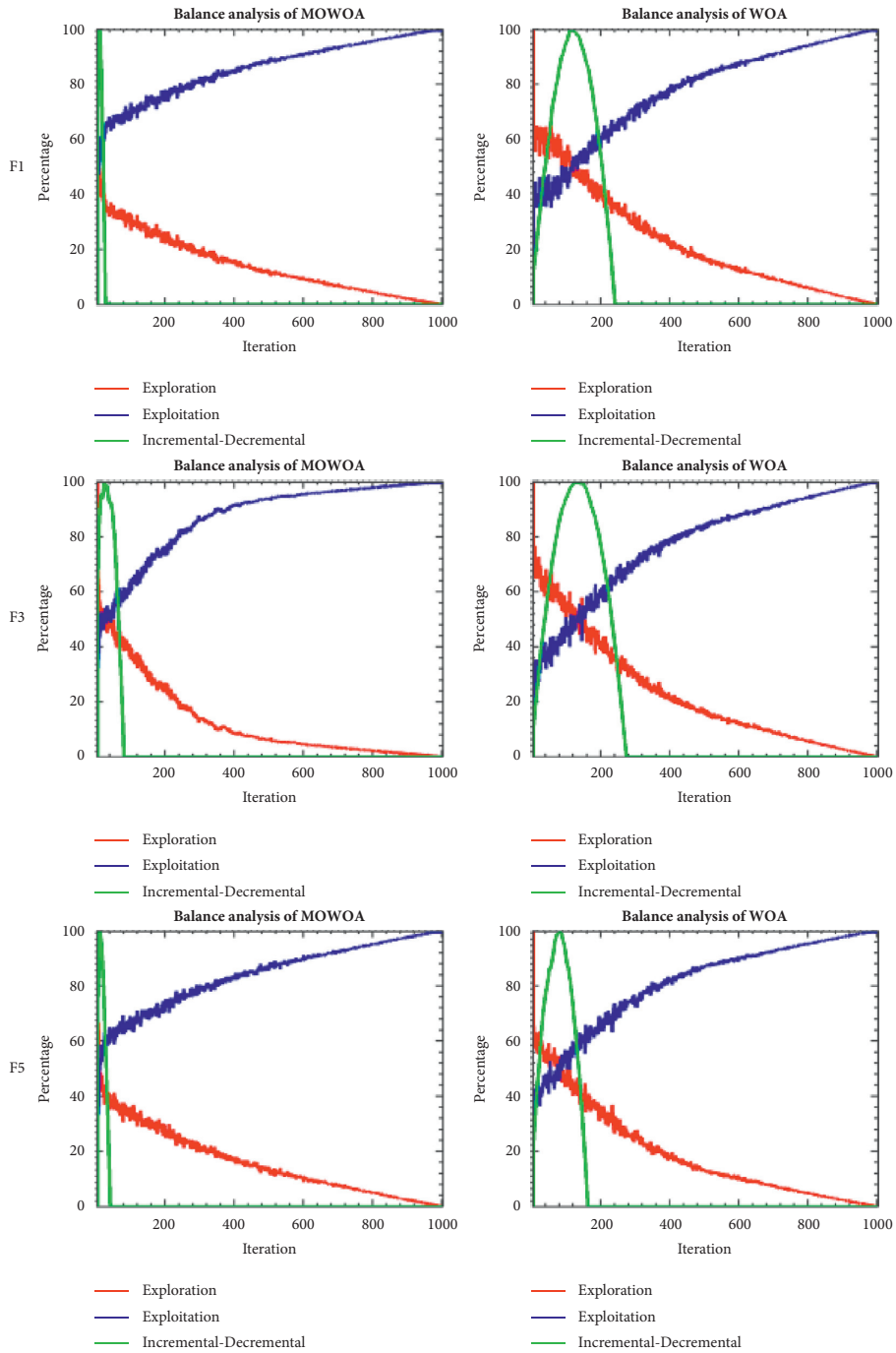
(a)

Figure 3: Continued.
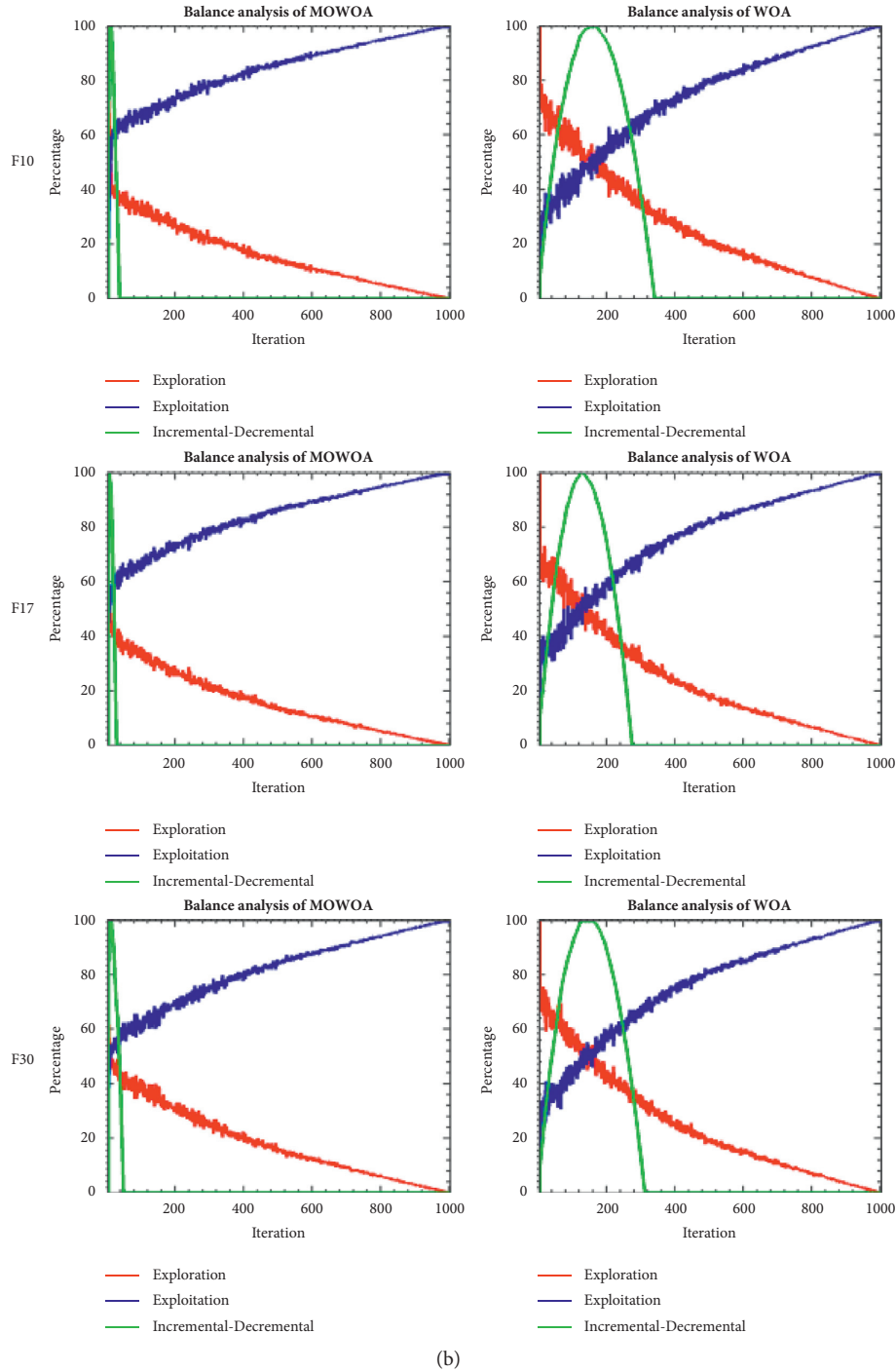
Figure 3: Balance analysis of algorithms.

On the Unimodal functions, the performance of MEWOA can be ranked in the middle among the listed algorithms; especially, for the F2 and F3 functions, MEWOA can be ranked third among all algorithms, exceeding the classical algorithm DE, so the overall results are still good.

On the Multimodal functions, MEWOA does not perform as well as on the Unimodal function, in terms of both convergence speed and convergence accuracy. However, on F10, its results are still relatively good. The final convergence accuracy can be ranked third. In addition, according to the picture, except for MFO, MEWOA can achieve a good convergence effect in the first half process iteration.

MEWOA has the best results on Hybrid functions, especially on F13, F16, F18, and F19, where MEWOA can be ranked second among all functions. According to the experimental results, it can also be found that the difference between the convergence accuracy of MEWOA and the first-ranked algorithm is not very large in the remaining functions.
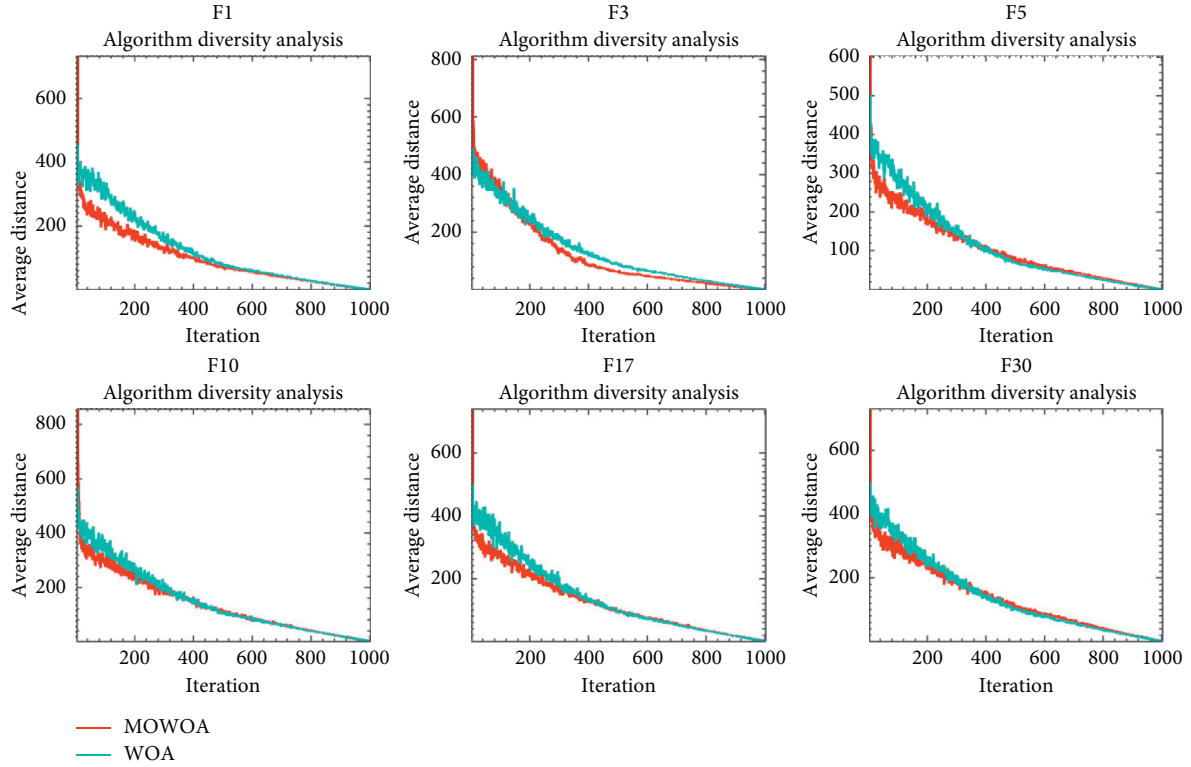
FIGURE 4: Diversity analysis of algorithms.

TABLE 3: Benchmark functions utilized in the scalability experiment.

Dim			MEWOA	OBWOA	ACWOA	BWOA	BMWOA	CCMWOA	CWOA
F1	50	AVG	$1.0377E+04$	$7.6546E+09$	$5.1362E+09$	$2.9030E+08$	$3.3981E+08$	$2.2425E+10$	$2.6554E+09$
		STD	$1.4448E+04$	$3.7797E+09$	$2.1333E+09$	$1.8009E+08$	$1.7216E+08$	$5.7702E+09$	$2.4349E+09$
	100	AVG	$3.4074E+04$	$6.1323E+09$	$3.8614E+09$	$3.5406E+07$	$6.4327E+07$	$1.6422E+10$	$1.6696E+09$
		STD	$1.4310E+05$	$3.9653E+09$	$1.6506E+09$	$2.4011E+07$	$3.1031E+07$	$3.8734E+09$	$1.7015E+09$
F2	50	AVG	$8.1668E+15$	$3.0916E+35$	$1.4866E+38$	$4.2055E+27$	$1.1327E+26$	$6.9725E+39$	$1.8395E+33$
		STD	$4.4713E+16$	$1.6677E+36$	$8.0871E+38$	$1.5488E+28$	$5.4122E+26$	$3.6879E+40$	$9.4663E+33$
	100	AVG	$5.4804E+12$	$2.6204E+32$	$6.2325E+35$	$3.1419E+25$	$3.1733E+20$	$1.7536E+38$	$4.9194E+32$
		STD	$1.5236E+13$	$7.3949E+32$	$3.1390E+36$	$1.6248E+26$	$8.8369E+20$	$9.4394E+38$	$2.6657E+33$
F3	50	AVG	$7.4126E+03$	$5.0041E+04$	$5.3069E+04$	$5.8975E+04$	$7.2088E+04$	$7.7685E+04$	$1.7950E+05$
		STD	$3.9238E+03$	$7.5664E+03$	$1.1922E+04$	$9.4105E+03$	$9.8742E+03$	$5.1149E+03$	$5.8222E+04$
	100	AVG	$2.5460E+03$	$4.6919E+04$	$4.8133E+04$	$5.1394E+04$	$6.0710E+04$	$7.4883E+04$	$1.4297E+05$
		STD	$3.3331E+03$	$1.2165E+04$	$1.1438E+04$	$1.3780E+04$	$9.0256E+03$	$6.3180E+03$	$4.3977E+04$
F4	50	AVG	$5.1424E+02$	$1.3102E+03$	$1.5099E+03$	$6.0628E+02$	$6.3457E+02$	$3.4367E+03$	$7.2047E+02$
		STD	$5.0383E+01$	$9.2372E+02$	$9.1177E+02$	$4.4055E+01$	$5.3049E+01$	$1.2448E+03$	$1.9633E+02$
	100	AVG	$5.0761E+02$	$1.0433E+03$	$9.3826E+02$	$5.6889E+02$	$5.6772E+02$	$2.8972E+03$	$6.1254E+02$
		STD	$3.0282E+01$	$5.8283E+02$	$2.5118E+02$	$2.9881E+01$	$3.5575E+01$	$1.6178E+03$	$1.0315E+02$
F5	50	AVG	$6.8660E+02$	$8.0334E+02$	$8.0383E+02$	$7.6877E+02$	$7.9177E+02$	$8.4123E+02$	$7.9951E+02$
		STD	$3.9567E+01$	$3.1435E+01$	$3.0546E+01$	$3.3178E+01$	$5.5888E+01$	$3.0406E+01$	$6.2931E+01$
	100	AVG	$6.7717E+02$	$7.9697E+02$	$7.8954E+02$	$7.5788E+02$	$7.7647E+02$	$8.1562E+02$	$8.2434E+02$
		STD	$3.3853E+01$	$2.7023E+01$	$2.6015E+01$	$3.4720E+01$	$4.7106E+01$	$3.5426E+01$	$6.2786E+01$
F6	50	AVG	$6.4280E+02$	$6.6924E+02$	$6.6517E+02$	$6.6566E+02$	$6.6621E+02$	$6.7035E+02$	$6.7652E+02$
		STD	$1.0910E+01$	$6.4989E+00$	$4.5122E+00$	$8.3904E+00$	$8.9785E+00$	$8.5912E+00$	$1.2226E+01$
	100	AVG	$6.3798E+02$	$6.6650E+02$	$6.6353E+02$	$6.6470E+02$	$6.6466E+02$	$6.7030E+02$	$6.7069E+02$
		STD	$1.1490E+01$	$6.1196E+00$	$6.8462E+00$	$8.2608E+00$	$9.3215E+00$	$8.2339E+00$	$1.1780E+01$

Table 3: Continued.

Dim			MEWOA	OBWOA	ACWOA	BWOA	BMWOA	CCMWOA	CWOA
F7	50	AVG	$9.6655E+02$	$1.2959E+03$	$1.2357E+03$	$1.2617E+03$	$1.2439E+03$	$1.2902E+03$	$1.2742E+03$
		STD	$7.1608E+01$	$4.4520E+01$	$6.1102E+01$	$7.9393E+01$	$9.3492E+01$	$6.4993E+01$	$7.4210E+01$
	100	AVG	$9.5751E+02$	$1.2807E+03$	$1.2236E+03$	$1.2400E+03$	$1.1750E+03$	$1.2622E+03$	$1.2446E+03$
		STD	$5.9145E+01$	$5.9135E+01$	$6.1447E+01$	$7.5216E+01$	$1.0336E+02$	$8.1953E+01$	$6.7215E+01$
F8	50	AVG	$1.0013E+03$	$1.0045E+03$	$1.0177E+03$	$9.8480E+02$	$1.0180E+03$	$1.0456E+03$	$1.0319E+03$
		STD	$5.5037E+01$	$2.5078E+01$	$2.6427E+01$	$2.7098E+01$	$2.4785E+01$	$2.7515E+01$	$4.2507E+01$
	100	AVG	$9.7555E+02$	$1.0016E+03$	$1.0081E+03$	$9.7816E+02$	$1.0067E+03$	$1.0300E+03$	$1.0347E+03$
		STD	$4.4852E+01$	$2.4995E+01$	$1.9787E+01$	$1.7740E+01$	$3.4795E+01$	$3.0539E+01$	$5.6612E+01$
F9	50	AVG	$5.8348E+03$	$7.3478E+03$	$7.1516E+03$	$6.2441E+03$	$7.8921E+03$	$7.9590E+03$	$8.8671E+03$
		STD	$1.9274E+03$	$1.1299E+03$	$9.7706E+02$	$8.7146E+02$	$1.3587E+03$	$1.4096E+03$	$2.5451E+03$
	100	AVG	$6.0388E+03$	$6.8714E+03$	$6.8865E+03$	$5.8989E+03$	$6.9697E+03$	$7.5847E+03$	$8.1388E+03$
		STD	$2.1690E+03$	$9.1811E+02$	$9.7778E+02$	$4.5234E+02$	$1.0148E+03$	$1.0859E+03$	$2.5020E+03$
F10	50	AVG	$5.2132E+03$	$6.3611E+03$	$6.6167E+03$	$6.7578E+03$	$7.7359E+03$	$7.0624E+03$	$6.0753E+03$
		STD	$7.9703E+02$	$6.9125E+02$	$9.1709E+02$	$9.4592E+02$	$5.4810E+02$	$5.8703E+02$	$8.2775E+02$
	100	AVG	$5.3579E+03$	$6.1734E+03$	$6.2137E+03$	$6.3582E+03$	$7.0292E+03$	$6.9010E+03$	$5.9492E+03$
		STD	$8.1114E+02$	$6.1867E+02$	$8.4074E+02$	$8.1917E+02$	$8.3520E+02$	$4.6039E+02$	$6.1961E+02$
F11	50	AVG	$1.2820E+03$	$2.7979E+03$	$3.0964E+03$	$1.8492E+03$	$1.7997E+03$	$3.4954E+03$	$3.5263E+03$
		STD	$6.2856E+01$	$1.2354E+03$	$9.3467E+02$	$3.5878E+02$	$2.1356E+02$	$1.2351E+03$	$1.6474E+03$
	100	AVG	$1.3139E+03$	$2.3188E+03$	$2.5542E+03$	$1.5523E+03$	$1.4788E+03$	$3.0025E+03$	$3.1462E+03$
		STD	$6.5062E+01$	$1.0241E+03$	$7.5378E+02$	$1.3554E+02$	$1.0288E+02$	$4.6619E+02$	$2.0175E+03$
F12	50	AVG	$2.0866E+06$	$5.4663E+08$	$7.0549E+08$	$1.3443E+08$	$1.0153E+08$	$3.1251E+09$	$2.1403E+08$
		STD	$1.3895E+06$	$7.9906E+08$	$7.4501E+08$	$8.6216E+07$	$5.7278E+07$	$2.0312E+09$	$6.0185E+08$
	100	AVG	$1.4145E+06$	$2.3280E+08$	$4.0570E+08$	$6.2528E+07$	$4.3622E+07$	$1.0572E+09$	$7.3297E+07$
		STD	$1.1317E+06$	$5.2068E+08$	$3.6694E+08$	$3.6693E+07$	$2.7375E+07$	$8.8761E+08$	$6.9963E+07$
F13	50	AVG	$2.8736E+04$	$3.2546E+05$	$5.8098E+07$	$3.1410E+05$	$5.3145E+05$	$1.7827E+08$	$1.5088E+05$
		STD	$2.0176E+04$	$3.3803E+05$	$1.0445E+08$	$1.7443E+05$	$3.7550E+05$	$4.2469E+08$	$8.2594E+04$
	100	AVG	$2.8030E+04$	$9.3162E+06$	$1.1670E+08$	$1.6722E+05$	$1.7872E+05$	$3.7303E+07$	$1.4285E+05$
		STD	$2.4067E+04$	$4.9866E+07$	$3.7689E+08$	$1.0720E+05$	$1.2190E+05$	$8.7842E+07$	$9.8340E+04$
F14	50	AVG	$3.9976E+04$	$1.4800E+06$	$9.9948E+05$	$1.2139E+06$	$8.1522E+05$	$1.4775E+06$	$1.4639E+06$
		STD	$2.2279E+04$	$1.1492E+06$	$8.4649E+05$	$1.6525E+06$	$7.5212E+05$	$1.2739E+06$	$1.3442E+06$
	100	AVG	$2.7654E+04$	$8.1587E+05$	$7.5986E+05$	$1.0263E+06$	$4.3235E+05$	$1.1574E+06$	$9.9956E+05$
		STD	$2.1704E+04$	$5.6323E+05$	$6.8474E+05$	$9.5288E+05$	$4.5036E+05$	$9.1787E+05$	$9.5781E+05$
F15	50	AVG	$1.9648E+04$	$1.9513E+06$	$1.0018E+07$	$2.3326E+05$	$1.2765E+05$	$4.7314E+06$	$6.6735E+06$
		STD	$1.5537E+04$	$3.0462E+06$	$1.3785E+07$	$5.3438E+05$	$1.5993E+05$	$1.0569E+07$	$1.5884E+07$
	100	AVG	$1.7258E+04$	$3.4231E+06$	$1.1297E+07$	$6.7191E+04$	$4.8208E+04$	$2.4340E+06$	$1.9551E+06$
		STD	$1.2602E+04$	$1.0657E+07$	$3.8329E+07$	$7.1976E+04$	$2.8165E+04$	$3.9738E+06$	$4.3858E+06$
F16	50	AVG	$2.6782E+03$	$3.9833E+03$	$3.9266E+03$	$3.9609E+03$	$3.4721E+03$	$4.3136E+03$	$3.7458E+03$
		STD	$3.7601E+02$	$5.5297E+02$	$3.5148E+02$	$6.4900E+02$	$4.1081E+02$	$7.4318E+02$	$5.3179E+02$
	100	AVG	$2.6047E+03$	$3.6881E+03$	$3.6697E+03$	$3.6417E+03$	$3.4681E+03$	$3.8127E+03$	$3.6832E+03$
		STD	$2.8196E+02$	$5.4792E+02$	$2.9038E+02$	$5.2779E+02$	$4.2993E+02$	$4.4155E+02$	$5.0216E+02$
F17	50	AVG	$2.3075E+03$	$2.6205E+03$	$2.6403E+03$	$2.6899E+03$	$2.5231E+03$	$2.7808E+03$	$2.6261E+03$
		STD	$2.9381E+02$	$3.1275E+02$	$1.8234E+02$	$2.4155E+02$	$2.2274E+02$	$3.5820E+02$	$2.3234E+02$
	100	AVG	$2.3092E+03$	$2.5878E+03$	$2.5663E+03$	$2.5445E+03$	$2.3901E+03$	$2.6705E+03$	$2.5358E+03$
		STD	$2.2490E+02$	$2.3905E+02$	$1.8353E+02$	$3.2721E+02$	$2.1330E+02$	$3.9669E+02$	$2.7897E+02$
F18	50	AVG	$4.8531E+05$	$2.7178E+06$	$4.9753E+06$	$4.7870E+06$	$3.9696E+06$	$1.0008E+07$	$5.2516E+06$
		STD	$3.6262E+05$	$4.3217E+06$	$4.9851E+06$	$3.6592E+06$	$4.1710E+06$	$8.7883E+06$	$5.2077E+06$
	100	AVG	$3.2319E+05$	$1.8524E+06$	$2.0466E+06$	$3.4255E+06$	$3.0443E+06$	$8.7689E+06$	$3.2644E+06$
		STD	$2.5201E+05$	$2.2250E+06$	$3.0810E+06$	$2.9805E+06$	$3.7768E+06$	$9.9315E+06$	$3.9346E+06$
F19	50	AVG	$2.0880E+04$	$1.1253E+06$	$1.4096E+07$	$4.5512E+06$	$8.4651E+05$	$4.9944E+06$	$2.4743E+06$
		STD	$2.0800E+04$	$9.3945E+05$	$2.3132E+07$	$3.8997E+06$	$8.9808E+05$	$4.0455E+06$	$2.5119E+06$
	100	AVG	$2.0597E+04$	$1.1714E+06$	$1.4314E+07$	$3.0040E+06$	$2.9342E+05$	$3.3380E+06$	$5.8437E+06$
		STD	$1.9606E+04$	$9.2106E+05$	$2.5721E+07$	$2.8549E+06$	$3.0967E+05$	$4.0676E+06$	$2.1544E+07$
F20	50	AVG	$2.5745E+03$	$2.7246E+03$	$2.6898E+03$	$2.7568E+03$	$2.7300E+03$	$2.7067E+03$	$2.8540E+03$
		STD	$2.1430E+02$	$2.3025E+02$	$1.3537E+02$	$1.9178E+02$	$1.8621E+02$	$2.1710E+02$	$2.0568E+02$
	100	AVG	$2.4905E+03$	$2.7821E+03$	$2.6152E+03$	$2.6534E+03$	$2.6362E+03$	$2.6471E+03$	$2.7217E+03$
		STD	$1.7572E+02$	$1.6627E+02$	$1.4973E+02$	$1.7623E+02$	$1.7958E+02$	$1.7418E+02$	$1.8903E+02$

Table 3: Continued.

Dim			MEWOA	OBWOA	ACWOA	BWOA	BMWOA	CCMWOA	CWOA
F21	50	AVG	$2.4895E+03$	$2.5943E+03$	$2.5948E+03$	$2.5885E+03$	$2.5353E+03$	$2.6227E+03$	$2.5933E+03$
		STD	$3.8874E+01$	$4.1381E+01$	$3.3573E+01$	$5.8174E+01$	$4.7024E+01$	$4.1343E+01$	$6.2363E+01$
	100	AVG	$2.4743E+03$	$2.5761E+03$	$2.5755E+03$	$2.5653E+03$	$2.5220E+03$	$2.6198E+03$	$2.5813E+03$
		STD	$5.4390E+01$	$8.4792E+01$	$3.2601E+01$	$5.3228E+01$	$4.5418E+01$	$4.8100E+01$	$6.8689E+01$
F22	50	AVG	$6.1490E+03$	$7.3173E+03$	$5.4178E+03$	$6.3144E+03$	$5.1290E+03$	$7.4041E+03$	$6.7333E+03$
		STD	$1.9016E+03$	$1.5471E+03$	$2.0351E+03$	$2.5268E+03$	$3.1716E+03$	$1.2267E+03$	$2.1379E+03$
	100	AVG	$6.3054E+03$	$6.7626E+03$	$4.2461E+03$	$7.4007E+03$	$3.9537E+03$	$7.1283E+03$	$6.9038E+03$
		STD	$1.0591E+03$	$1.9153E+03$	$1.7276E+03$	$1.3291E+03$	$2.4923E+03$	$1.2612E+03$	$1.9830E+03$
F23	50	AVG	$2.8555E+03$	$3.0652E+03$	$3.0611E+03$	$3.0740E+03$	$2.9303E+03$	$3.1941E+03$	$3.1005E+03$
		STD	$6.3711E+01$	$9.9008E+01$	$8.3564E+01$	$1.1219E+02$	$7.0249E+01$	$1.1891E+02$	$1.0485E+02$
	100	AVG	$2.8435E+03$	$3.1324E+03$	$3.0390E+03$	$3.0578E+03$	$2.9329E+03$	$3.1405E+03$	$3.0590E+03$
		STD	$6.7638E+01$	$1.0696E+02$	$5.5154E+01$	$1.0289E+02$	$8.3256E+01$	$9.6440E+01$	$1.0534E+02$
F24	50	AVG	$3.0137E+03$	$3.2187E+03$	$3.1779E+03$	$3.1921E+03$	$3.1348E+03$	$3.3436E+03$	$3.2694E+03$
		STD	$7.2441E+01$	$1.4166E+02$	$6.0225E+01$	$9.8612E+01$	$6.9010E+01$	$1.0411E+02$	$1.0534E+02$
	100	AVG	$3.0116E+03$	$3.1669E+03$	$3.2049E+03$	$3.1882E+03$	$3.1294E+03$	$3.2470E+03$	$3.2113E+03$
		STD	$5.9600E+01$	$1.0993E+02$	$6.6519E+01$	$7.7999E+01$	$8.2632E+01$	$9.4985E+01$	$9.6792E+01$
F25	50	AVG	$2.9101E+03$	$3.1393E+03$	$3.1633E+03$	$3.0363E+03$	$3.0378E+03$	$3.3893E+03$	$3.0620E+03$
		STD	$2.0120E+01$	$1.0600E+02$	$1.0642E+02$	$4.1774E+01$	$3.9266E+01$	$1.2506E+02$	$9.2411E+01$
	100	AVG	$2.9113E+03$	$3.0928E+03$	$3.1725E+03$	$2.9967E+03$	$2.9819E+03$	$3.2988E+03$	$3.0115E+03$
		STD	$2.2493E+01$	$9.9682E+01$	$1.3476E+02$	$3.9829E+01$	$3.2477E+01$	$1.2817E+02$	$4.7850E+01$
F26	50	AVG	$6.1456E+03$	$8.2881E+03$	$7.8116E+03$	$7.9608E+03$	$7.2504E+03$	$9.0684E+03$	$8.0177E+03$
		STD	$6.1830E+02$	$1.3386E+03$	$8.3893E+02$	$1.4155E+03$	$9.3993E+02$	$1.1007E+03$	$1.1973E+03$
	100	AVG	$5.6689E+03$	$8.1545E+03$	$7.5863E+03$	$7.5645E+03$	$6.4549E+03$	$8.3392E+03$	$7.7474E+03$
		STD	$5.3520E+02$	$1.2603E+03$	$7.4569E+02$	$1.6258E+03$	$1.3256E+03$	$1.1570E+03$	$1.0925E+03$
F27	50	AVG	$3.5106E+03$	$3.4028E+03$	$3.4759E+03$	$3.4213E+03$	$3.3410E+03$	$3.6205E+03$	$3.3903E+03$
		STD	$1.3443E+02$	$1.2973E+02$	$1.1189E+02$	$1.2788E+02$	$1.0546E+02$	$1.6440E+02$	$1.0062E+02$
	100	AVG	$3.4392E+03$	$3.3773E+03$	$3.4438E+03$	$3.3436E+03$	$3.3029E+03$	$3.5657E+03$	$3.3682E+03$
		STD	$1.0646E+02$	$8.9512E+01$	$8.9662E+01$	$8.8219E+01$	$3.6244E+01$	$1.3092E+02$	$9.3400E+01$
F28	50	AVG	$8.7622E+03$	$3.7920E+03$	$3.7604E+03$	$3.4125E+03$	$3.4177E+03$	$4.5930E+03$	$3.5357E+03$
		STD	$1.0609E+03$	$2.2475E+02$	$2.0019E+02$	$6.5309E+01$	$6.3955E+01$	$3.9731E+02$	$2.3404E+02$
	100	AVG	$8.2899E+03$	$3.7758E+03$	$3.6512E+03$	$3.3403E+03$	$3.3648E+03$	$4.3012E+03$	$3.4138E+03$
		STD	$1.0768E+03$	$2.6586E+02$	$1.7241E+02$	$3.8695E+01$	$3.6542E+01$	$4.0344E+02$	$9.2971E+01$
F29	50	AVG	$4.1814E+03$	$4.7997E+03$	$4.7766E+03$	$5.0867E+03$	$4.8669E+03$	$5.2353E+03$	$4.9032E+03$
		STD	$2.6819E+02$	$3.6532E+02$	$3.6033E+02$	$5.5228E+02$	$4.2425E+02$	$5.6003E+02$	$4.6297E+02$
	100	AVG	$4.0297E+03$	$4.6450E+03$	$4.5318E+03$	$4.9508E+03$	$4.6385E+03$	$5.2996E+03$	$4.8376E+03$
		STD	$2.6601E+02$	$3.6948E+02$	$2.8181E+02$	$3.1316E+02$	$3.0809E+02$	$6.6241E+02$	$4.7446E+02$
F30	50	AVG	$3.0309E+04$	$4.2253E+07$	$6.2921E+07$	$2.1406E+07$	$6.6288E+06$	$8.3127E+07$	$1.2808E+07$
		STD	$2.2691E+04$	$1.0790E+08$	$5.0098E+07$	$2.4931E+07$	$4.5636E+06$	$9.1773E+07$	$1.3470E+07$
	100	AVG	$1.7144E+04$	$5.9401E+07$	$4.2420E+07$	$1.6012E+07$	$4.4775E+06$	$5.1449E+07$	$1.1866E+07$
		STD	$7.9091E+03$	$1.7815E+08$	$3.1937E+07$	$1.3827E+07$	$3.6919E+06$	$3.8182E+07$	$6.9753E+06$

Finally, in the Composition functions, we can see that the results shown by MEWOA are still good in the convergence graphs of both F22 and F30 functions, especially in the F22 function, which can achieve a better solution than the other algorithms.

4.6. Comparison with Advanced Algorithms.

To further verify the performance of MEWOA, this section has selected some advanced algorithms to compare with MEWOA. Among the compared algorithms, champion algorithms, such as LSHADE, are included, as well as improved algorithms on DE, such as SADE, and algorithms with stronger performance, such as HCLPSO. The specific algorithms involved in the comparison are shown as follows.

(i) Adaptive DE with success-history and linear population size reduction (HCLPSO) [119]

(ii) Self-adaptive differential evolution (SADE) [120]

(iii) Adaptive differential evolution with optional external archive (JADE) [121]

(iv) Comprehensive learning particle swarm optimizer (CLPSO) [122]

(v) Adaptive DE with success-history and linear population size reduction (LSHADE) [123]

(vi) LSHADE_cnEpSi (LSHADE_ES) [124].

(vii) Multistrategy enhanced sine cosine algorithm (MSCA) [16]

The experimental parameters were set in the same way as in the previous section, and in addition, we have modified

TABLE 4: Comparison results of different peers.

		MEWOA	OBWOA	ACWOA	BWOA	BMWOA	CCMWOA	CWOA
F1	AVG	$1.1469E + 05$	$9.7743E + 09$	$7.8058E + 09$	$9.6529E + 08$	$1.0985E + 09$	$2.4867E + 10$	$4.0000E + 09$
	STD	$4.1160E + 05$	$4.1822E + 09$	$2.8798E + 09$	$6.1575E + 08$	$5.0173E + 08$	$5.0888E + 09$	$2.8487E + 09$
	Rank	1	6	5	2	3	7	4
	p value		$1.7344E - 06$	$1.7344E - 06$	$1.7344E - 06$	$1.7344E - 06$	$1.7344E - 06$	$1.7344E - 06$
F2	AVG	$8.1708E + 15$	$6.2853E + 34$	$9.2862E + 34$	$7.1393E + 30$	$1.0002E + 27$	$1.9200E + 41$	$1.0852E + 34$
	STD	$4.4709E + 16$	$2.4742E + 35$	$3.2104E + 35$	$2.7272E + 31$	$3.4542E + 27$	$9.9696E + 41$	$4.5433E + 34$
	Rank	1	5	6	3	2	7	4
	p value		$1.7344E - 06$	$1.7344E - 06$	$1.7344E - 06$	$1.7344E - 06$	$1.7344E - 06$	$1.7344E - 06$
F3	AVG	$1.3261E + 04$	$5.8532E + 04$	$5.3179E + 04$	$6.7334E + 04$	$8.1538E + 04$	$7.8703E + 04$	$1.9351E + 05$
	STD	$7.4562E + 03$	$7.9256E + 03$	$9.6568E + 03$	$9.6164E + 03$	$6.7204E + 03$	$6.4792E + 03$	$4.4523E + 04$
	Rank	1	3	2	4	6	5	7
	p value		$1.7344E - 06$	$1.7344E - 06$	$1.7344E - 06$	$1.7344E - 06$	$1.7344E - 06$	$1.7344E - 06$
F4	AVG	$5.1430E + 02$	$1.6724E + 03$	$1.4835E + 03$	$7.1171E + 02$	$7.3454E + 02$	$5.0608E + 03$	$1.0173E + 03$
	STD	$3.8031E + 01$	$9.9516E + 02$	$7.3853E + 02$	$1.3421E + 02$	$1.0306E + 02$	$1.3683E + 03$	$4.7652E + 02$
	Rank	1	6	5	2	3	7	4
	p value		$1.7344E - 06$	$1.7344E - 06$	$1.7344E - 06$	$1.7344E - 06$	$1.7344E - 06$	$1.7344E - 06$
F5	AVG	$6.8487E + 02$	$8.1524E + 02$	$8.1331E + 02$	$7.7250E + 02$	$8.0978E + 02$	$8.4433E + 02$	$8.1605E + 02$
	STD	$4.7570E + 01$	$3.3664E + 01$	$2.4957E + 01$	$4.0902E + 01$	$4.8970E + 01$	$3.4510E + 01$	$5.3895E + 01$
	Rank	1	5	4	2	3	7	6
	p value		$2.1266E - 06$	$1.9209E - 06$	$2.3704E - 05$	$2.6033E - 06$	$1.7344E - 06$	$2.1266E - 06$
F6	AVG	$6.4282E + 02$	$6.7097E + 02$	$6.7025E + 02$	$6.6603E + 02$	$6.6566E + 02$	$6.7218E + 02$	$6.7673E + 02$
	STD	$1.4507E + 01$	$5.7482E + 00$	$7.7197E + 00$	$7.1928E + 00$	$9.7165E + 00$	$6.8770E + 00$	$1.4458E + 01$
	Rank	1	5	4	3	2	6	7
	p value		$1.9209E - 06$	$2.1266E - 06$	$7.6909E - 06$	$2.8434E - 05$	$2.1266E - 06$	$4.2857E - 06$
F7	AVG	$9.6141E + 02$	$1.3112E + 03$	$1.2484E + 03$	$1.2622E + 03$	$1.2408E + 03$	$1.3043E + 03$	$1.2987E + 03$
	STD	$5.5626E + 01$	$6.2946E + 01$	$6.3206E + 01$	$7.4289E + 01$	$1.0208E + 02$	$6.1390E + 01$	$8.7682E + 01$
	Rank	1	7	3	4	2	6	5
	p value		$1.7344E - 06$	$1.7344E - 06$	$1.7344E - 06$	$1.7344E - 06$	$1.7344E - 06$	$1.7344E - 06$
F8	AVG	$9.7134E + 02$	$1.0202E + 03$	$1.0168E + 03$	$1.0079E + 03$	$1.0273E + 03$	$1.0640E + 03$	$1.0492E + 03$
	STD	$4.7508E + 01$	$2.8426E + 01$	$2.8267E + 01$	$2.9916E + 01$	$3.5155E + 01$	$2.7126E + 01$	$4.4532E + 01$
	Rank	1	4	3	2	5	7	6
	p value		$7.1570E - 04$	$3.5888E - 04$	$1.1973E - 03$	$3.0650E - 04$	$3.1817E - 06$	$1.7988E - 05$
F9	AVG	$5.3008E + 03$	$7.7529E + 03$	$7.6542E + 03$	$6.9325E + 03$	$8.1060E + 03$	$8.3760E + 03$	$9.4107E + 03$
	STD	$2.3047E + 03$	$1.3121E + 03$	$1.3167E + 03$	$1.2491E + 03$	$1.2116E + 03$	$1.1790E + 03$	$3.4607E + 03$
	Rank	1	4	3	2	5	6	7
	p value		$5.3070E - 05$	$2.6134E - 04$	$4.3896E - 03$	$5.7924E - 05$	$2.5967E - 05$	$7.6909E - 06$
F10	AVG	$5.4854E + 03$	$6.6088E + 03$	$6.9340E + 03$	$6.5450E + 03$	$7.8922E + 03$	$7.4870E + 03$	$6.7032E + 03$
	STD	$4.6850E + 02$	$7.0586E + 02$	$8.7016E + 02$	$9.6760E + 02$	$4.8577E + 02$	$6.6709E + 02$	$7.1353E + 02$
	Rank	1	3	5	2	7	6	4
	p value		$3.5152E - 06$	$3.8822E - 06$	$5.7924E - 05$	$1.7344E - 06$	$1.7344E - 06$	$3.5152E - 06$
F11	AVG	$1.3061E + 03$	$2.7691E + 03$	$3.5652E + 03$	$2.6648E + 03$	$2.2559E + 03$	$4.2405E + 03$	$4.6712E + 03$
	STD	$5.8914E + 01$	$8.1162E + 02$	$8.0204E + 02$	$7.1733E + 02$	$4.2647E + 02$	$1.5082E + 03$	$2.1153E + 03$
	Rank	1	4	5	3	2	6	7
	p value		$1.7344E - 06$	$1.7344E - 06$	$1.7344E - 06$	$1.7344E - 06$	$1.7344E - 06$	$1.7344E - 06$
F12	AVG	$2.4360E + 06$	$9.8130E + 08$	$8.2218E + 08$	$1.3739E + 08$	$7.9127E + 07$	$3.2303E + 09$	$3.1765E + 08$
	STD	$1.5471E + 06$	$1.1552E + 09$	$5.5155E + 08$	$1.0049E + 08$	$4.7219E + 07$	$2.2913E + 09$	$6.8408E + 08$
	Rank	1	6	5	3	2	7	4
	p value		$1.7344E - 06$	$1.7344E - 06$	$1.7344E - 06$	$1.7344E - 06$	$1.7344E - 06$	$1.7344E - 06$
F13	AVG	$2.8953E + 04$	$9.1760E + 07$	$1.0060E + 08$	$7.6109E + 05$	$1.1932E + 06$	$4.4095E + 08$	$2.3929E + 07$
	STD	$2.2290E + 04$	$2.5341E + 08$	$1.2133E + 08$	$5.3474E + 05$	$1.1894E + 06$	$8.1558E + 08$	$6.7495E + 07$
	Rank	1	5	6	2	3	7	4
	p value		$1.7344E - 06$	$1.7344E - 06$	$1.7344E - 06$	$1.7344E - 06$	$1.7344E - 06$	$1.7344E - 06$
F14	AVG	$5.6939E + 04$	$1.4304E + 06$	$1.2065E + 06$	$1.8174E + 06$	$9.9752E + 05$	$8.4350E + 05$	$1.6400E + 06$
	STD	$4.2722E + 04$	$8.4116E + 05$	$9.2598E + 05$	$1.8577E + 06$	$1.2010E + 06$	$6.5140E + 05$	$2.1374E + 06$
	Rank	1	5	4	7	3	2	6
	p value		$1.7344E - 06$	$1.9209E - 06$	$1.7344E - 06$	$8.4661E - 06$	$2.6033E - 06$	$8.4661E - 06$

Table 4: Continued.

		MEWOA	OBWOA	ACWOA	BWOA	BMWOA	CCMWOA	CWOA
F15	AVG	$1.4040E+04$	$2.2774E+06$	$1.5036E+07$	$4.6385E+05$	$4.0735E+05$	$1.5924E+07$	$1.1770E+07$
	STD	$1.3322E+04$	$3.0346E+06$	$2.0563E+07$	$7.6165E+05$	$4.8751E+05$	$3.3323E+07$	$2.3834E+07$
	Rank	1	4	6	3	2	7	5
	p value		$1.7344E-06$	$1.7344E-06$	$1.7344E-06$	$1.9209E-06$	$1.7344E-06$	$1.7344E-06$
F16	AVG	$2.8685E+03$	$4.1845E+03$	$3.9644E+03$	$4.1107E+03$	$3.6995E+03$	$4.2443E+03$	$4.0025E+03$
	STD	$3.6172E+02$	$6.1591E+02$	$3.8061E+02$	$5.2914E+02$	$4.2616E+02$	$6.7556E+02$	$5.5613E+02$
	Rank	1	6	3	5	2	7	4
	p value		$1.9209E-06$	$1.7344E-06$	$1.7344E-06$	$3.8822E-06$	$1.7344E-06$	$3.5152E-06$
F17	AVG	$2.2854E+03$	$2.7068E+03$	$2.6770E+03$	$2.6352E+03$	$2.5517E+03$	$2.8414E+03$	$2.6316E+03$
	STD	$1.9620E+02$	$4.3177E+02$	$2.5201E+02$	$2.6185E+02$	$2.4464E+02$	$4.2162E+02$	$3.4749E+02$
	Rank	1	6	5	4	2	7	3
	p value		$1.9729E-05$	$2.1630E-05$	$3.5152E-06$	$2.8308E-04$	$5.2165E-06$	$1.4773E-04$
F18	AVG	$5.5120E+05$	$2.8676E+06$	$5.4427E+06$	$6.4180E+06$	$5.3972E+06$	$1.2420E+07$	$6.6179E+06$
	STD	$4.8939E+05$	$3.0952E+06$	$5.3048E+06$	$7.5511E+06$	$5.4387E+06$	$9.8233E+06$	$5.5669E+06$
	Rank	1	2	4	5	3	7	6
	p value		$5.3070E-05$	$5.7517E-06$	$1.9209E-06$	$5.2165E-06$	$3.1817E-06$	$9.3157E-06$
F19	AVG	$1.3717E+04$	$3.0480E+06$	$1.0422E+07$	$4.6951E+06$	$2.0680E+06$	$1.0663E+07$	$1.2514E+07$
	STD	$1.1887E+04$	$2.2545E+06$	$9.7587E+06$	$3.9463E+06$	$2.4791E+06$	$1.4257E+07$	$2.9116E+07$
	Rank	1	3	5	4	2	6	7
	p value		$1.7344E-06$	$1.7344E-06$	$1.7344E-06$	$1.7344E-06$	$1.7344E-06$	$1.7344E-06$
F20	AVG	$2.5860E+03$	$2.7810E+03$	$2.7721E+03$	$2.7280E+03$	$2.7335E+03$	$2.7675E+03$	$2.8115E+03$
	STD	$2.4998E+02$	$1.8726E+02$	$1.4354E+02$	$1.7856E+02$	$1.8055E+02$	$1.4773E+02$	$2.8444E+02$
	Rank	1	6	5	2	3	4	7
	p value		$4.6818E-03$	$3.1618E-03$	$3.6826E-02$	$1.8519E-02$	$7.7309E-03$	$1.5927E-03$
F21	AVG	$2.4913E+03$	$2.6218E+03$	$2.5934E+03$	$2.6143E+03$	$2.5482E+03$	$2.6334E+03$	$2.6339E+03$
	STD	$5.3196E+01$	$4.0524E+01$	$3.9408E+01$	$5.7246E+01$	$4.3122E+01$	$4.5956E+01$	$4.5301E+01$
	Rank	1	5	3	4	2	6	7
	p value		$2.3534E-06$	$2.8786E-06$	$6.9838E-06$	$4.1955E-04$	$2.1266E-06$	$3.5152E-06$
F22	AVG	$6.7754E+03$	$7.4885E+03$	$5.7450E+03$	$6.0676E+03$	$5.7389E+03$	$8.0936E+03$	$7.6980E+03$
	STD	$8.1126E+02$	$1.6154E+03$	$2.0982E+03$	$2.7007E+03$	$3.1010E+03$	$1.1558E+03$	$1.4657E+03$
	Rank	4	5	2	3	1	7	6
	p value		$9.8421E-03$	$3.3269E-02$	$2.4519E-01$	$2.4308E-02$	$9.7110E-05$	$4.8969E-04$
F23	AVG	$2.8657E+03$	$3.0749E+03$	$3.0869E+03$	$3.1063E+03$	$2.9653E+03$	$3.2383E+03$	$3.1038E+03$
	STD	$5.7887E+01$	$9.9219E+01$	$1.0268E+02$	$9.7098E+01$	$8.3624E+01$	$1.3477E+02$	$8.9816E+01$
	Rank	1	3	4	6	2	7	5
	p value		$1.7344E-06$	$1.7344E-06$	$1.9209E-06$	$1.6394E-05$	$1.7344E-06$	$1.7344E-06$
F24	AVG	$3.0070E+03$	$3.2234E+03$	$3.2273E+03$	$3.1919E+03$	$3.1389E+03$	$3.3596E+03$	$3.2316E+03$
	STD	$5.7504E+01$	$1.0143E+02$	$5.8657E+01$	$9.1384E+01$	$1.0181E+02$	$1.1491E+02$	$1.0423E+02$
	Rank	1	4	5	3	2	7	6
	p value		$2.8786E-06$	$1.7344E-06$	$3.1817E-06$	$2.1630E-05$	$1.7344E-06$	$2.1266E-06$
F25	AVG	$2.9117E+03$	$3.1983E+03$	$3.2366E+03$	$3.0750E+03$	$3.0831E+03$	$3.5568E+03$	$3.1342E+03$
	STD	$1.9595E+01$	$1.2767E+02$	$1.1942E+02$	$5.0411E+01$	$4.1369E+01$	$1.6227E+02$	$1.2156E+02$
	Rank	1	5	6	2	3	7	4
	p value		$1.7344E-06$	$1.7344E-06$	$1.7344E-06$	$1.7344E-06$	$1.7344E-06$	$1.7344E-06$
F26	AVG	$5.8306E+03$	$8.1949E+03$	$7.7996E+03$	$8.2172E+03$	$7.2992E+03$	$9.0800E+03$	$8.1757E+03$
	STD	$6.3000E+02$	$1.2501E+03$	$9.6542E+02$	$1.4063E+03$	$1.4449E+03$	$1.1041E+03$	$7.9669E+02$
	Rank	1	5	3	6	2	7	4
	p value		$5.2165E-06$	$2.3534E-06$	$7.6909E-06$	$4.0715E-05$	$1.9209E-06$	$1.7344E-06$
F27	AVG	$3.4622E+03$	$3.4347E+03$	$3.5255E+03$	$3.4216E+03$	$3.3516E+03$	$3.6760E+03$	$3.4140E+03$
	STD	$1.5188E+02$	$1.3233E+02$	$1.2672E+02$	$1.2677E+02$	$8.4571E+01$	$1.5086E+02$	$1.7922E+02$
	Rank	5	4	6	3	1	7	2
	p value		$3.7094E-01$	$1.3591E-01$	$3.7094E-01$	$2.2551E-03$	$2.3704E-05$	$1.4704E-01$
F28	AVG	$8.3338E+03$	$3.9002E+03$	$3.9416E+03$	$3.4953E+03$	$3.4937E+03$	$4.9119E+03$	$3.6342E+03$
	STD	$1.2992E+03$	$2.8345E+02$	$3.0133E+02$	$9.2327E+01$	$7.6587E+01$	$3.5365E+02$	$2.4510E+02$
	Rank	7	4	5	2	1	6	3
	p value		$1.7344E-06$	$1.7344E-06$	$1.7344E-06$	$1.7344E-06$	$1.7344E-06$	$1.7344E-06$
F29	AVG	$4.1437E+03$	$4.9914E+03$	$4.9150E+03$	$5.3323E+03$	$4.8399E+03$	$5.4105E+03$	$4.9190E+03$
	STD	$3.1912E+02$	$3.7880E+02$	$4.6601E+02$	$4.9795E+02$	$2.8342E+02$	$5.9734E+02$	$3.4227E+02$
	Rank	1	5	3	6	2	7	4
	p value		$1.7344E-06$	$6.3391E-06$	$1.7344E-06$	$1.9209E-06$	$2.3534E-06$	$1.7344E-06$

TABLE 4: Continued.

		MEWOA	OBWOA	ACWOA	BWOA	BMWOA	CCMWOA	CWOA
F30	AVG	$3.6123E+04$	$6.5293E+07$	$7.3992E+07$	$2.4908E+07$	$8.6846E+06$	$1.3551E+08$	$2.0455E+07$
	STD	$2.6425E+04$	$1.6904E+08$	$4.6210E+07$	$2.2064E+07$	$5.5000E+06$	$1.2208E+08$	$1.5758E+07$
	Rank	1	5	6	4	2	7	3
	p value		$1.7344E-06$	$1.7344E-06$	$1.7344E-06$	$1.7344E-06$	$1.7344E-06$	$1.7344E-06$

the test functions with the aim of making them more diverse. We used a total of 27 functions for testing, where F1–F8 denote Unimodal functions, F8–F13 are Multimodal functions, F14–F19 are Hybrid functions, and F20–F27 are Composition functions. The specific experimental results are shown in Table 6, where the significance of the indicators that appear is explained in the previous section. In addition, we have chosen two functions in each class as examples and depicted the convergence curves of each algorithm on the corresponding functions.

Both Unimodal and Multimodal functions, F1–F13, are taken from the benchmark functions, while F14–F27 are taken from the CEC2014 test set. The entire performance of the MEWOA can be ranked in the middle position among all algorithms in terms of Unimodal and Multimodal functions. The overall performance of MEWOA is quite good due to the presence of algorithms like HCLPSO, LSHADE, and other algorithms with extremely strong performance inside the algorithms involved in the comparison. From the convergence curves in Figure 7, we can also find that the MEWOA works very well on F1, F2, F11, and F12, in terms of both convergence speed and convergence accuracy, especially for F11, where MEWOA can reach the optimal convergence accuracy at one-third of the iterations, and this performance is also worthy of recognition.

As for the Hybrid functions and the Composition functions, MEWOA's effect is not very good, but in the two functions F21 and F23, its effect is still relatively good. We can see that on these two functions, MEWOA's ranking can be located in the middle and upper. And among some remaining functions, such as F16, F17, F19, F20, and F22, although the ranking of MEWOA is not satisfactory, the difference between them is minimal.

Owing to the strong optimization capability, the MEWOA can be applied to many other promising problems such as medical science [125, 126], financial risk prediction [19, 35], and video deblurring [127–129]. In addition, MEWOA can also be used for parameter tuning for the convolutional neural networks [127, 130–132]. Other potential applications include feature selection [133–136], parameter optimization of solar cell [137–141], social recommendation and QoS-aware service composition [142–144], brain function network decomposition and estimation [145, 146], image editing [147–149], image dehazing [130, 150–152], blockchain technology [153–155], prediction problems in the educational field [156–160], and computer vision [161–163], which are also interesting topics that are worthy of investigation in the near future.

4.7. Practical Constraint Modeling Problems.
In this part, we apply the improved algorithm MEWOA in this paper to

three engineering constraint problems to demonstrate the MEWOA algorithm's performance in the mathematical constraint modeling problems, including tension/compression spring, welding beam, and I-beam. The mathematical model's main target value is constructed through penalty functions [164] and automatically discards the infeasible solution through the heuristic algorithm. There is no need to carry out this solution's infeasibility and usually uses a recursive iteration way with each recursive call generating a new point before finding a feasible solution. So, the model constructed by penalty functions combined with the MEWOA algorithm is utilized to handle three mathematical modeling problems.

4.7.1. Tension-Compression String Design Problem.
The tension/compression spring design aims to obtain the spring's minimum weight [165–167]. The model needs to iterate through the MEWOA algorithm to optimize the three design variables, including wire diameter (d), the average coil diameter (D), and the quantity of active coils (N). The mathematical model formula is illustrated as follows:

Consider $\vec{x} = [x_1 \ x_2 \ x_3] = [d \ D \ N]$.
Objective function:

$$f(\vec{x})_{\min} = x_1^2 x_2 x_3 + 2x_1^2 x_2 \quad (13)$$

subject to

$$h_1(\vec{x}) = 1 - \frac{x_2^3 x_3}{71785 x_1^4} \le 0,$$

$$h_2(\vec{x}) = \frac{4x_2^2 - x_1 x_2}{12566(x_2 x_1^3 - x_1^4)} + \frac{1}{5180 x_1^2} \le 0,$$

$$h_3(\vec{x}) = 1 - \frac{140.45 x_1}{x_2^3 x_3} \le 0,$$

$$h_4(\vec{x}) = \frac{x_1 + x_2}{1.5} - 1 \le 0.$$

(14)

Variable ranges:

$$0.05 \le x_1 \le 2.00,$$
$$0.25 \le x_2 \le 1.30, \quad (15)$$
$$2.00 \le x_3 \le 15.0.$$

Some scholars used mathematical techniques or metaheuristic techniques to solve the model. He and Wang [168] used PSO to handle tension/compression spring design problems. Coello Coello [169] utilized genetic algorithms to settle the problem, and the final minimum weight is
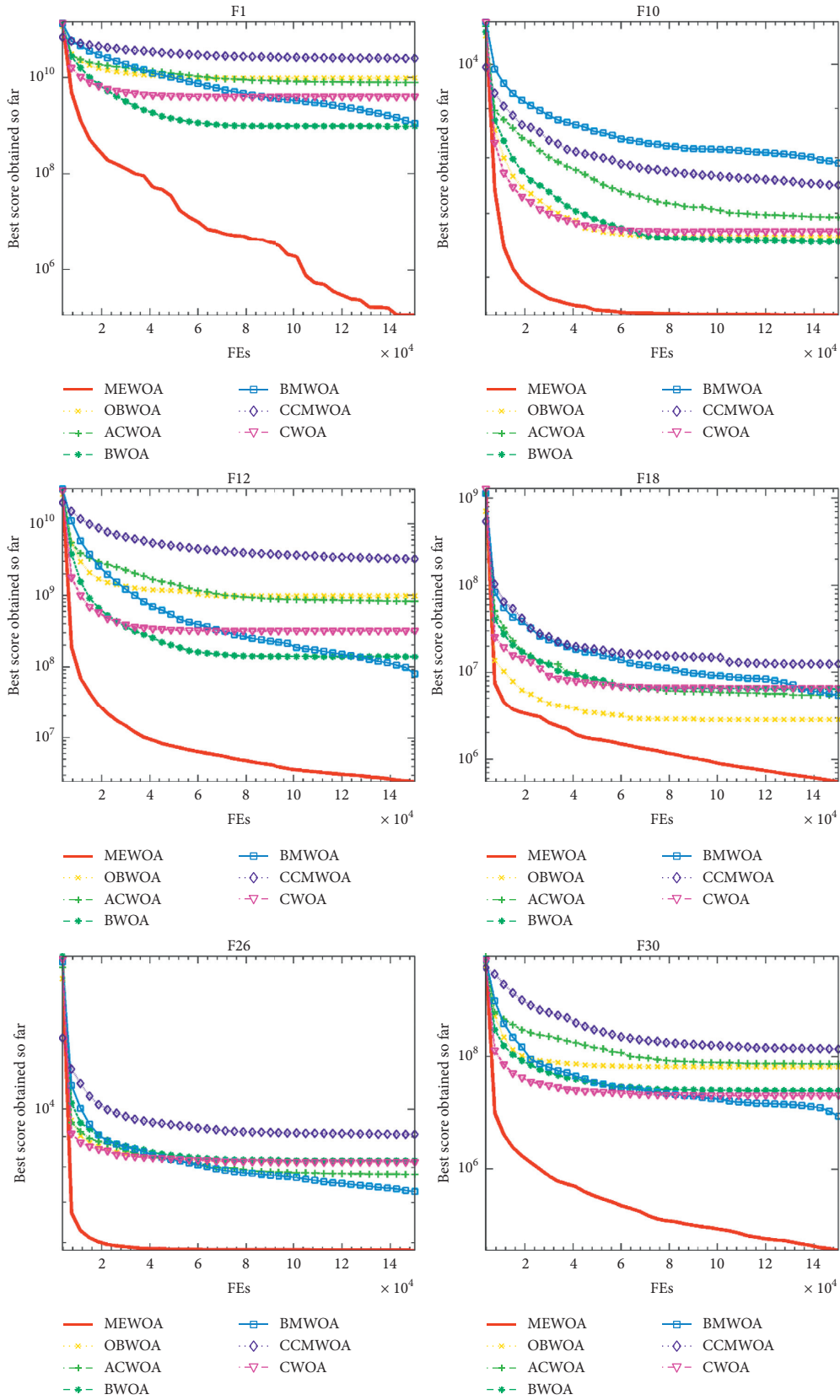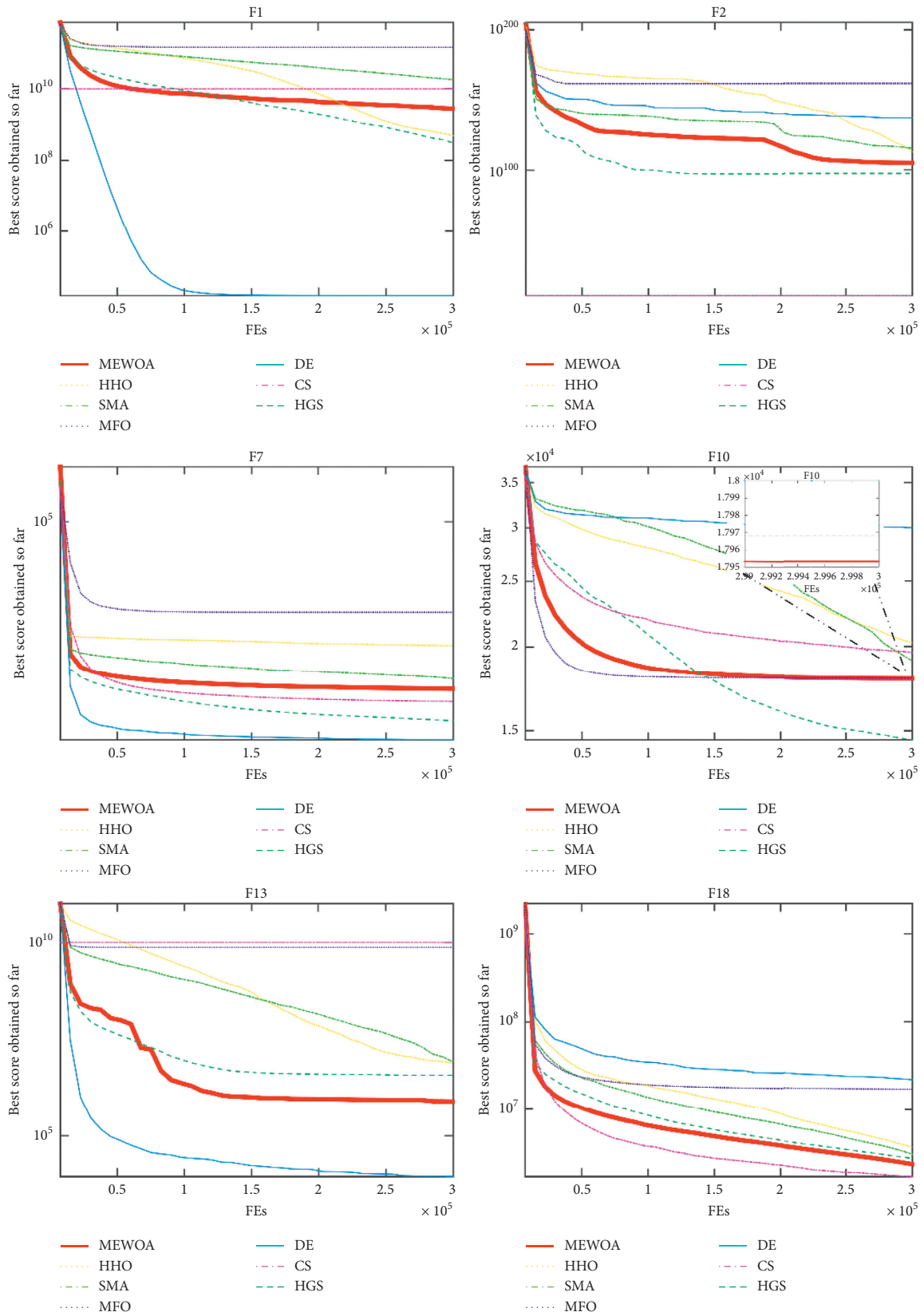
FIGURE 5: Convergence trends of MEWOA and peers.

Table 5: Comparison results of MEWOA with metaheuristic algorithms.

		MEWOA	HHO	SMA	HGS	DE	MFO	CS
F1	AVG	$2.7888E+09$	$4.9840E+08$	$1.8342E+10$	$3.1101E+08$	$1.5828E+04$	$1.4697E+11$	$1.0000E+10$
	STD	$4.1112E+09$	$5.5567E+07$	$4.2222E+09$	$4.1515E+08$	$1.8311E+04$	$5.4889E+10$	$0.0000E+00$
	Rank	4	3	6	2	1	7	5
	p value		$1.5169E-03$	$2.3518E-05$	$2.5504E-04$	$1.8215E-05$	$1.8215E-05$	$5.6117E-05$
F2	AVG	$1.0811E+105$	$4.9880E+112$	$1.9634E+115$	$2.3856E+97$	$1.4657E+137$	$6.2116E+161$	$1.0000E+10$
	STD	$5.2928E+105$	$2.4436E+113$	$6.8005E+115$	$1.1687E+98$	$2.7004E+137$	$6.5535E+04$	$0.0000E+00$
	Rank	3	4	5	2	6	7	1
	p value		$1.5158E-02$	$2.3518E-05$	$8.5744E-03$	$1.8215E-05$	$1.8215E-05$	$1.8215E-05$
F3	AVG	$2.0518E+05$	$2.2082E+05$	$2.0278E+05$	$1.2290E+05$	$6.1128E+05$	$6.7633E+05$	$5.1454E+05$
	STD	$1.8131E+04$	$1.6309E+04$	$1.6408E+04$	$3.6076E+04$	$5.6384E+04$	$2.1096E+05$	$4.7395E+04$
	Rank	3	4	2	1	6	7	5
	p value		$8.5744E-03$	$3.9137E-01$	$1.8215E-05$	$1.8215E-05$	$1.8215E-05$	$1.8215E-05$
F4	AVG	$1.1492E+03$	$1.0209E+03$	$1.8776E+03$	$7.7633E+02$	$6.2027E+02$	$3.1304E+04$	$6.8021E+02$
	STD	$2.7710E+02$	$7.0247E+01$	$3.1601E+02$	$1.1704E+02$	$1.2220E+01$	$1.9668E+04$	$6.2934E+01$
	Rank	5	4	6	3	1	7	2
	p value		$5.9333E-02$	$1.8215E-05$	$1.8215E-05$	$1.8215E-05$	$1.8215E-05$	$1.8215E-05$
F5	AVG	$1.5433E+03$	$1.5048E+03$	$1.3493E+03$	$1.2086E+03$	$1.4145E+03$	$1.8676E+03$	$1.3472E+03$
	STD	$1.4621E+02$	$4.5375E+01$	$4.1080E+01$	$8.6658E+01$	$2.5021E+01$	$1.6102E+02$	$5.4429E+01$
	Rank	6	5	3	1	4	7	2
	p value		$2.5310E-01$	$6.3342E-05$	$2.6691E-05$	$8.2921E-04$	$5.6117E-05$	$3.0270E-05$
F6	AVG	$6.7711E+02$	$6.8224E+02$	$6.6040E+02$	$6.3323E+02$	$6.0000E+02$	$6.7095E+02$	$6.7323E+02$
	STD	$1.1545E+01$	$4.4768E+00$	$4.3507E+00$	$5.6014E+00$	$2.3705E-13$	$4.6354E+00$	$8.7010E+00$
	Rank	6	7	3	2	1	4	5
	p value		$2.7807E-02$	$3.4301E-05$	$1.8215E-05$	$1.8215E-05$	$3.4491E-02$	$1.5313E-01$
F7	AVG	$2.6149E+03$	$3.7113E+03$	$2.8342E+03$	$2.0231E+03$	$1.7360E+03$	$4.8578E+03$	$2.3608E+03$
	STD	$4.0557E+02$	$1.3218E+02$	$1.1746E+02$	$1.8844E+02$	$2.6302E+01$	$9.6042E+02$	$1.0809E+02$
	Rank	4	6	5	2	1	7	3
	p value		$2.0706E-05$	$1.1927E-02$	$7.1443E-05$	$1.8215E-05$	$1.8215E-05$	$6.0907E-03$
F8	AVG	$1.8381E+03$	$1.9423E+03$	$1.7220E+03$	$1.5410E+03$	$1.6970E+03$	$2.1830E+03$	$1.6931E+03$
	STD	$1.5719E+02$	$7.7800E+01$	$8.3696E+01$	$9.5254E+01$	$2.2908E+01$	$1.6552E+02$	$6.3349E+01$
	Rank	5	6	4	1	3	7	2
	p value		$7.8806E-03$	$1.0172E-03$	$3.0270E-05$	$4.9082E-04$	$2.3518E-05$	$2.0378E-04$
F9	AVG	$4.0928E+04$	$4.8779E+04$	$3.3534E+04$	$2.4577E+04$	$1.4344E+03$	$4.4792E+04$	$5.1247E+04$
	STD	$1.0060E+04$	$4.7643E+03$	$3.7290E+03$	$3.1871E+03$	$1.9961E+02$	$6.6036E+03$	$8.9405E+03$
	Rank	4	6	3	2	1	5	7
	p value		$1.6731E-03$	$4.2747E-03$	$3.0270E-05$	$1.8215E-05$	$7.1861E-02$	$3.9582E-04$
F10	AVG	$1.7953E+04$	$2.0257E+04$	$1.9024E+04$	$1.4537E+04$	$2.9970E+04$	$1.7968E+04$	$1.9589E+04$
	STD	$1.6953E+03$	$1.0935E+03$	$1.4198E+03$	$1.4226E+03$	$6.0852E+02$	$1.3604E+03$	$4.2207E+02$
	Rank	2	6	4	1	7	3	5
	p value		$1.8194E-04$	$4.8675E-02$	$4.9677E-05$	$1.8215E-05$	$9.7721E-01$	$3.9582E-04$
F11	AVG	$1.1146E+04$	$6.6177E+03$	$1.3000E+04$	$4.0275E+03$	$8.0747E+03$	$1.6383E+05$	$4.2994E+03$
	STD	$5.1184E+03$	$1.2893E+03$	$4.6483E+03$	$2.9372E+03$	$1.6194E+03$	$1.0082E+05$	$6.9278E+02$
	Rank	5	3	6	1	4	7	2
	p value		$1.5169E-03$	$1.0340E-01$	$1.0203E-04$	$2.3999E-02$	$2.0706E-05$	$3.4301E-05$
F12	AVG	$3.0433E+08$	$5.0870E+08$	$1.1246E+09$	$1.8517E+08$	$2.4746E+08$	$3.6693E+10$	$1.0000E+10$
	STD	$4.7772E+08$	$1.6876E+08$	$4.3599E+08$	$1.4342E+08$	$3.9693E+07$	$1.4776E+10$	$0.0000E+00$
	Rank	3	4	5	1	2	7	6
	p value		$1.9137E-02$	$5.6117E-05$	$7.7510E-01$	$1.0340E-01$	$1.8215E-05$	$1.8215E-05$
F13	AVG	$8.0205E+05$	$7.6973E+06$	$8.3991E+06$	$3.7945E+06$	$8.9851E+03$	$7.4539E+09$	$1.0000E+10$
	STD	$2.0468E+06$	$1.5882E+06$	$2.6856E+07$	$1.2600E+07$	$1.2759E+04$	$5.9644E+09$	$0.0000E+00$
	Rank	2	4	5	3	1	6	7
	p value		$2.0706E-05$	$4.9082E-04$	$2.3014E-01$	$1.8215E-05$	$1.8215E-05$	$1.8215E-05$
F14	AVG	$1.6213E+06$	$2.2404E+06$	$2.1552E+06$	$8.1350E+05$	$1.1498E+07$	$1.0914E+07$	$3.3779E+05$
	STD	$1.1996E+06$	$6.8718E+05$	$1.2730E+06$	$3.6761E+05$	$2.9606E+06$	$1.4342E+07$	$1.4734E+05$
	Rank	3	5	4	2	7	6	1
	p value		$1.0995E-02$	$9.7491E-02$	$4.9082E-04$	$1.8215E-05$	$3.2520E-03$	$1.8215E-05$
F15	AVG	$1.0476E+05$	$2.0463E+06$	$5.4296E+04$	$9.2208E+04$	$2.6462E+04$	$1.7237E+09$	$1.0000E+10$
	STD	$2.3658E+05$	$5.6835E+05$	$9.1684E+04$	$1.7587E+05$	$2.9456E+04$	$2.1518E+09$	$0.0000E+00$
	Rank	4	5	2	3	1	6	7
	p value		$1.8215E-05$	$1.6151E-01$	$3.6057E-01$	$5.2963E-01$	$4.9677E-05$	$1.8215E-05$

TABLE 5: Continued.

|		MEWOA	HHO	SMA	HGS	DE	MFO	CS
F16	AVG	$6.5007E + 03$	$7.6919E + 03$	$6.4449E + 03$	$6.7451E + 03$	$8.9299E + 03$	$8.3383E + 03$	$6.5108E + 03$
	STD	$6.6524E + 02$	$5.4911E + 02$	$9.0734E + 02$	$7.1938E + 02$	$3.9103E + 02$	$6.5950E + 02$	$2.7308E + 02$
	Rank	2	5	1	4	7	6	3
	p value		$4.9677E - 05$	$7.9707E - 01$	$2.1923E - 01$	$1.8215E - 05$	$1.8215E - 05$	$8.4148E - 01$
F17	AVG	$6.3650E + 03$	$6.4839E + 03$	$5.2020E + 03$	$5.4345E + 03$	$5.4888E + 03$	$2.9574E + 04$	$5.0701E + 03$
	STD	$6.0952E + 02$	$5.4838E + 02$	$5.7154E + 02$	$3.8989E + 02$	$2.3292E + 02$	$7.7040E + 04$	$2.3818E + 02$
	Rank	5	6	2	3	4	7	1
	p value		$7.1032E - 01$	$3.8838E - 05$	$1.0203E - 04$	$8.0517E - 05$	$1.8215E - 05$	$2.6691E - 05$
F18	AVG	$2.3586E + 06$	$3.6828E + 06$	$3.0654E + 06$	$2.7563E + 06$	$2.1707E + 07$	$1.6840E + 07$	$1.7082E + 06$
	STD	$1.3657E + 06$	$1.6591E + 06$	$1.8227E + 06$	$1.8969E + 06$	$6.1519E + 06$	$2.5829E + 07$	$4.1136E + 05$
	Rank	2	5	4	3	7	6	1
	p value		$4.6756E - 03$	$2.6516E - 01$	$5.2963E - 01$	$1.8215E - 05$	$2.2346E - 03$	$6.3291E - 02$
F19	AVG	$2.2811E + 04$	$9.2444E + 06$	$4.1479E + 05$	$8.0893E + 04$	$1.9794E + 04$	$1.3273E + 09$	$1.0000E + 10$
	STD	$1.4499E + 04$	$5.1528E + 06$	$3.7123E + 05$	$6.2020E + 04$	$2.2278E + 04$	$1.4732E + 09$	$0.0000E + 00$
	Rank	2	5	4	3	1	6	7
	p value		$1.8215E - 05$	$1.8215E - 05$	$7.1443E - 05$	$6.3291E - 02$	$1.8215E - 05$	$1.8215E - 05$
F20	AVG	$6.2485E + 03$	$5.7908E + 03$	$5.0367E + 03$	$5.4356E + 03$	$5.7274E + 03$	$5.9532E + 03$	$5.6192E + 03$
	STD	$6.1430E + 02$	$4.9167E + 02$	$4.5369E + 02$	$5.5928E + 02$	$2.2179E + 02$	$6.5073E + 02$	$2.4746E + 02$
	Rank	7	5	1	2	4	6	3
	p value		$1.5158E - 02$	$2.3518E - 05$	$3.1822E - 04$	$2.9642E - 03$	$8.6476E - 02$	$5.4594E - 04$
F21	AVG	$3.4080E + 03$	$4.0621E + 03$	$3.1835E + 03$	$2.9952E + 03$	$3.2438E + 03$	$3.7236E + 03$	$3.1724E + 03$
	STD	$1.9244E + 02$	$1.6810E + 02$	$1.1195E + 02$	$8.2857E + 01$	$3.0492E + 01$	$2.1205E + 02$	$9.9310E + 01$
	Rank	5	7	3	1	4	6	2
	p value		$1.8215E - 05$	$6.0677E - 04$	$1.8215E - 05$	$1.5169E - 03$	$2.0706E - 05$	$9.0672E - 05$
F22	AVG	$1.9262E + 04$	$2.4028E + 04$	$2.1385E + 04$	$1.7506E + 04$	$3.1763E + 04$	$2.0519E + 04$	$2.2755E + 04$
	STD	$1.5257E + 03$	$1.3118E + 03$	$1.1967E + 03$	$1.0533E + 03$	$6.0097E + 02$	$1.8378E + 03$	$5.9742E + 02$
	Rank	2	6	4	1	7	3	5
	p value		$1.8215E - 05$	$1.1472E - 04$	$1.4470E - 04$	$1.8215E - 05$	$8.5744E - 03$	$1.8215E - 05$
F23	AVG	$3.9003E + 03$	$5.1643E + 03$	$3.6747E + 03$	$3.2529E + 03$	$3.5529E + 03$	$3.9352E + 03$	$3.6545E + 03$
	STD	$1.6807E + 02$	$2.7838E + 02$	$7.4514E + 01$	$5.5872E + 01$	$2.1217E + 01$	$1.5414E + 02$	$8.7300E + 01$
	Rank	5	7	4	1	2	6	3
	p value		$1.8215E - 05$	$5.6117E - 05$	$1.8215E - 05$	$1.8215E - 05$	$3.6057E - 01$	$2.6691E - 05$
F24	AVG	$4.6479E + 03$	$6.5004E + 03$	$4.3113E + 03$	$3.9218E + 03$	$4.1047E + 03$	$4.4701E + 03$	$4.2583E + 03$
	STD	$2.1942E + 02$	$3.8952E + 02$	$1.0737E + 02$	$9.5224E + 01$	$2.4785E + 01$	$1.7258E + 02$	$9.9907E + 01$
	Rank	6	7	4	1	2	5	3
	p value		$1.8215E - 05$	$4.3941E - 05$	$1.8215E - 05$	$1.8215E - 05$	$5.5811E - 03$	$2.0706E - 05$
F25	AVG	$3.9507E + 03$	$3.7214E + 03$	$4.2569E + 03$	$3.6542E + 03$	$3.2693E + 03$	$1.2101E + 04$	$3.3212E + 03$
	STD	$2.8356E + 02$	$6.7331E + 01$	$1.7083E + 02$	$3.7974E + 02$	$5.7511E + 01$	$5.2221E + 03$	$4.3663E + 01$
	Rank	5	4	6	3	1	7	2
	p value		$2.8499E - 04$	$6.7386E - 04$	$1.7719E - 02$	$1.8215E - 05$	$1.8215E - 05$	$1.8215E - 05$
F26	AVG	$1.8804E + 04$	$2.6052E + 04$	$1.8102E + 04$	$1.2630E + 04$	$1.4720E + 04$	$1.9820E + 04$	$1.6418E + 04$
	STD	$2.2676E + 03$	$1.6397E + 03$	$3.2370E + 03$	$2.6531E + 03$	$2.3288E + 02$	$1.5918E + 03$	$1.1740E + 03$
	Rank	5	7	4	1	2	6	3
	p value		$1.8215E - 05$	$6.6824E - 01$	$1.8215E - 05$	$1.8215E - 05$	$1.3735E - 01$	$3.9582E - 04$
F27	AVG	$8.3736E + 03$	$4.4735E + 03$	$3.6246E + 03$	$3.5247E + 03$	$3.5497E + 03$	$4.0464E + 03$	$3.7779E + 03$
	STD	$1.7236E + 03$	$3.2426E + 02$	$8.3281E + 01$	$7.9600E + 01$	$6.2216E + 01$	$2.3018E + 02$	$8.0163E + 01$
	Rank	7	6	3	1	2	5	4
	p value		$2.0706E - 05$	$1.8215E - 05$	$1.8215E - 05$	$1.8215E - 05$	$1.8215E - 05$	$1.8215E - 05$
F28	AVG	$5.4475E + 04$	$3.7262E + 03$	$4.1512E + 03$	$3.4833E + 03$	$3.3953E + 03$	$2.0538E + 04$	$3.4414E + 03$
	STD	$5.9341E + 03$	$4.8190E + 01$	$2.4287E + 02$	$4.2503E + 01$	$1.8255E + 02$	$1.8753E + 03$	$3.1260E + 01$
	Rank	7	4	5	3	1	6	2
	p value		$1.8215E - 05$	$1.8215E - 05$	$1.8215E - 05$	$1.8215E - 05$	$1.8215E - 05$	$1.8215E - 05$
F29	AVG	$8.3827E + 03$	$9.8509E + 03$	$8.6041E + 03$	$6.9585E + 03$	$7.4441E + 03$	$1.7671E + 04$	$7.7750E + 03$
	STD	$7.1162E + 02$	$8.7940E + 02$	$6.7211E + 02$	$4.3224E + 02$	$3.0162E + 02$	$1.5175E + 04$	$2.5110E + 02$
	Rank	4	6	5	1	2	7	3
	p value		$6.3342E - 05$	$1.7932E - 01$	$2.6691E - 05$	$2.8499E - 04$	$2.0706E - 05$	$1.3743E - 03$
F30	AVG	$2.4181E + 06$	$4.7921E + 07$	$1.6219E + 07$	$1.5200E + 06$	$2.2138E + 04$	$3.6915E + 09$	$1.0000E + 10$
	STD	$2.3647E + 06$	$1.6952E + 07$	$1.3407E + 07$	$2.2183E + 06$	$7.6087E + 03$	$2.8610E + 09$	$0.0000E + 00$
	Rank	3	5	4	2	1	6	7
	p value		$1.8215E - 05$	$2.6691E - 05$	$1.5313E - 01$	$1.8215E - 05$	$1.8215E - 05$	$1.8215E - 05$

Figure 6: Continued.
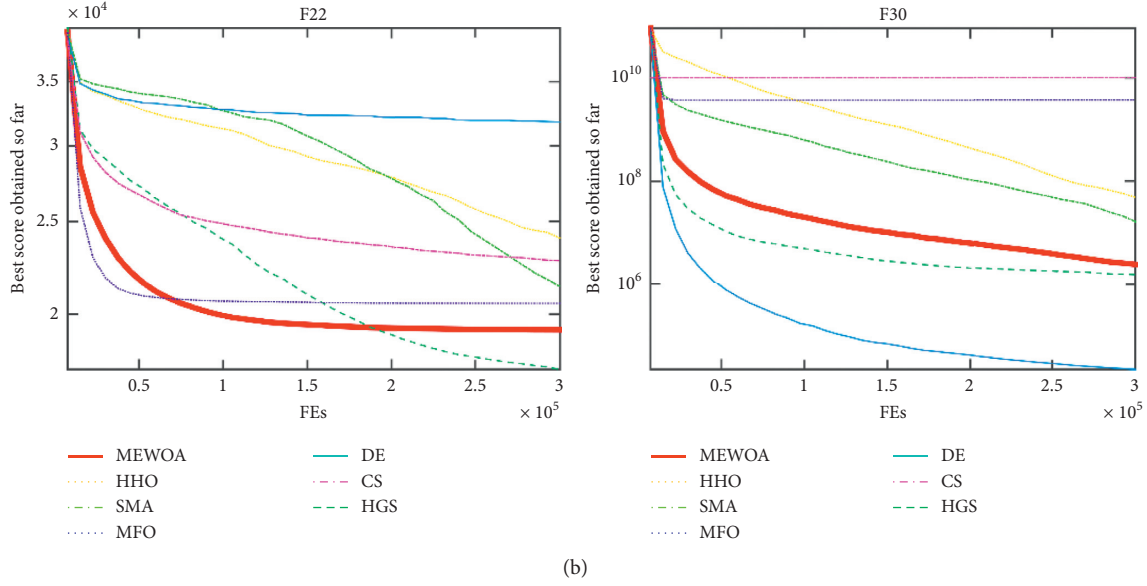
Figure 6: Convergence trends of MEWOA and metaheuristic algorithms.

Table 6: Comparison results of MEWOA with advanced algorithms.

		MEWOA	HCLPSO	SADE	JADE	CLPSO	LSHADE	LSHADE_ES	MSCA
F1	AVG	$1.2569E-182$	$0.0000E+00$	$1.2584E-18$	$1.9473E-49$	$3.3945E-08$	$4.0764E-29$	$3.9402E-21$	$2.7595E-300$
	STD	$0.0000E+00$	$0.0000E+00$	$4.6982E-18$	$9.5398E-49$	$1.3608E-08$	$1.9695E-28$	$7.4330E-21$	$0.0000E+00$
	Rank	3	1	7	4	8	5	6	2
	p value		$1.8215E-05$	$1.8215E-05$	$1.8215E-05$	$1.8215E-05$	$1.8215E-05$	$1.8215E-05$	$1.8215E-05$
F2	AVG	$8.6406E-134$	$0.0000E+00$	$9.3447E-11$	$1.9157E-23$	$8.4210E-06$	$1.5492E-10$	$2.1801E-05$	$4.9151E-194$
	STD	$3.6770E-133$	$0.0000E+00$	$4.4857E-10$	$6.5627E-23$	$1.0438E-06$	$5.6184E-10$	$3.5553E-05$	$0.0000E+00$
	Rank	3	1	5	4	7	6	8	2
	p value		$1.8215E-05$	$1.8215E-05$	$1.8215E-05$	$1.8215E-05$	$1.8215E-05$	$1.8215E-05$	$1.8215E-05$
F3	AVG	$2.0105E+03$	$0.0000E+00$	$1.0304E+03$	$1.0487E-01$	$7.4220E+04$	$2.6868E-01$	$2.9066E-01$	$4.1699E-36$
	STD	$1.1603E+03$	$0.0000E+00$	$3.6045E+02$	$1.2912E-01$	$7.8998E+03$	$4.1952E-01$	$3.7604E-01$	$2.0425E-35$
	Rank	7	1	6	3	8	4	5	2
	p value		$1.8215E-05$	$2.2806E-04$	$1.8215E-05$	$1.8215E-05$	$1.8215E-05$	$1.8215E-05$	$1.8215E-05$
F4	AVG	$4.7158E+01$	$0.0000E+00$	$8.0223E+00$	$3.0423E+01$	$2.3227E+01$	$3.1500E+01$	$2.1085E+01$	$1.7669E-62$
	STD	$2.6553E+01$	$0.0000E+00$	$3.5809E+00$	$3.5006E+00$	$9.9945E-01$	$3.1446E+00$	$2.5381E+00$	$8.6554E-62$
	Rank	8	1	3	6	5	7	4	2
	p value		$1.8037E-05$	$1.8215E-05$	$3.2520E-03$	$5.6117E-05$	$7.8806E-03$	$3.0270E-05$	$1.8037E-05$
F5	AVG	$9.0878E+01$	$0.0000E+00$	$2.5044E+02$	$3.3751E+01$	$1.1780E+02$	$9.9309E+01$	$1.5236E+02$	$9.8122E+01$
	STD	$2.2799E+00$	$0.0000E+00$	$8.9147E+01$	$3.9626E+01$	$4.6422E+01$	$5.0781E+01$	$3.4750E+01$	$5.4494E-01$
	Rank	3	1	8	2	6	5	7	4
	p value		$1.8215E-05$	$1.8215E-05$	$1.2889E-04$	$2.5842E-02$	$9.3169E-01$	$2.6691E-05$	$2.0706E-05$
F6	AVG	$1.0455E+00$	$0.0000E+00$	$7.5009E-19$	$4.1215E-32$	$2.9895E-08$	$2.1326E-31$	$9.6013E-21$	$1.6562E+01$
	STD	$6.7610E-01$	$0.0000E+00$	$2.3381E-18$	$2.6953E-32$	$8.2736E-09$	$1.0715E-31$	$3.3317E-20$	$8.0242E-01$
	Rank	7	1	5	2	6	3	4	8
	p value		$1.8215E-05$	$1.8215E-05$	$1.8215E-05$	$1.8215E-05$	$1.8215E-05$	$1.8215E-05$	$1.8215E-05$
F7	AVG	$6.0591E-03$	$0.0000E+00$	$1.7219E-01$	$8.2773E-02$	$2.3969E-02$	$3.8799E-01$	$3.3155E-01$	$1.4537E-04$
	STD	$2.8014E-03$	$0.0000E+00$	$6.1625E-02$	$3.4827E-02$	$2.8555E-03$	$2.2665E-01$	$2.3386E-01$	$1.1529E-04$
	Rank	3	1	6	5	4	8	7	2
	p value		$1.8215E-05$	$1.8215E-05$	$1.8215E-05$	$1.8215E-05$	$1.8215E-05$	$1.8215E-05$	$1.8215E-05$
F8	AVG	$-1.8492E+04$	$0.0000E+00$	$-4.0880E+04$	$-4.0813E+04$	$-4.1834E+04$	$-6.1322E+03$	$-4.0250E+04$	$-1.9443E+04$
	STD	$2.1949E+02$	$0.0000E+00$	$3.2508E+02$	$3.7885E+02$	$6.9669E+01$	$4.2287E+02$	$8.6108E+02$	$2.6514E+03$
	Rank	6	8	2	3	1	7	4	5
	p value		$1.8215E-05$	$1.8215E-05$	$1.8215E-05$	$1.8215E-05$	$1.8215E-05$	$1.8215E-05$	$7.1861E-02$

Table 6: Continued.

		MEWOA	HCLPSO	SADE	JADE	CLPSO	LSHADE	LSHADE_ES	MSCA
F9	AVG	$5.9498E+02$	$0.0000E+00$	$3.1383E+01$	$7.4622E-01$	$4.2339E-02$	$1.3899E+03$	$8.8193E+00$	$0.0000E+00$
	STD	$1.2476E+02$	$0.0000E+00$	$5.8751E+00$	$2.0168E+00$	$2.0300E-01$	$8.4750E+02$	$5.3562E+00$	$0.0000E+00$
	Rank	7	1	6	4	3	8	5	1
	p value		$1.8215E-05$	$1.8215E-05$	$1.8215E-05$	$1.8215E-05$	$6.0677E-04$	$1.8215E-05$	$1.8215E-05$
F10	AVG	$1.8277E+01$	$0.0000E+00$	$4.8107E+00$	$3.3569E+00$	$5.6114E-05$	$1.8711E-13$	$1.0971E+01$	$5.9350E+00$
	STD	$5.6291E+00$	$0.0000E+00$	$7.7991E-01$	$8.0222E-01$	$8.7246E-06$	$1.3039E-14$	$9.7568E-01$	$9.4480E+00$
	Rank	8	1	5	4	3	2	7	6
	p value		$1.8215E-05$	$2.6691E-05$	$2.6691E-05$	$2.6691E-05$	$2.6691E-05$	$3.2520E-03$	$4.6756E-03$
F11	AVG	$0.0000E+00$	$0.0000E+00$	$1.1291E-01$	$2.5517E-02$	$9.3593E-08$	$5.1017E-02$	$8.2012E-03$	$0.0000E+00$
	STD	$0.0000E+00$	$0.0000E+00$	$1.4935E-01$	$4.9975E-02$	$4.6089E-08$	$7.0621E-02$	$1.1942E-02$	$0.0000E+00$
	Rank	1	1	8	6	4	7	5	1
	p value		$1.0000E+00$	$1.3101E-04$	$1.8215E-05$	$1.8215E-05$	$1.8215E-05$	$1.8215E-05$	$1.0000E+00$
F12	AVG	$4.9773E-01$	$0.0000E+00$	$1.4232E-01$	$8.1941E-01$	$4.1072E-10$	$1.4086E+00$	$1.8058E+00$	$5.9598E-01$
	STD	$8.5940E-01$	$0.0000E+00$	$2.2161E-01$	$9.3459E-01$	$1.3208E-10$	$1.4559E+00$	$2.2647E+00$	$8.9643E-02$
	Rank	4	1	3	6	2	7	8	5
	p value		$1.8215E-05$	$6.7464E-02$	$1.0960E-01$	$1.8215E-05$	$2.2346E-03$	$7.8806E-03$	$1.0340E-01$
F13	AVG	$2.0206E+00$	$0.0000E+00$	$5.1741E-01$	$4.0895E-01$	$3.2942E-08$	$3.8895E+00$	$6.7941E+01$	$8.4065E+00$
	STD	$2.2432E+00$	$0.0000E+00$	$1.0905E+00$	$1.0036E+00$	$9.5664E-09$	$4.7486E+00$	$3.3014E+01$	$2.3718E-01$
	Rank	5	1	4	3	2	6	8	7
	p value		$1.8215E-05$	$7.4779E-04$	$8.0517E-05$	$1.8215E-05$	$3.1731E-01$	$1.8215E-05$	$2.0706E-05$
F14	AVG	$8.6336E+06$	$0.0000E+00$	$1.3127E+06$	$1.0362E+05$	$3.5798E+07$	$1.3038E+05$	$1.5379E+05$	$4.8497E+07$
	STD	$6.1405E+06$	$0.0000E+00$	$4.4922E+05$	$8.5187E+04$	$7.8511E+06$	$7.2937E+04$	$8.8656E+04$	$3.2124E+07$
	Rank	6	1	5	2	7	3	4	8
	p value		$1.8215E-05$	$1.8215E-05$	$1.8215E-05$	$1.8215E-05$	$1.8215E-05$	$1.8215E-05$	$1.8215E-05$
F15	AVG	$1.5408E+07$	$0.0000E+00$	$2.6581E+03$	$4.5701E+03$	$5.0173E+03$	$4.5137E+03$	$6.2594E+03$	$2.6234E+09$
	STD	$4.5159E+07$	$0.0000E+00$	$6.3741E+02$	$2.1893E+03$	$2.1788E+03$	$2.0320E+03$	$4.1307E+03$	$1.3244E+09$
	Rank	7	1	2	4	5	3	6	8
	p value		$1.8215E-05$	$1.8215E-05$	$1.6232E-04$	$1.6232E-04$	$2.0378E-04$	$4.6756E-03$	$1.8215E-05$
F16	AVG	$2.0733E+03$	$0.0000E+00$	$1.9980E+03$	$1.9998E+03$	$2.0147E+03$	$2.0115E+03$	$2.0442E+03$	$2.4631E+03$
	STD	$2.8253E+01$	$0.0000E+00$	$3.2580E+01$	$2.2786E+01$	$1.3238E+01$	$2.4256E+01$	$2.7623E+01$	$1.1272E+02$
	Rank	7	1	2	3	5	4	6	8
	p value		$1.8215E-05$	$2.6691E-05$	$1.8215E-05$	$2.3518E-05$	$2.0706E-05$	$2.6998E-03$	$1.8215E-05$
F17	AVG	$4.7411E+04$	$0.0000E+00$	$3.4786E+04$	$1.4127E+04$	$3.8256E+04$	$1.0104E+04$	$3.1493E+03$	$7.7468E+04$
	STD	$1.2273E+04$	$0.0000E+00$	$1.1382E+04$	$1.8669E+04$	$6.6486E+03$	$9.5970E+03$	$2.2074E+02$	$1.7488E+04$
	Rank	7	1	5	4	6	3	2	8
	p value		$1.8215E-05$	$3.2520E-03$	$7.1443E-05$	$7.8806E-03$	$2.0706E-05$	$1.8215E-05$	$6.3342E-05$
F18	AVG	$4.5553E+06$	$0.0000E+00$	$1.4398E+06$	$4.5873E+04$	$1.7528E+07$	$5.7403E+04$	$4.5246E+04$	$2.5887E+07$
	STD	$2.4111E+06$	$0.0000E+00$	$4.6818E+05$	$3.7590E+04$	$4.8015E+06$	$3.2729E+04$	$2.4163E+04$	$1.2860E+07$
	Rank	6	1	5	3	7	4	2	8
	p value		$1.8215E-05$	$1.8215E-05$	$1.8215E-05$	$1.8215E-05$	$1.8215E-05$	$1.8215E-05$	$1.8215E-05$
F19	AVG	$5.4625E+03$	$0.0000E+00$	$3.9874E+03$	$4.1164E+03$	$3.9843E+03$	$4.0517E+03$	$3.8389E+03$	$4.8857E+03$
	STD	$6.7438E+02$	$0.0000E+00$	$3.7582E+02$	$3.2798E+02$	$2.9974E+02$	$2.8293E+02$	$4.0803E+02$	$4.9073E+02$
	Rank	8	1	4	6	3	5	2	7
	p value		$1.8215E-05$	$2.6691E-05$	$1.8215E-05$	$2.0706E-05$	$2.6691E-05$	$1.8215E-05$	$2.9642E-03$
F20	AVG	$2.6671E+03$	$0.0000E+00$	$2.6485E+03$	$2.6482E+03$	$2.6485E+03$	$2.6482E+03$	$2.6482E+03$	$3.2821E+03$
	STD	$1.2544E+01$	$0.0000E+00$	$1.9072E-01$	$8.3736E-11$	$1.8986E-01$	$1.6676E-05$	$3.4250E-03$	$1.2001E+02$
	Rank	7	1	5	2	6	3	4	8
	p value		$1.8215E-05$	$1.8215E-05$	$1.8215E-05$	$1.8215E-05$	$1.8215E-05$	$1.8215E-05$	$1.8215E-05$
F21	AVG	$2.7987E+03$	$0.0000E+00$	$2.8179E+03$	$2.8268E+03$	$2.7650E+03$	$2.8574E+03$	$2.8751E+03$	$2.6000E+03$
	STD	$1.9004E+01$	$0.0000E+00$	$9.4205E+00$	$9.7299E+00$	$2.8193E+00$	$1.2508E+01$	$1.9061E+01$	$8.1779E-04$
	Rank	4	1	5	6	3	7	8	2
	p value		$1.8215E-05$	$3.8838E-05$	$1.8215E-05$	$4.9677E-05$	$1.8215E-05$	$1.8215E-05$	$1.8215E-05$
F22	AVG	$2.8316E+03$	$0.0000E+00$	$2.7645E+03$	$2.7995E+03$	$2.7731E+03$	$2.8190E+03$	$2.8138E+03$	$2.7000E+03$
	STD	$3.5291E+01$	$0.0000E+00$	$1.7604E+01$	$1.0315E+01$	$6.7929E+00$	$1.3657E+01$	$1.0399E+01$	$3.4188E-13$
	Rank	8	1	3	5	4	7	6	2
	p value		$1.8215E-05$	$1.8215E-05$	$6.0677E-04$	$2.6691E-05$	$1.5313E-01$	$3.9672E-02$	$1.8215E-05$
F23	AVG	$2.7134E+03$	$0.0000E+00$	$2.8004E+03$	$2.8002E+03$	$2.8023E+03$	$2.8002E+03$	$2.8003E+03$	$2.7947E+03$
	STD	$3.4010E+01$	$0.0000E+00$	$7.7142E-02$	$3.5414E-02$	$3.1306E+01$	$3.3575E-02$	$9.8684E-02$	$1.8482E+02$
	Rank	2	1	7	4	8	5	6	3
	p value		$1.8215E-05$	$3.8838E-05$	$3.8838E-05$	$3.0270E-05$	$3.8838E-05$	$3.8838E-05$	$1.0172E-03$

TABLE 6: Continued.

		MEWOA	HCLPSO	SADE	JADE	CLPSO	LSHADE	LSHADE_ES	MSCA
F24	AVG	$6.2407E + 03$	$0.0000E + 00$	$4.9086E + 03$	$4.6702E + 03$	$5.2973E + 03$	$5.5069E + 03$	$5.6285E + 03$	$6.0305E + 03$
	STD	$2.0232E + 02$	$0.0000E + 00$	$1.6887E + 02$	$2.0066E + 02$	$8.6157E + 01$	$1.9325E + 02$	$1.3858E + 02$	$1.5676E + 02$
	Rank	8	1	3	2	4	5	6	7
	p value		$1.8215E - 05$	$1.8215E - 05$	$1.8215E - 05$	$1.8215E - 05$	$1.8215E - 05$	$1.8215E - 05$	$2.6998E - 03$
F25	AVG	$1.1362E + 04$	$0.0000E + 00$	$6.7031E + 03$	$6.3849E + 03$	$7.6197E + 03$	$7.8583E + 03$	$1.0152E + 04$	$1.4004E + 04$
	STD	$1.1444E + 03$	$0.0000E + 00$	$5.4002E + 02$	$6.6193E + 02$	$1.1661E + 03$	$1.0245E + 03$	$9.7023E + 02$	$1.2833E + 03$
	Rank	7	1	3	2	4	5	6	8
	p value		$1.8215E - 05$	$1.8215E - 05$	$1.8215E - 05$	$1.8215E - 05$	$1.8215E - 05$	$1.6731E - 03$	$3.4301E - 05$
F26	AVG	$3.8176E + 08$	$0.0000E + 00$	$6.2856E + 03$	$4.4561E + 03$	$1.5026E + 04$	$4.5562E + 03$	$5.6922E + 06$	$4.6298E + 08$
	STD	$2.1098E + 08$	$0.0000E + 00$	$8.1826E + 02$	$2.2726E + 02$	$3.6346E + 03$	$1.6183E + 02$	$2.7859E + 07$	$2.9315E + 08$
	Rank	7	1	4	2	5	3	6	8
	p value		$1.8215E - 05$	$1.8215E - 05$	$1.8215E - 05$	$1.8215E - 05$	$1.8215E - 05$	$1.8215E - 05$	$4.5757E - 01$
F27	AVG	$1.2546E + 05$	$0.0000E + 00$	$3.4105E + 04$	$1.3837E + 04$	$6.8084E + 04$	$1.6085E + 04$	$1.5161E + 04$	$7.9458E + 06$
	STD	$1.6955E + 05$	$0.0000E + 00$	$1.0053E + 04$	$2.2441E + 03$	$1.4559E + 04$	$5.3295E + 03$	$2.0803E + 03$	$2.9451E + 06$
	Rank	7	1	5	2	6	4	3	8
	p value		$1.8215E - 05$	$3.2520E - 03$	$1.8215E - 05$	$1.0000E + 00$	$1.8215E - 05$	$1.8215E - 05$	$1.8215E - 05$

0.0127048. Some more algorithms were used to solve this problem that can be seen in the harmony search (IHS) algorithm [170] and RO algorithm [171]. Experimental results show that the weight of the model obtained by MEWOA is 0.0126788, as shown in Table 7, which is smaller than the minimum value obtained by other methods.

4.7.2. Welded Beam Design Problem. The aim of the welded beam design model [169] is to achieve the lowest welded beam manufacturing cost. The model includes the following four constraint variables: critical buckling load (P_c), shear stress (τ), internal bending stress of the beam (θ), and deflection rate (δ). The steel bar height (t), weld seam thickness (h), steel bar thickness (b), and steel bar length (l) are the direct parameters that affect the manufacturing cost of welded beams. The mathematical model is as follows:

Consider $\vec{x} = [\, x_1 \;\; x_2 \;\; x_3 \;\; x_4 \,] = [\, h \;\; l \;\; t \;\; b \,]$

Objective

$$f(\vec{x})_{\min} = 1.10471 x_2 x_1^2 + 0.04811 x_3 x_4 (14.0 + x_2)$$

subject to

$$g_1(\vec{x}) = \tau(\vec{x}) - \tau_{\max} \leq 0,$$

$$g_2(\vec{x}) = \sigma(\vec{x}) - \sigma_{\max} \leq 0,$$

$$g_3(\vec{x}) = \delta(\vec{x}) - \delta_{\max} \leq 0,$$

$$g_4(\vec{x}) = x_1 - x_4 \leq 0,$$

$$g_5(\vec{x}) = P - P_C(\vec{x}) \leq 0,$$

$$g_6(\vec{x}) = 0.125 - x_1 \leq 0,$$

$$g_7(\vec{x}) = 1.10471 x_1^2 + 0.04811 x_3 x_4 (14.0 + x_2) - 5.0 \leq 0.$$

$$(16)$$

Variable ranges:

$$
\begin{aligned}
0.1 &\leq x_1 \leq 2, \\
0.1 &\leq x_2 \leq 10, \\
0.1 &\leq x_3 \leq 10, \\
0.1 &\leq x_4 \leq 2,
\end{aligned}
\tag{17}
$$

where

$$(\vec{x}) = \sqrt{(\tau')^2 + 2\tau'\tau'' \frac{x_2}{2R} + (\tau'')^2},$$

$$\tau' = \frac{P}{\sqrt{2} x_1 x_2},$$

$$\tau'' = \frac{MR}{J},$$

$$M = P\left(L + \frac{x_2}{2}\right),$$

$$R = \sqrt{\frac{x_2^2}{4} + \left(\frac{x_1 + x_3}{2}\right)^2},$$

$$J = 2\left\{\sqrt{2}\, x_1 x_2 \left[\frac{x_2^2}{4} + \left(\frac{x_1 + x_3}{2}\right)^2\right]\right\},$$

$$\sigma(\vec{x}) = \frac{6PL}{x_4 x_3^2},$$

$$\delta(\vec{x}) = \frac{6PL^3}{E x_3^2 x_4},$$

$$P_C(\vec{x}) = \frac{4.013E\sqrt{(x_3^2 x_4^6/36)}}{L^2}\left(1 - \frac{x_3}{2L}\sqrt{\frac{E}{4G}}\right),$$

$$P = 60001b, L = 14 \text{ in.}.\delta_{\max} = 0.25 \text{ in.}.,$$

$$E = 30 \times 1^6 \text{psi}, G = 12 \times 10^6 \text{psi},$$

$$\tau_{\max} = 13600 \text{psi}, \sigma_{\max} = 30000 \text{psi}.$$

$$(18)$$

F1

F2

F11

F12

F14

F18
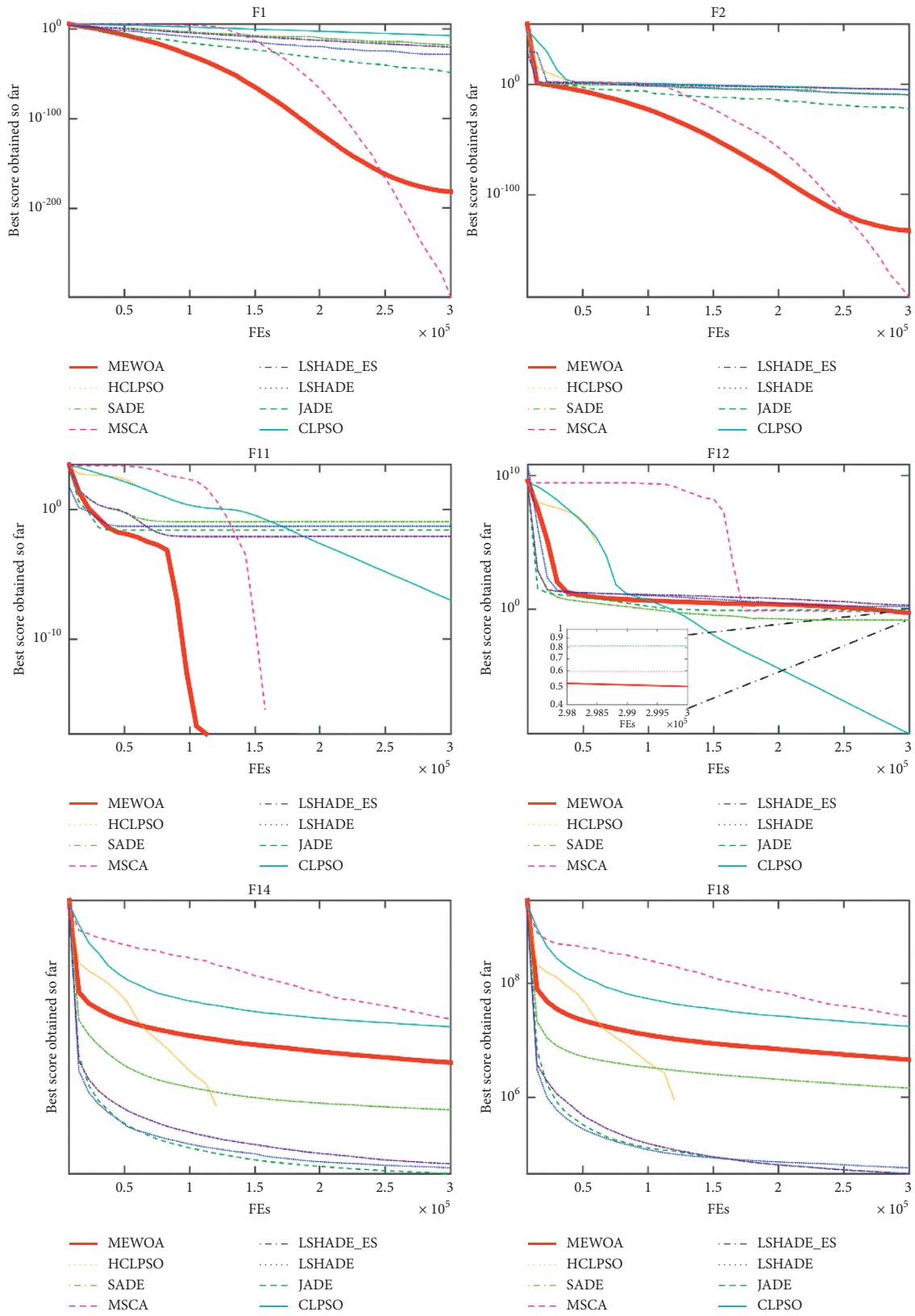
(a)

Figure 7: Continued.

(b)
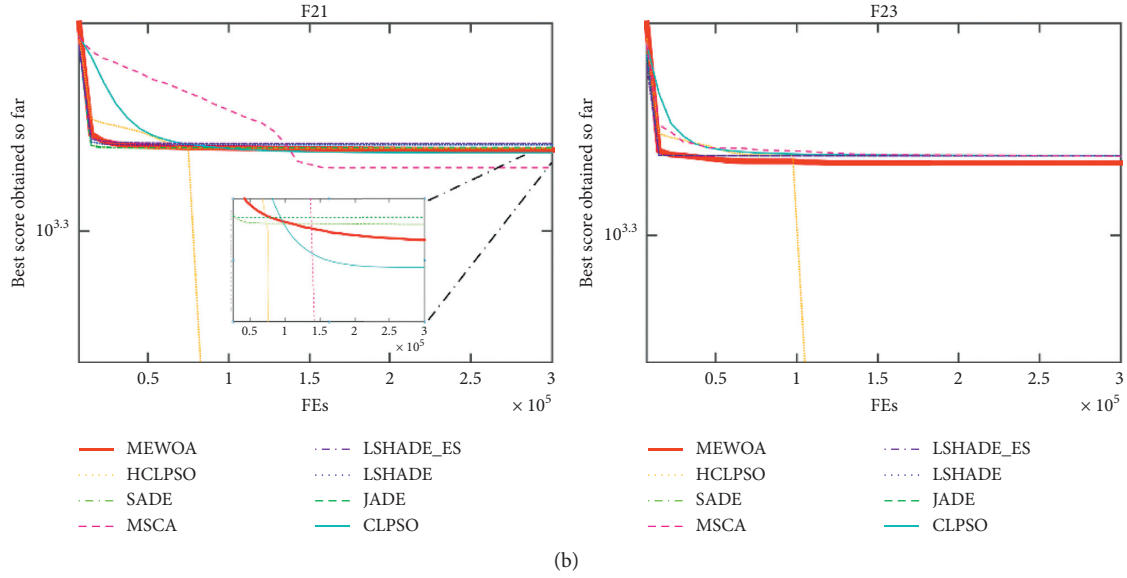
FIGURE 7: Convergence trends of MEWOA and advanced algorithms.

TABLE 7: Comparison results of MEWOA and other algorithms on the tension/compression spring case.

Method	Best variables			Best weight
	d	N	D	
MEWOA	0.051579	0.354086	11.44504	0.012666
WOA [85]	0.051207	12.0043032	0.345215	0.0126763
PSO [168]	0.015728	11.244543	0.357644	0.0126747
GA [169]	0.051480	11.632201	0.351661	0.0127048
RO [171]	0.051370	11.762790	0.349096	0.0126788
IHS [170]	0.051154	12.076432	0.349871	0.0126706
Constraint correction [166]	0.050000	14.250000	0.315900	0.0128334
Math. Optimization [167]	0.053396	901854000	0.399180	0.0127303

Some scholars use mathematical techniques or meta-heuristic techniques to solve the model. Kaveh and Khayatazad [171] adopted RO to solve the manufacturing cost of the model. The enhanced HS model IHS [170] was also used to calculate the model's manufacturing cost. Radgsdell and Phillips [172] used Davidon-Fletcher-Powell, Richardson's random method, and the Simplex method to solve the model's minimum manufacturing cost. As shown in Table 8, when the parameters were set to 0.1885, 3.471, 9.11343, and 0.206754, MEWOA obtained the minimum manufacturing cost of the welded beam of 1.720001. It proves that the MEWOA possesses a very good effect in this engineering problem.

4.7.3. I-Beam Design Problem. We used the MEWOA method to solve the I-beam design problem by optimizing the four parameters, including the I-beam length, two thicknesses, and height, to get the minimum vertical deflection. The mathematical model is as follows:

Consider $\vec{x} = \begin{bmatrix} x_1 & x_2 & x_3 & x_4 \end{bmatrix} = \begin{bmatrix} b & h & t_w & t_f \end{bmatrix}$

Objective $f(\vec{x})_{\min} = 5000/((t_w(h - 2t_f)^3/12) + (bt_f^3/6) + 2bt_f((h - t_f)/2)^2)$

subject to $g(\vec{x}) = 2bt_w + t_w (h - 2t_f) \leq 0$

Variable range:

$$10 \leq x_1 \leq 50,$$
$$10 \leq x_2 \leq 80,$$
$$0.9 \leq x_3 \leq 5,$$
$$0.9 \leq x_4 \leq 5.$$

(19)

Wang used the ARSM [174] method to solve the model and obtained a minimum vertical deflection of 0.0157. The minimum vertical deflection optimized by the improved method IARSM is 0.0131. Gandomi et al. [175] utilized CS to decrease the minimum vertical deflection to 0.0130747. Cheng and Prayogo [176] used SOS to obtain deflection the value of 0.0130741. Table 9 demonstrates that the I-beam's vertical deflection obtained by the MEWOA algorithm is 0.0130741, and the experimental result is better than other comparison methods.

Table 8: Comparison results of MEWOA and other algorithms on the welded beam case.

Technique	Best variables				Best cost
	h	L	t	b	
MEWOA	0.1885	3.471	9.11343	0.206754	1.720001
RO [171]	0.203687	3.528467	9.004233	0.207241	1.735344
CDE [173]	0.203137	3.542998	9.033498	0.206179	1.733462
IHS [170]	0.20573	3.47049	9.03662	0.20573	1.7248

Table 9: Comparison results of MEWOA and other algorithms on the I-beam case.

Algorithm	Best variables				Optimum vertical
	b	h	t_w	t_f	
MEWOA	50	80	0.9	2.32179	0.0130741
ARSM [174]	37.05	80	1.71	2.31	0.0157
IARSM [174]	48.42	79.99	0.90	2.40	0.0131
CS [175]	50	80	0.9	2.321675	0.0130747
SOS [176]	50	80	0.9	2.32179	0.0130741

5. Conclusions and Future Works

This article presents an enhanced MEWOA by integrating the opposition-based learning mechanism and MFO algorithm to enhance the balance between exploration and exploitation of the original WOA. Firstly, the MEWOA was estimated and compared with the basic algorithms in different dimensions to verify its effectiveness. Moreover, the devised MEWOA was also compared with six metaheuristic algorithms and five advanced algorithms to demonstrate its superiority. The experimental results proved that MEWOA has achieved much better performance than the original one. The convergence accuracy and scalability of MEWOA also have been improved a lot. The MEWOA can also effectively solve practical engineering problems. The results have shown that MEWOA can achieve a good balance between the exploration and exploitation ability and solve the constraint problem effectively.

In future work, we plan to improve the WOA in a deeper way from the principle of WOA. And the MEWOA can also be extended to a multiobjective version or binary version for other optimization tasks.

Data Availability

The data involved in this study are all public data, which can be downloaded through public channels.

Conflicts of Interest

The authors declare that they have no conflicts of interest.

Acknowledgments

References

[1] S. Qu, Y. Han, Z. Wu, and H. Raza, "Consensus modeling with asymmetric cost based on data-driven robust optimization," *Group Decision and Negotiation*, vol. 7, pp. 1–38, 2020.

[2] B. Cao, J. Zhao, Y. Gu, Y. Ling, and X. Ma, "Applying graph-based differential grouping for multiobjective large-scale optimization," *Swarm and Evolutionary Computation*, vol. 53, Article ID 100626, 2020.

[3] B. Cao, S. Fan, J. Zhao, P. Yang, K. Muhammad, and M. Tanveer, "Quantum-enhanced multiobjective large-scale optimization via parallelism," *Swarm and Evolutionary Computation*, vol. 57, Article ID 100697, 2020.

[4] B. Cao, "Multiobjective 3-D topology optimization of next-generation wireless data center network," *IEEE Transactions on Industrial Informatics*, vol. 16, no. 5, pp. 3597–3605, 2019.

[5] H. Huang, X. a. Feng, S. Zhou et al., "A new fruit fly optimization algorithm enhanced support vector machine for diagnosis of breast cancer based on high-level features," *BMC Bioinformatics*, vol. 20, no. S8, 2019.

[6] B. Cao, "Hybrid Microgrid many-objective sizing optimization with fuzzy decision," *IEEE Transactions on Fuzzy Systems*, vol. 28, no. 11, 2020.

[7] B. Cao, X. Wang, W. Zhang, H. Song, and Z. Lv, "A many-objective optimization model of industrial internet of things based on private blockchain," *IEEE Network*, vol. 34, no. 5, pp. 78–83, 2020.

[8] W. Deng, "An improved quantum-inspired differential evolution algorithm for deep belief network," *IEEE Transactions on Instrumentation & Measurement*, vol. 69, 2020.

[9] H. Zhao, "Performance prediction using high-order differential mathematical morphology gradient spectrum entropy and extreme learning machine," *IEEE Transactions on Instrumentation & Measurement*, vol. 69, 2019.

[10] W. Deng, "A novel gate resource allocation method using improved PSO-based QEA," *IEEE Transactions on Intelligent Transportation Systems*, vol. 19, 2020.

[11] H. Chen, A. A. Heidari, H. Chen, M. Wang, Z. Pan, and A. H. Gandomi, "Multi-population differential evolution-assisted Harris hawks optimization: framework and case studies," *Future Generation Computer Systems*, vol. 111, pp. 175–198, 2020.

[12] Y. Xu, H. Chen, J. Luo, Q. Zhang, S. Jiao, and X. Zhang, "Enhanced Moth-flame optimizer with mutation strategy for global optimization," *Information Sciences*, vol. 492, pp. 181–203, 2019.

[13] X. Xu and H.-l. Chen, "Adaptive computational chemotaxis based on field in bacterial foraging optimization," *Soft Computing*, vol. 18, no. 4, pp. 797–807, 2014.

[14] H. Chen, Y. Xu, M. Wang, and X. Zhao, "A balanced whale optimization algorithm for constrained engineering design problems," *Applied Mathematical Modelling*, vol. 71, pp. 45–59, 2019.

[15] H. Yu, N. Zhao, P. Wang, H. Chen, and C. Li, "Chaos-enhanced synchronized bat optimizer," *Applied Mathematical Modelling*, vol. 77, pp. 1201–1215, 2020.

[16] H. L. Chen, M. J. Wang, and X. H. Zhao, "A multi-strategy enhanced sine cosine algorithm for global optimization and constrained practical engineering problems," *Applied Mathematics and Computation*, vol. 369, 2020.

[17] X. Zhang, Y. Xu, C. Yu et al., "Gaussian mutational chaotic fruit fly-built optimization and feature selection," *Expert Systems with Applications*, vol. 141, Article ID 112976, 2020.

[18] M. A. Al-Betar, "Survival exploration strategies for Harris hawks optimizer," *Expert Systems with Applications*, vol. 168, 2020.

[19] J. Luo, H. Chen, Q. zhang, Y. Xu, H. Huang, and X. Zhao, "An improved grasshopper optimization algorithm with application to financial stress prediction," *Applied Mathematical Modelling*, vol. 64, pp. 654–668, 2018.

[20] H. L. Chen, "Efficient multi-population outpost fruit fly-driven optimizers: framework and advances in support vector machines," *Expert Systems with Applications*, vol. 142, 2020.

[21] H. Chen, C. Yang, A. A. Heidari, and X. Zhao, "An efficient double adaptive random spare reinforced whale optimization algorithm," *Expert Systems with Applications*, vol. 154, Article ID 113018, 2020.

[22] A. A. Heidari, I. Aljarah, H. Faris, H. Chen, J. Luo, and S. Mirjalili, "An enhanced associative learning-based exploratory whale optimizer for global optimization," *Neural Computing & Applications*, vol. 32, no. 9, pp. 5185–5211, 2019.

[23] L. Shen, H. Chen, Z. Yu et al., "Evolving support vector machines using fruit fly optimization for medical data classification," *Knowledge-Based Systems*, vol. 96, pp. 61–75, 2016.

[24] Y. Zhang, R. Liu, X. Wang, H. Chen, and C. Li, "Boosted binary Harris hawks optimizer and feature selection," *Engineering with Computers*, vol. 57, 2020.

[25] X. Zhao, D. Li, B. Yang, C. Ma, Y. Zhu, and H. Chen, "Feature selection based on improved ant colony optimization for online detection of foreign fiber in cotton," *Applied Soft Computing*, vol. 24, pp. 585–596, 2014.

[26] M. Wang and H. Chen, "Chaotic multi-swarm whale optimizer boosted support vector machine for medical diagnosis," *Applied Soft Computing*, vol. 88, Article ID 105946, 2020.

[27] X. Zhao, D. Li, B. Yang et al., "A two-stage feature selection method with its application," *Computers & Electrical Engineering*, vol. 47, pp. 114–125, 2015.

[28] C. Li, L. Hou, B. Y. Sharma et al., "Developing a new intelligent system for the diagnosis of tuberculous pleural effusion," *Computer Methods and Programs in Biomedicine*, vol. 153, pp. 211–225, 2018.

[29] M. Wang, H. Chen, B. Yang et al., "Toward an optimal kernel extreme learning machine using a chaotic moth-flame optimization strategy with applications in medical diagnoses," *Neurocomputing*, vol. 267, pp. 69–84, 2017.

[30] J. Xia, H. Chen, Q. Li et al., "Ultrasound-based differentiation of malignant and benign thyroid Nodules: an extreme learning machine approach," *Computer Methods and Programs in Biomedicine*, vol. 147, pp. 37–49, 2017.

[31] H.-L. Chen, G. Wang, C. Ma, Z.-N. Cai, W.-B. Liu, and S.-J. Wang, "An efficient hybrid kernel extreme learning machine approach for early diagnosis of Parkinson's disease," *Neurocomputing*, vol. 184, pp. 131–144, 2016.

[32] L. Hu, G. Hong, J. Ma, X. Wang, and H. Chen, "An efficient machine learning approach for diagnosis of paraquat-poisoned patients," *Computers in Biology and Medicine*, vol. 59, pp. 116–124, 2015.

[33] S.-J. Wang, H.-L. Chen, W.-J. Yan, Y.-H. Chen, and X. Fu, "Face recognition and micro-expression recognition based on discriminant tensor subspace analysis plus extreme learning machine," *Neural Processing Letters*, vol. 39, no. 1, pp. 25–43, 2014.

[34] X. Zhao, X. Zhang, Z. Cai et al., "Chaos enhanced grey wolf optimization wrapped ELM for diagnosis of paraquat-poisoned patients," *Computational Biology and Chemistry*, vol. 78, pp. 481–490, 2019.

[35] Y. Zhang, "Towards augmented kernel extreme learning models for bankruptcy prediction: algorithmic behavior and comprehensive analysis," *Neurocomputing*, vol. 430, 2020.

[36] C. Yu, M. Chen, K. Cheng et al., "SGOA: annealing-behaved grasshopper optimizer for global tasks," *Engineering with Computers*, vol. 26, 2021.

[37] Z. Cai, J. Gu, J. Luo et al., "Evolving an optimal kernel extreme learning machine by using an enhanced grey wolf optimization strategy," *Expert Systems with Applications*, vol. 138, Article ID 112814, 2019.

[38] M. Wang, H. Chen, H. Li et al., "Grey wolf optimization evolving kernel extreme learning machine: application to bankruptcy prediction," *Engineering Applications of Artificial Intelligence*, vol. 63, pp. 54–68, 2017.

[39] X. Wang, H. Chen, A. A. Heidari et al., "Multi-population following behavior-driven fruit fly optimization: a Markov chain convergence proof and comprehensive analysis," *Knowledge-Based Systems*, vol. 210, Article ID 106437, 2020.

[40] J. Tu, "Evolutionary biogeography-based Whale optimization methods with communication structure: towards measuring the balance," *Knowledge-Based Systems*, vol. 212, Article ID 106642, 2020.

[41] S. Song, "Dimension decided Harris hawks optimization with Gaussian mutation: balance analysis and diversity patterns," *Knowledge-Based Systems*, vol. 215, Article ID 106425, 2020.

[42] X. Liang, Z. Cai, M. Wang, X. Zhao, H. Chen, and C. Li, "Chaotic oppositional sine-cosine method for solving global optimization problems," *Engineering with Computers*, vol. 7, 2020.

[43] A. F. Ba, H. Huang, M. Wang et al., "Levy-based antlion-inspired optimizers with orthogonal learning scheme," *Engineering with Computers*, vol. 21, 2020.

[44] J. Yan, W. Pu, S. Zhou, H. Liu, and M. S. Greco, "Optimal resource allocation for asynchronous multiple targets tracking in heterogeneous radar networks," *IEEE Transactions on Signal Processing*, vol. 68, pp. 4055–4068, 2020.

[45] C. Li, L. Sun, Z. Xu, X. Wu, T. Liang, and W. Shi, "Experimental investigation and error analysis of high precision fbg displacement sensor for structural health monitoring," *International Journal of Structural Stability and Dynamics*, vol. 20, no. 6, Article ID 2040011, 2020.

[46] L. Sun, C. Li, C. Zhang, T. Liang, and Z. Zhao, "The strain transfer mechanism of fiber bragg grating sensor for extra large strain monitoring," *Sensors*, vol. 19, no. 8, Article ID 1851, 2019.

[47] C. Zhang, "Fibre Bragg grating sensor-based damage response monitoring of an asymmetric reinforced concrete shear wall structure subjected to progressive seismic loads," *Structural Control and Health Monitoring*, vol. 26, no. 3, Article ID e2307, 2019.

[48] L. Sun, C. Li, C. Zhang, Z. Su, and C. Chen, "Early monitoring of rebar corrosion evolution based on FBG sensor," *International Journal of Structural Stability and Dynamics*, vol. 18, no. 8, Article ID 1840001, 2018.

[49] C. Cai, "Selective laser melting of near-α titanium alloy Ti-6Al-2Zr-1Mo-1V: parameter optimization, heat treatment and mechanical performance," *Journal of Materials Science & Technology*, vol. 57, 2020.

[50] C. Cai, "Hot isostatic pressing of a near α-Ti alloy: temperature optimization, microstructural evolution and mechanical performance evaluation," *Materials Science and Engineering: A*, vol. 802, Article ID 140426, 2020.

[51] H. Kordestani and C. Zhang, "E-direct use of the savitzky-golay filter to develop an output-only trend line-based damage detection method," *Sensors*, vol. 20, no. 7, Article ID 1983, 2020.

[52] A. A. Mousavi, C. Zhang, S. F. Masri, and G. Gholipour, "Structural damage localization and quantification based on a CEEMDAN hilbert transform neural network approach: a model steel truss bridge case study," *Sensors*, vol. 20, no. 5, Article ID 1271, 2020.

[53] X. Wang, Y. Liu, and K. R. Choo, "Fault tolerant multi-subset aggregation scheme for smart grid," *IEEE Transactions on Industrial Informatics*, vol. 171 page, 2020.

[54] B. Wang, B. F. Zhang, X. W. Liu, and F. C. Zou, "Novel infrared image enhancement optimization algorithm combined with DFOCS," *Optik*, vol. 224, Article ID 165476, 2020.

[55] Q. Zhu, "Research on road traffic situation awareness system based on image big data," *IEEE Intelligent Systems*, vol. 35, no. 1, pp. 18–26, 2019.

[56] Q. Jiang, "Unified no-reference quality assessment of singly and multiply distorted stereoscopic images," *IEEE Transactions on Image Processing*, vol. 28, no. 4, pp. 1866–1881, 2018.

[57] M. Xu, C. Li, S. Zhang, and P. L. Callet, "State-of-the-Art in 360° video/image processing: perception, assessment and compression," *IEEE Journal of Selected Topics in Signal Processing*, vol. 14, no. 1, pp. 5–26, 2020.

[58] M. Yang and A. Sowmya, "An underwater color image quality evaluation metric," *IEEE Transactions on Image Processing*, vol. 24, no. 12, pp. 6062–6071, 2015.

[59] B. Wang, B. Zhang, and X. Liu, "An image encryption approach on the basis of a time delay chaotic system," *Optik*, vol. 225, Article ID 165737, 2021.

[60] S. Hinojosa, D. Oliva, E. Cuevas, G. Pajares, D. Zaldivar, and M. Pérez-Cisneros, "Reducing overlapped pixels: a multiobjective color thresholding approach," *Soft Computing*, vol. 24, no. 9, pp. 6787–6807, 2020.

[61] D. Liu, S. Wang, D. Huang, G. Deng, F. Zeng, and H. Chen, "Medical image classification using spatial adjacent histogram based on adaptive local binary patterns," *Computers in Biology and Medicine*, vol. 72, pp. 185–200, 2016.

[62] D. Zhao, "Ant colony optimization with horizontal and vertical crossover search: fundamental visions for multi-threshold image segmentation," *Expert Systems with Applications*, vol. 167, Article ID 114122, 2020.

[63] D. Zhao, "Chaotic random spare ant colony optimization for multi-threshold image segmentation of 2D Kapur entropy," *Knowledge-Based Systems*, vol. 216, Article ID 106510, 2020.

[64] S. Li, H. Chen, M. Wang, A. A. Heidari, and S. Mirjalili, "Slime mould algorithm: a new method for stochastic optimization," *Future Generation Computer Systems*, vol. 111, pp. 300–323, 2020.

[65] A. A. Heidari, S. Mirjalili, H. Faris, I. Aljarah, M. Mafarja, and H. Chen, "Harris hawks optimization: algorithm and applications," *Future Generation Computer Systems*, vol. 97, pp. 849–872, 2019.

[66] R. Salgotra and U. Singh, "The naked mole-rat algorithm," *Neural Computing & Applications*, vol. 31, no. 12, pp. 8837–8857, 2019.

[67] Y. Yang, "Hunger games search: visions, conception, implementation, deep analysis, perspectives, and towards performance shifts," *Expert Systems with Applications*, vol. 177, 2021.

[68] G.-G. Wang, "Moth search algorithm: a bio-inspired metaheuristic algorithm for global optimization problems," *Memetic Computing*, vol. 10, no. 2, pp. 151–164, 2018.

[69] Y. Feng, S. Deb, G.-G. Wang, and A. H. Alavi, "Monarch butterfly optimization: a comprehensive review," *Expert Systems with Applications*, vol. 168, Article ID 114418, 2021.

[70] G.-G. Wang, A. H. Gandomi, A. H. Alavi, and D. Gong, "A comprehensive review of krill herd algorithm: variants, hybrids and applications," *Artificial Intelligence Review*, vol. 51, no. 1, pp. 119–148, 2019.

[71] N. Gao, D. Luo, B. Cheng, and H. Hou, "Teaching-learning-based optimization of a composite metastructure in the 0-10 kHz broadband sound absorption range," *Journal of the Acoustical Society of America*, vol. 148, no. 2, pp. EL125–EL129, 2020.

[72] G. Sun, "An adaptive differential evolution with combined strategy for global numerical optimization," *Soft Computing*, vol. 24, pp. 1–20, 2019.

[73] J. Liu, C. Wu, G. Wu, and X. Wang, "A novel differential search algorithm and applications for structure design," *Applied Mathematics and Computation*, vol. 268, pp. 246–269, 2015.

[74] S. Xu, "Computer vision techniques in construction: a critical review," *Archives of Computational Methods in Engineering*, vol. 28, pp. 3383–3397, 2020.

[75] B. Cao, "Security-aware industrial wireless sensor network deployment optimization," *IEEE Transactions on Industrial Informatics*, vol. 16, no. 8, pp. 5309–5316, 2019.

[76] C. Wu, P. Wu, J. Wang, R. Jiang, M. Chen, and X. Wang, "Ontological knowledge base for concrete bridge

rehabilitation project management," *Automation in Construction*, vol. 121, Article ID 103428, 2021.

[77] T. Qiu, X. Shi, J. Wang et al., "Deep learning: a rapid and efficient route to automatic metasurface design," *Advanced Science*, vol. 6, no. 12, Article ID 1900128, 2019.

[78] T. Li, M. Xu, C. Zhu, R. Yang, Z. Wang, and Z. Guan, "A deep learning approach for multi-frame in-loop filter of HEVC," *IEEE Transactions on Image Processing*, vol. 28, no. 11, pp. 5663–5678, 2019.

[79] H. Chen, A. Chen, L. Xu et al., "A deep learning CNN architecture applied in smart near-infrared analysis of water pollution for agricultural irrigation resources," *Agricultural Water Management*, vol. 240, Article ID 106303, 2020.

[80] Q. Jiang, G. Wang, S. Jin, Y. Li, and Y. Wang, "Predicting human microRNA-disease associations based on support vector machine," *International Journal of Data Mining and Bioinformatics*, vol. 8, no. 3, pp. 282–293, 2013.

[81] K. Qu, L. Wei, and Q. Zou, "A review of DNA-binding proteins prediction methods," *Current Bioinformatics*, vol. 14, no. 3, pp. 246–254, 2019.

[82] C. Wu, P. Wu, J. Wang, R. Jiang, M. Chen, and X. Wang, "Critical review of data-driven decision-making in bridge operation and maintenance," *Structure and Infrastructure Engineering*, vol. 21, pp. 1–24, 2020.

[83] S. Liu, "A variable weight-based hybrid approach for multi-attribute group decision making under interval valued intuitionistic fuzzy sets," *International Journal of Intelligent Systems*, vol. 39, 2020.

[84] S. Liu, F. T. S. Chan, and W. Ran, "Decision making for the selection of cloud vendor: an improved approach under group decision-making with integrated weights and objective/subjective attributes," *Expert Systems with Applications*, vol. 55, pp. 37–47, 2016.

[85] S. Mirjalili and A. Lewis, "The whale optimization algorithm," *Advances in Engineering Software*, vol. 95, pp. 51–67, 2016.

[86] W. L. Wang, W. K. Li, Z. Wang, and L. Li, "Opposition-based multi-objective whale optimization algorithm with global grid ranking," *Neurocomputing*, vol. 341, pp. 41–59, 2019.

[87] R. Salgotra, U. Singh, and S. Saha, "On some improved versions of whale optimization algorithm," *Arabian Journal for Science and Engineering*, vol. 44, no. 11, pp. 9653–9691, 2019.

[88] Y. Sun, T. Yang, and Z. Liu, "A whale optimization algorithm based on quadratic interpolation for high-dimensional global optimization problems," *Applied Soft Computing*, vol. 85, 2019.

[89] R. K. Agrawal, B. Kaur, and S. Sharma, "Quantum based whale optimization algorithm for wrapper feature selection," *Applied Soft Computing*, vol. 89, 2020.

[90] A. G. Hussien, "New binary whale optimization algorithm for discrete optimization problems," *Engineering Optimization*, vol. 52, no. 6, 2019.

[91] J. Luo, H. Chen, A. A. Heidari, Y. Xu, Q. Zhang, and C. Li, "Multi-strategy boosted mutative whale-inspired optimization approaches," *Applied Mathematical Modelling*, vol. 73, pp. 109–123, 2019.

[92] K. Shi, Y. Tang, X. Liu, and S. Zhong, "Non-fragile sampled-data robust synchronization of uncertain delayed chaotic Lurie systems with randomly occurring controller gain fluctuation," *ISA Transactions*, vol. 66, pp. 185–199, 2017.

[93] T. Wu, L. Xiong, J. Cheng, and X. Xie, "New results on stabilization analysis for fuzzy semi-Markov jump chaotic systems with state quantized sampled-data controller," *Information Sciences*, vol. 521, pp. 231–250, 2020.

[94] T. Wu, "New stabilization results for semi-markov chaotic systems with fuzzy sampled-data control," *Complexity*, vol. 2019, 2019.

[95] Y. Sun, X. Wang, Y. Chen, and Z. Liu, "A modified whale optimization algorithm for large-scale global optimization problems," *Expert Systems with Applications*, vol. 114, pp. 563–577, 2018.

[96] F. Hemasian-Etefagh and F. Safi-Esfahani, "Group-based whale optimization algorithm," *Soft Computing*, vol. 24, no. 5, pp. 3647–3673, 2020.

[97] M. A. Elaziz and S. Mirjalili, "A hyper-heuristic for improving the initial population of whale optimization algorithm," *Knowledge-Based Systems*, vol. 172, pp. 42–63, 2019.

[98] W. Guo, "An improved whale optimization algorithm for forecasting water resources demand," *Applied Soft Computing*, vol. 86, 2020.

[99] S. T. Revathi, N. Ramaraj, and S. Chithra, "Brain storm-based whale optimization algorithm for privacy-protected data publishing in cloud computing," *Cluster Computing-the Journal of Networks Software Tools and Applications*, vol. 22, no. 2, pp. S3521–S3530, 2019.

[100] S. Gong, W. Gao, and F. Abza, "Brain tumor diagnosis based on artificial neural network and a chaos whale optimization algorithm," *Computational Intelligence*, vol. 36, no. 1, pp. 259–275, 2020.

[101] N. Zhang, Y. X Cai, Y. Y Wang, Y. T Tian, X. L Wang, and B Badami, "Skin cancer diagnosis based on optimized convolutional neural network," *Artificial Intelligence in Medicine*, vol. 102, Article ID 101756, 2020.

[102] G. Xiong, J. Zhang, D. Shi, and Y. He, "Parameter extraction of solar photovoltaic models using an improved whale optimization algorithm," *Energy Conversion and Management*, vol. 174, pp. 388–405, 2018.

[103] M. Petrović, Z. Miljkovic, and A. Jokic, "A novel methodology for optimal single mobile robot scheduling using whale optimization algorithm," *Applied Soft Computing*, vol. 81, 2019.

[104] L.-L. Li, J. Sun, M.-L. Tseng, and Z.-G. Li, "Extreme learning machine optimized by whale optimization algorithm using insulated gate bipolar transistor module aging degree evaluation," *Expert Systems with Applications*, vol. 127, pp. 58–67, 2019.

[105] S. Akyol and B. Alatas, "Sentiment classification within online social media using whale optimization algorithm and social impact theory based optimization," *Physica A-Statistical Mechanics and Its Applications*, vol. 540, 2020.

[106] W. Qiao, "Short-term natural gas consumption prediction based on Volterra adaptive filter and improved whale optimization algorithm," *Engineering Applications of Artificial Intelligence*, vol. 87, 2020.

[107] X. Ye, "Modified whale optimization algorithm for solar cell and PV module parameter identification," *Complexity*, vol. 2021, Article ID 8878686, , 2021.

[108] S. Mirjalili, "Moth-flame optimization algorithm: a novel nature-inspired heuristic paradigm," *Knowledge-Based Systems*, vol. 89, pp. 228–249, 2015.

[109] Y. Xu, H. Chen, A. A. Heidari et al., "An efficient chaotic mutative moth-flame-inspired optimizer for global optimization tasks," *Expert Systems with Applications*, vol. 129, pp. 135–155, 2019.

[110] S. Yang, "Scalable digital neuromorphic architecture for large-scale biophysically meaningful neural network with

multi-compartment neurons," *IEEE transactions on neural networks and learning systems*, vol. 31, no. 1, pp. 148–162, 2019.

[111] T. Ni, H. Chang, T. Song et al., "Non-intrusive online distributed pulse shrinking-based interconnect testing in 2.5D IC," *IEEE Transactions on Circuits and Systems II: Express Briefs*, vol. 67, no. 11, pp. 2657–2661, 2020.

[112] H. Zhang, Z. Qiu, J. Cao, M. Abdel-Aty, and L. Xiong, "Event-triggered synchronization for Neutral-Type semi-Markovian neural networks with partial mode-dependent time-varying delays," *IEEE Transactions on Neural Networks and Learning Systems*, vol. 31, no. 11, pp. 4437–4450, 2020.

[113] J. Derrac, S. García, D. Molina, and F. Herrera, "A practical tutorial on the use of nonparametric statistical tests as a methodology for comparing evolutionary and swarm intelligence algorithms," *Swarm and Evolutionary Computation*, vol. 1, no. 1, pp. 3–18, 2011.

[114] S. García, A. Fernández, J. Luengo, and F. Herrera, "Advanced nonparametric tests for multiple comparisons in the design of experiments in computational intelligence and data mining: experimental analysis of power," *Information Sciences*, vol. 180, no. 10, pp. 2044–2064, 2010.

[115] H. R. Tizhoosh, "Opposition-based learning: a new scheme for machine intelligence," in *Proceedings of the International Conference on Computational Intelligence for Modelling, Control and Automation and International Conference on Intelligent Agents, Web Technologies and Internet Commerce (CIMCA-IAWTIC'06)*, Vienna, Austria, November 2005.

[116] N. Awad, "Problem definitions and evaluation criteria for the CEC 2017 special session and competition on single objective real-parameter numerical optimization," Technical Report, 2016.

[117] V. Bhargava, S. E. K. Fateen, and A. Bonilla-Petriciolet, "Cuckoo Search: a new nature-inspired optimization method for phase equilibrium calculations," *Fluid Phase Equilibria*, vol. 337, pp. 191–200, 2013.

[118] S. Saremi, S. Mirjalili, and A. Lewis, "Grasshopper optimisation algorithm: theory and application," *Advances in Engineering Software*, vol. 105, pp. 30–47, 2017.

[119] N. Lynn and P. N. Suganthan, "Heterogeneous comprehensive learning particle swarm optimization with enhanced exploration and exploitation," *Swarm and Evolutionary Computation*, vol. 24, pp. 11–24, 2015.

[120] M. G. H. Omran, A. Salman, and A. P. Engelbrecht, "Self-adaptive differential evolution," in *Proceedings of the Computational Intelligence and Security*, pp. 192–199, Guangzhou, China, December 2005.

[121] J. Jingqiao Zhang and A. C. Sanderson, "JADE: adaptive differential evolution with optional external archive," *IEEE Transactions on Evolutionary Computation*, vol. 13, no. 5, pp. 945–958, 2009.

[122] J. J. Liang, A. K. Qin, P. N. Suganthan, and S. Baskar, "Comprehensive learning particle swarm optimizer for global optimization of multimodal functions," *IEEE Transactions on Evolutionary Computation*, vol. 10, no. 3, pp. 281–295, 2006.

[123] R. Tanabe and A. S. Fukunaga, "Improving the search performance of SHADE using linear population size reduction," in *Proceedings of the Evolutionary Computation*, Beijing, China, July 2014.

[124] N. H. Awad, M. Z. Ali, and P. N. Suganthan, "Ensemble sinusoidal differential covariance matrix adaptation with Euclidean neighborhood for solving CEC2017 benchmark problems," in *Proceedings of the 2017 IEEE Congress on Evolutionary Computation (CEC)*, Donostia, Spain, June 2017.

[125] X. Fei, J. Wang, S. Ying, Z. Hu, and J. Shi, "Projective parameter transfer based sparse multiple empirical kernel learning Machine for diagnosis of brain disease," *Neurocomputing*, vol. 413, pp. 271–283, 2020.

[126] H. Zhao, X. Qiu, W. Lu, H. Huang, and X. Jin, "High-quality retinal vessel segmentation using generative adversarial network with a large receptive field," *International Journal of Imaging Systems and Technology*, vol. 30, no. 3, pp. 828–842, 2020.

[127] T. Wang, "Video deblurring via spatiotemporal pyramid network and adversarial gradient prior," *Computer Vision and Image Understanding*, vol. 203, Article ID 103135, 2020.

[128] X. Zhang, R. Jiang, T. Wang, P. Huang, and L. Zhao, "Attention-based interpolation network for video deblurring," *Neurocomputing*, vol. 453, pp. 865–875, 2021.

[129] X. Zhang, R. Jiang, T. Wang, and J. Wang, "Recursive neural network for video deblurring," *IEEE Transactions on Circuits and Systems for Video Technology*, vol. 31, no. 8, pp. 3025–3036, 2021.

[130] X. Zhang, T. Wang, J. Wang, G. Tang, and L. Zhao, "Pyramid channel-based feature attention network for image dehazing," *Computer Vision and Image Understanding*, vol. 198, Article ID 103003, 2020.

[131] Y. Li, W.-G. Cui, H. Huang, Y.-Z. Guo, K. Li, and T. Tan, "Epileptic seizure detection in EEG signals using sparse multiscale radial basis function networks and the Fisher vector approach," *Knowledge-Based Systems*, vol. 164, pp. 96–106, 2019.

[132] Y. Li, J. Liu, Z. Tang, and B. Lei, "Deep spatial-temporal feature fusion from adaptive dynamic functional connectivity for MCI identification," *IEEE Transactions on Medical Imaging*, vol. 39, no. 9, pp. 2818–2830, 2020.

[133] X. Zhang, M. Fan, D. Wang, P. Zhou, and D. Tao, "Top-k feature selection framework using robust 0-1 integer programming," *IEEE Transactions on Neural Networks and Learning Systems*, vol. 32, no. 7, pp. 3005–3019, 2021.

[134] X. Wu, X. Xu, J. Liu, H. Wang, B. Hu, and F. Nie, "Supervised feature selection with orthogonal regression and feature weighting," *IEEE Transactions on Neural Networks and Learning Systems*, vol. 32, no. 5, pp. 1831–1838, 2021.

[135] N. Gu, M. Fan, L. Du, and D. Ren, "Efficient sequential feature selection based on adaptive eigenspace model," *Neurocomputing*, vol. 161, pp. 199–209, 2015.

[136] M. Fan, N. Gu, H. Qiao, and B. Zhang, "Dimensionality reduction: an interpretation from manifold regularization perspective," *Information Sciences*, vol. 277, pp. 694–714, 2014.

[137] H. M. Ridha, C. Gomes, H. Hizam, M. Ahmadipour, A. A. Heidari, and H. Chen, "Multi-objective optimization and multi-criteria decision-making methods for optimal design of standalone photovoltaic system: a comprehensive review," *Renewable and Sustainable Energy Reviews*, vol. 135, Article ID 110202, 2021.

[138] H. Chen, S. Jiao, M. Wang, A. A. Heidari, and X. Zhao, "Parameters identification of photovoltaic cells and modules using diversification-enriched Harris hawks optimization with chaotic drifts," *Journal of Cleaner Production*, vol. 244, Article ID 118778, 2020.

[139] A. Abbassi, R. Abbassi, A. A. Heidari et al., "Parameters identification of photovoltaic cell models using enhanced exploratory salp chains-based approach," *Energy*, vol. 198, Article ID 117333, 2020.

[140] H. Zhang, A. A. Heidari, M. Wang, L. Zhang, H. Chen, and C. Li, "Orthogonal Nelder-Mead moth flame method for parameters identification of photovoltaic modules," *Energy Conversion and Management*, vol. 211, Article ID 112764, 2020.

[141] Y. Liu, G. Chong, A. A. Heidari et al., "Horizontal and vertical crossover of Harris hawk optimizer with Nelder-Mead simplex for parameter estimation of photovoltaic models," *Energy Conversion and Management*, vol. 223, Article ID 113211, 2020.

[142] J. Li, C. Chen, H. Chen, and C. Tong, "Towards context-aware social recommendation via individual trust," *Knowledge-Based Systems*, vol. 127, pp. 58–66, 2017.

[143] J. Li and J. Lin, "A probability distribution detection based hybrid ensemble QoS prediction approach," *Information Sciences*, vol. 519, pp. 289–305, 2020.

[144] J. Li, X.-L. Zheng, S.-T. Chen, W.-W. Song, and D.-r. Chen, "An efficient and reliable approach for quality-of-service-aware service composition," *Information Sciences*, vol. 269, pp. 238–254, 2014.

[145] Q. Li, X. Wu, and T. Liu, "Differentiable neural architecture search for optimal spatial/temporal brain function network decomposition," *Medical Image Analysis*, vol. 69, Article ID 101974, 2021.

[146] Z. Zhu, Z. Zhen, X. Wu, and S. Li, "Estimating functional connectivity by integration of inherent brain function activity pattern priors," *IEEE/ACM Transactions on Computational Biology and Bioinformatics*, vol. 951 page, 2020.

[147] X. Li, H. Huang, H. Zhao, Y. Wang, and M. Hu, "Learning a convolutional neural network for propagation-based stereo image segmentation," *The Visual Computer*, vol. 36, no. 1, pp. 39–52, 2020.

[148] X. Li, H. Zhao, H. Huang, Z. Hu, and L. Xiao, "Interactive image recoloring by combining global and local optimization," *Multimedia Tools and Applications*, vol. 75, no. 11, pp. 6431–6443, 2016.

[149] H. Huang, X. Li, H. Zhao, G. Nie, Z. Hu, and L. Xiao, "Manifold-preserving image colorization with nonlocal estimation," *Multimedia Tools and Applications*, vol. 74, no. 18, pp. 7555–7568, 2015.

[150] T. Wang, "Haze concentration adaptive network for image dehazing," *Neurocomputing*, vol. 439, 2021.

[151] P. Huang, "Self-filtering image dehazing with self-supporting module," *Neurocomputing*, vol. 432, pp. 57–69, 2020.

[152] X. Zhang, T. Wang, W. Luo, and P. Huang, "Multi-level fusion and attention-guided CNN for image dehazing," *IEEE Transactions on Circuits and Systems for Video Technology*, vol. 25, no. 1, 2020.

[153] L. Zhang, Y. Zou, W. Wang, Z. Jin, Y. Su, and H. Chen, "Resource allocation and trust computing for blockchain-enabled edge computing system," *Computers & Security*, vol. 105, Article ID 102249, 2021.

[154] L. Zhang, "A covert communication method using special bitcoin addresses generated by vanitygen," *Computers, Materials \& Continua*, vol. 65, no. 1, pp. 597–616, 2020.

[155] L. Zhang, Z. Zhang, W. Wang, Z. Jin, Y. Su, and H. Chen, "Research on a covert communication model realized by using smart contracts in blockchain environment," *IEEE Systems Journal*, vol. 12, no. 1, 2021.

[156] Y. Wei, H. Lv, M. Chen et al., "Predicting entrepreneurial intention of students: an extreme learning machine with Gaussian barebone Harris hawks optimizer," *IEEE Access*, vol. 8, pp. 76841–76855, 2020.

[157] W. Zhu, C. Ma, X. Zhao et al., "Evaluation of sino foreign cooperative education project using orthogonal sine cosine optimized kernel extreme learning machine," *IEEE Access*, vol. 8, pp. 61107–61123, 2020.

[158] A. Lin, Q. Wu, A. A. Heidari et al., "Predicting intentions of students for master programs using a chaos-induced sine cosine-based fuzzy K-nearest neighbor classifier," *IEEE Access*, vol. 7, pp. 67235–67248, 2019.

[159] J. Tu, A. Lin, H. Chen, Y. Li, and C. Li, "Predict the entrepreneurial intention of fresh graduate students based on an adaptive support vector machine framework," *Mathematical Problems in Engineering*, vol. 201916 pages, 2019.

[160] Y. Wei, N. Ni, D. Liu et al., "An improved grey wolf optimization strategy enhanced SVM and its application in predicting the second major," *Mathematical Problems in Engineering*, vol. 201712 pages, 2017.

[161] Y. Li, X. Liu, S. Zhang, and X. Ye, "Human articulated body recognition method in high-resolution monitoring images," *Neurocomputing*, vol. 181, pp. 116–121, 2016.

[162] Y. Li, S. Zhang, and L. Zhang, "Mining location-aware discriminative blocklets for recognizing landmark architectures," *Multimedia Systems*, vol. 22, no. 4, pp. 455–464, 2016.

[163] B. Liu, Y. Li, S. Zhang, and X. Ye, "Healthy human sitting posture estimation in RGB-D scenes using object context," *Multimedia Tools and Applications*, vol. 76, no. 8, pp. 10721–10739, 2017.

[164] C. A. Coello Coello, "Theoretical and numerical constraint-handling techniques used with evolutionary algorithms: a survey of the state of the art," *Computer Methods in Applied Mechanics and Engineering*, vol. 191, no. 11-12, pp. 1245–1287, 2002.

[165] C. A. Coello Coello and E. Mezura Montes, "Constraint-handling in genetic algorithms through the use of dominance-based tournament selection," *Advanced Engineering Informatics*, vol. 16, no. 3, pp. 193–203, 2002.

[166] J. S. Arora, "Introduction to design," *Introduction to Optimum Design*, vol. 55, pp. 1–14, 2004.

[167] A. D. Belegundu and J. S. Arora, "A study of mathematical programming methods for structural optimization. part I: theory," *International Journal for Numerical Methods in Engineering*, vol. 21, no. 9, pp. 1583–1599, 1985.

[168] Q. He and L. Wang, "An effective co-evolutionary particle swarm optimization for constrained engineering design problems," *Engineering Applications of Artificial Intelligence*, vol. 20, no. 1, pp. 89–99, 2007.

[169] C. A. Coello Coello, "Use of a self-adaptive penalty approach for engineering optimization problems," *Computers in Industry*, vol. 41, no. 2, pp. 113–127, 2000.

[170] M. Mahdavi, M. Fesanghary, and E. Damangir, "An improved harmony search algorithm for solving optimization problems," *Applied Mathematics and Computation*, vol. 188, no. 2, pp. 1567–1579, 2007.

[171] A. Kaveh and M. Khayatazad, "A new meta-heuristic method: ray optimization," *Computers & Structures*, vol. 112, no. 4, pp. 283–294, 2012.

[172] K. M. Ragsdell and D. T. Phillips, "Optimal design of a class of welded structures using geometric programming," *Journal of Engineering for Industry*, vol. 98, no. 3, pp. 1021–1025, 1976.

[173] F.-z. Huang, L. Wang, and Q. He, "An effective co-evolutionary differential evolution for constrained optimization," *Applied Mathematics and Computation*, vol. 186, no. 1, pp. 340–356, 2007.

[174] G. G. Wang, "Adaptive response surface method using inherited Latin hypercube design points," *Journal of Mechanical Design*, vol. 125, no. 2, pp. 210–220, 2003.

[175] A. H. Gandomi, X.-S. Yang, and A. H. Alavi, "Cuckoo search algorithm: a metaheuristic approach to solve structural optimization problems," *Engineering with Computers*, vol. 29, no. 1, pp. 17–35, 2013.

[176] M.-Y. Cheng and D. Prayogo, "Symbiotic organisms search: a new metaheuristic optimization algorithm," *Computers & Structures*, vol. 139, pp. 98–112, 2014.

WILEY | Hindawi

Research Article

A New Circumscribed Self-Excited Spherical Strange Attractor

Ramesh Ramamoorthy,[1] Sajjad Shaukat Jamal,[2] Iqtadar Hussain,[3] Mahtab Mehrabbeik ![ORCID],[4] Sajad Jafari,[4,5] and Karthikeyan Rajagopal ![ORCID][6]

[1]*Center for Artificial Intelligence, Chennai Institute of Technology, Chennai, India*
[2]*Department of Mathematics, College of Science, King Khalid University, Abha, Saudi Arabia*
[3]*Department of Mathematics, Statistics and Physics, Qatar University, Doha 2713, Qatar*
[4]*Biomedical Engineering Department, Amirkabir University of Technology, Tehran, Iran*
[5]*Health Technology Research Institute, Amirkabir University of Technology, Tehran, Iran*
[6]*Center for Nonlinear Systems, Chennai Institute of Technology, Chennai, India*

Correspondence should be addressed to Karthikeyan Rajagopal; rkarthiekeyan@gmail.com

Studying new chaotic flows with specific characteristics has been an open-ended field of exploring nonlinear dynamics. Investigation of chaotic flows is an area of research that has been taken into consideration for many years; thus, it helps in a better understanding of the chaotic systems. In this paper, an original chaotic 3D system, which has not been investigated yet, is presented in spherical coordinates. A unique feature of the proposed system is that its velocity becomes zero for a specific value of the radius variable. Hence, the system's attractor is expected to be stuck on one side of a plane in spherical coordinates and inside or outside a sphere in the corresponding Cartesian coordinates. It means that the attractor cannot pass through the sphere or even touch it. The introduced system owns two unstable equilibria and a self-excited strange attractor. The 1D and 2D system's bifurcation diagrams concerning the alteration of two bifurcation parameters are plotted to investigate the system's dynamical properties. Moreover, the system's Lyapunov exponents in the corresponding period of bifurcation parameters are calculated. Then, two 2D basins of attraction for two different third dimension values are explored. Based on the basin of attraction, it can be found that the sphere has attraction itself, partially, and some initial conditions are led to the sphere, not to the strange attractor. Ultimately, the connecting curves of the proposed system are explored to find an informative 1D set in addition to the system's equilibria.

1. Introduction

It has been revealed that simple, low-dimensional, and nonlinear mathematical differential equations can lead to complex and chaotic behaviors [1, 2]. Design or identification of unique special systems that can exhibit chaotic performance is one of the hottest topics in nonlinear mathematics [3–5]. Since the occurrence of chaotic behavior in the system's dynamic has always been taken into consideration, numerous investigations have been performed on particular characteristics of chaotic or nonlinear systems, and diverse systems have been introduced. In other words, some researchers have introduced multistable [6–9], megastable [10–12], extreme multistable [13–15], variable-

boostable [16, 17], memristor-based [18–20], conservative [21–23], multicluster [24], or any kinds of symmetrical systems [25–28]. For instance, the paper proposed by Bao et al. has introduced a nonautonomous 2D neural system and has also studied the multistability of the defined model [7]. The proposed model has been found to have an AC equilibrium and also two coexisting attractors, which have been considered as different neural firing activities. Another good example of multistability has been proposed by Bayani et al. [9]. They have introduced a 4D multistable system. The defined system was found to possess a plane of equilibria and also a hidden attractor. Megastability is a term first coined by Sprott et al., and it refers to the systems that include an unlimited number of countable coexisting attractors [10].

They have also investigated a cabbage-like model by forcing the 2D van der Pol system and have shown that infinite nested coexisting attractors and, in general, more complicated dynamics can be presented by forcing a simple system, such as a van der Pol oscillator. A similar term to mega-stability is extreme multistability which refers to the system with a limitless number of uncountable coexisting attractors [29]. An illustration of an extreme multistable system has been presented by Zhang et al. [14]. They have proposed a hyper-jerk system that showed an extreme multistability property. Furthermore, a list of variable-boostable systems—the domain of which can be partially controlled by a parameter—are provided by Li and Sprott [16]. Since the design of memristor-based and fractional-order systems have been interesting fields in nonlinear dynamics, Ruan et al. have presented a simple fractional-order memristor-based system [30]. Since Li et al.believed that the conservative chaotic systems are more appropriate for information security, they have proposed a conservative 3D system with 6 clusters and also a single fixed tori [22]. Moreover, some examples of different symmetrical systems have been proposed by Li et al. [27]. They have expressed how to construct a system with conditional symmetry and then have provided some systems as examples.

The study and realization of the system's equilibria's distribution play an important role in recognizing and identifying strange attractors. It used to be believed that strange attractors were associated with saddle points. However, chaos has been found in some systems with no or one stable equilibrium [31, 32]. Due to the attractiveness of this issue, different chaotic systems have been proposed to discover the secret of the strange attractor's presence in nonlinear systems. Thus, some studies have proposed systems with no equilibria [33–35], nonhyperbolic equilibria [36, 37], or stable equilibria [38, 39]. Some others include the systems with a specific configuration of equilibria such as line [40], curve [41, 42], plane [43], or surface [44]. Besides the equilibria points of a system which are zero-dimensional invariant sets, connecting curves, which are one-dimensional sets, can also provide helpful information about the trajectory of a system. Connecting curves provide more general information about the nature of flows and trajectories than local information provided by the fixed points. Connecting curves insistently pass through the fixed points. However, they are not dependent on them [45, 46].

Bifurcation diagram and Lyapunov exponent are the two primary tools for investigating the dynamics of a system [47, 48]. The bifurcation diagram of a system demonstrates the system's dynamics and its alteration in proportion to the variation of a control parameter. Lyapunov exponents of a system are the main objective and quantitative measure of the presence of chaos in a system. The number of Lyapunov exponents is based on the dimension of the system. Moreover, the largest Lyapunov exponents (LLE) value can determine the system's dynamic in specified parameters. For instance, a positive value of LLE can be evidence of chaos's existence in the system's dynamics [47].

Among other topics, one of the new-brand categories of studying the nonlinear system's dynamic is hidden attractors [49–51]. Based on the studies declared in [52–54], generally, two principal categories can be defined for the system's attractors: self-excited and hidden attractors. A self-excited attractor is a kind of attractor that possesses an unstable equilibrium within its basin of attraction. Therefore, using numerical computations, a self-excited attractor can be easily determined. It seems that the unstable equilibrium provides a mean for the self-excited attractor. In numeric solution, the trajectory is absorbed from a point near the unstable equilibrium to the oscillating attractor and traces it [55]. In contrast, the basin of attraction of a hidden attractor is equilibrium-free. Hence, hidden attractors are expected to be found in nonequilibrium systems or systems with entirely stable equilibria [56].

In the present paper, an original chaotic system with a restricted self-excited attractor is proposed using a comprehensive computational search. This system is initially defined in spherical coordinates, which is discussed in detail in Section 2. Section 3 investigates the various dynamic properties of the proposed system. The implementation of the system's connecting curves is explored in Section 4. Finally, Section 5 provides a conclusion for the paper.

1.1. The Spherical Definition of the New Chaotic System.

Lately, the exploration of chaotic systems in spherical coordinates has been an exciting topic [57–59]. The appeal of such systems is that their chaotic attractor in the Cartesian coordinates, like a captivated bird in a cage, is restricted to a sphere of radius k. In this paper, another novel bird system with the stated characteristic in the spherical coordinates is presented as follows:

$$\begin{aligned}
\dot{\rho} &= b\rho\varphi - a\rho - 10b\varphi + 10a, \\
\dot{\theta} &= \varphi^2 - c\theta\varphi, \\
\dot{\varphi} &= \theta^2 + \rho\theta - 10\theta.
\end{aligned} \tag{1}$$

Here, ρ, θ, and φ are denoted to the radial state, azimuthal state, and polar state, respectively. Also, a, b, and c are the system's parameters. According to system (1), it can be seen that when ρ variable reaches 10, the velocity of ρ variable, i.e., $\dot{\rho}$, becomes zero. In other words, as soon as the system's output reaches the $\rho = 10$ plane, it permanently remains on it. Hence, the attractor of the system, whether on the left or right side of the plane $\rho = 10$, cannot pass through the plane. In the spherical coordinates, the plane $\rho = 10$ is corresponding to a sphere of radius 10 in the Cartesian coordinates. Besides, depending on which side of the plane $\rho = 10$ of the system attractor is located in the spherical coordinates, the corresponding attractor in Cartesian coordinates is limited to inside or outside the sphere with a radius of 10. The investigation on the dynamic of system (1) revealed that this system has a strange attractor for $a = 2$, $b = 1$, and $c = 1$ using the initial condition of $(\rho_0, \theta_0, \varphi_0) = (-2, 3, 0)$. The initial condition is selected, using extensive computational search, in the left side of the plane $\rho = 10$ or inside the sphere of radius 10. So, the attractor of the system remains inside this sphere. Using the transformation $x = \rho \cos(\theta)\sin(\varphi)$, $y = \rho \sin(\theta)\sin(\varphi)$, and

$z = \rho \cos(\varphi)$, Figure 1 illustrates the three-dimensional trajectories of the proposed system in Cartesian coordinates along with its three 2D projections in x-y, x-z, and y-z planes.

According to Figure 1, it is apparent that the strange attractor of the proposed system is captivated in a sphere of radius 10.

2. Dynamic Properties

Finding the system's equilibria and analyzing their stability is the primary analysis that can be performed on a system in order to obtain a better recognition of the system. To achieve the equilibria of system (1), the velocity of each three states, i.e., $\dot{\rho}$, $\dot{\theta}$, and $\dot{\varphi}$ should be set to zero. So, it can be written that $b\rho\varphi - a\rho - 10b\varphi + 10a = 0$, $\varphi^2 - c\theta\varphi = 0$, and $\varphi^2 - c\theta\varphi = 0$. From the first equation, $\rho = 10$ or $\varphi = (a/2)$. Similarly, from the second equation, $\varphi = 0$ or $\varphi = c\theta$. Finally, from the third equation, $\theta = 0$ or $\theta = 10 - \rho$. The result of the combination of these conditions leads to two equilibria which are $(\rho_1^*, \theta_1^*, \varphi_1^*) = (10, 0, 0)$ and $(\rho_2^*, \theta_2^*, \varphi_2^*) = (10 - (a/cb), (a/cb), (a/b))$. To examine the stability of computed equilibria, the Jacobian matrix of system (1) is calculated as follows:

$$J = \begin{bmatrix} b\varphi - a & 0 & b\rho - 10b \\ 0 & -c\varphi & 2\varphi - c\theta \\ \theta & 2\theta + \rho - 10 & 0 \end{bmatrix}. \tag{2}$$

For each equilibrium of the system, the signs of the real part of the characteristic equation roots determine whether the applied equilibrium is stable or not. The characteristic equation can be obtained from

$$|\lambda I - J| = 0. \tag{3}$$

Using the Jacobian matrix and equation (3), the characteristic equation for $(\rho_1^*, \theta_1^*, \varphi_1^*) = (10, 0, 0)$ is $\lambda^3 + 2\lambda^2 = 0$. So, the first equilibrium $(\rho_1^*, \theta_1^*, \varphi_1^*)$ has two zero and one negative eigenvalues. Therefore, it is not possible to determine its stability using the analytic method. However, the numeric calculation shows that this equilibrium is unstable and settled on the sphere in Cartesian coordinates. In the same way, the characteristic equation for $(\rho_2^*, \theta_2^*, \varphi_2^*) = (10 - (a/cb), (a/cb), (a/b))$ is $\lambda^3 + 2\lambda^2 + 8 = 0$, which leads to one negative real eigenvalue $(\lambda_1 = -2.93)$ and two complex eigenvalues with positive real parts $(\lambda_{2,3} = 0.46 \pm 1.58i)$. So, the second equilibrium $(\rho_2^*, \theta_2^*, \varphi_2^*)$ is unstable as well.

The bifurcation diagram and the corresponding system's Lyapunov exponents are studied to investigate the different dynamical performances of the proposed system. Figure 2 represents the bifurcation diagram and Lyapunov exponents of system (1) corresponding to the alteration of two parameters, namely, b and c. The bifurcation diagram of the system is plotted using the Poincaré section. More specifically, the peaks or maximum values of the ρ variable are determined as the desired Poincaré section for obtaining the bifurcation diagrams. Also, the selected initial condition is considered constant for each bifurcation parameter. The Wolf algorithm [60], with a run-time of 10000, is used to obtain the system's Lyapunov exponents.
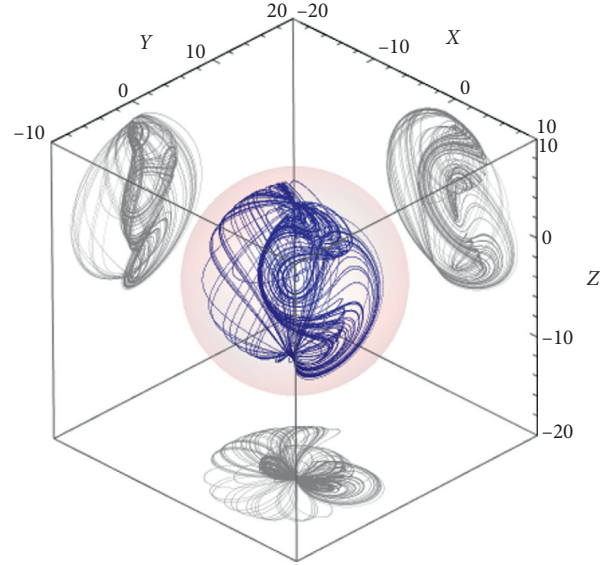
FIGURE 1: The 3D plot of the strange attractor of system (1) bounded in the sphere of radius 10 (red sphere) in the Cartesian coordinates for $a = 2$, $b = 1$, and $c = 1$ and initial condition of $(\rho_0, \theta_0, \varphi_0) = (-2, 3, 0)$. The three 2D projections in the x-y, x-z, and y-z plane are represented in gray. The system attractor is clearly bounded to a sphere of radius 10 and cannot pass through or even touch it.

Generally, considering $a = 2$ and $c = 1$, Figure 2(a) shows chaotic and periodic behaviors for $b \approx [0.7, 1.09]$ and $b \approx (1.09, 2.5]$, respectively. Figure 2(b) illustrates a positive, a negative, and one zero Lyapunov exponents for $a = 2$, $c = 1$, and $b \approx [0.7, 1.8]$ that demonstrate the chaotic performance of the system. Moreover, assuming $a = 2$ and $b = 1$, Figure 2(c) shows periodic and chaotic performances for $c \approx [0.5, 0.97)$ and $c \approx [0.97, 1.5]$, respectively. Similarly, Figure 2(d) illustrates a positive, a negative, and one zero Lyapunov exponents for $a = 2$, $b = 1$, and $c \approx [0.97, 1.5]$ that demonstrate the system's chaotic behavior. Consequently, determining $a = 2$, the introduced system shows a chaotic behavior in $b = 1$ and $c = 1$. For $a = 2$ and $c = 1$, it is noticeable that, by raising the parameter b, the system exhibits an inverse period-doubling route to chaos. On the contrary, assuming $a = 2$ and $b = 1$, a period-doubling route to chaos can be discerned in the system's dynamic by raising the parameter c. Also, Figure 2 shows both periodic dynamics and chaotic behavior.

Figure 3 illustrates two 2D bifurcation diagrams of system (1) corresponding to the variation of parameters b and c. Different bifurcation diagrams of the system can be observed for the simultaneous changes of parameter b in different values of parameter c and vice versa. Figure 3 can help to discover the system's dynamics in different parameter values at the same time.

In the study of systems with chaotic behavior, the initial conditions and the parameters' values can lead to the different behavior of the system, especially when the system is multistable. Therefore, calculating the system's basin of attraction can be an excellent method to study the sensitivity of the system's ultimate output to various initial values. So,
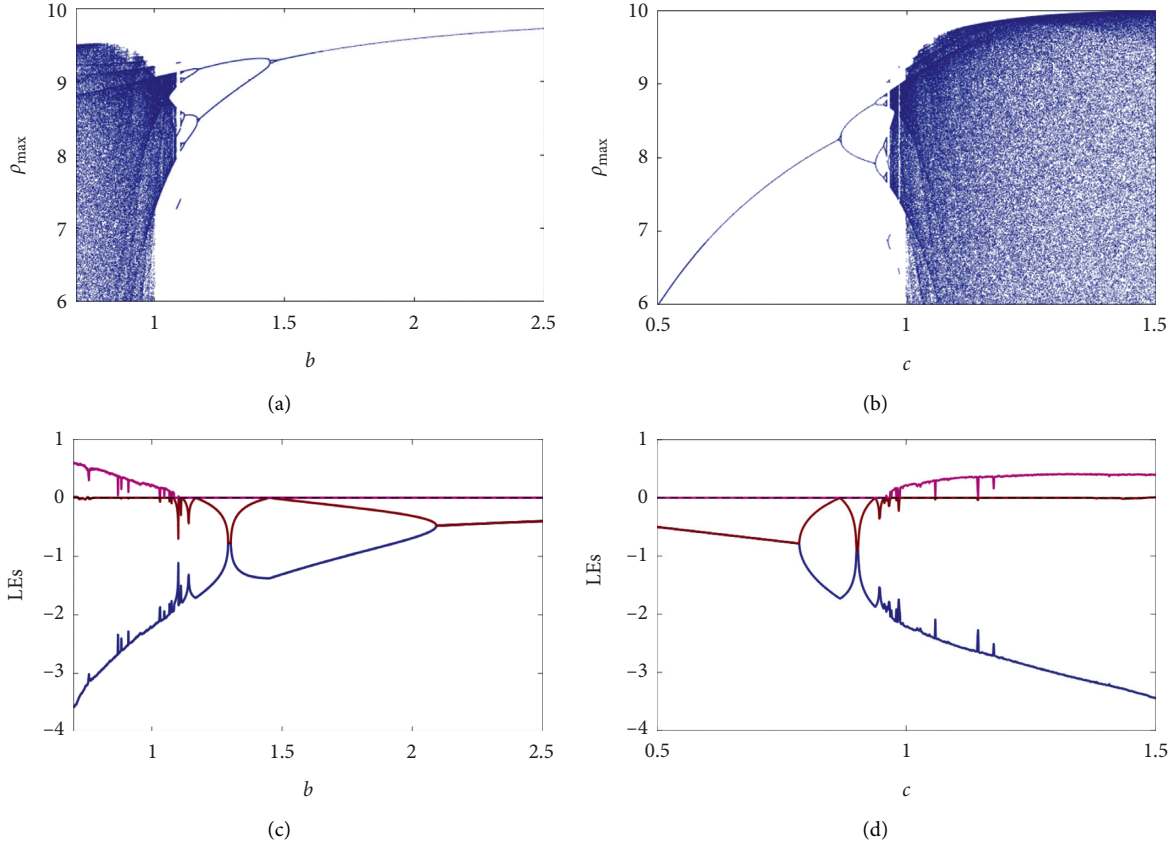
(a)

(b)

(c)

(d)

FIGURE 2: (a) The bifurcation diagram and (b) Lyapunov exponents of system (1) concerning the changes of parameter $b \in [0.7, 2.5]$. (c) The bifurcation diagram and (d) the Lyapunov exponents of system (1) concerning the changes of parameter $c \in [0.5, 1.5]$. The value of parameter a is considered to be equal to 2 with the initial condition of $(\rho_0, \theta_0, \varphi_0) = (-2, 3, 0)$. The occurrence of chaos behavior is justified based on the bifurcation diagrams and Lyapunov exponents.
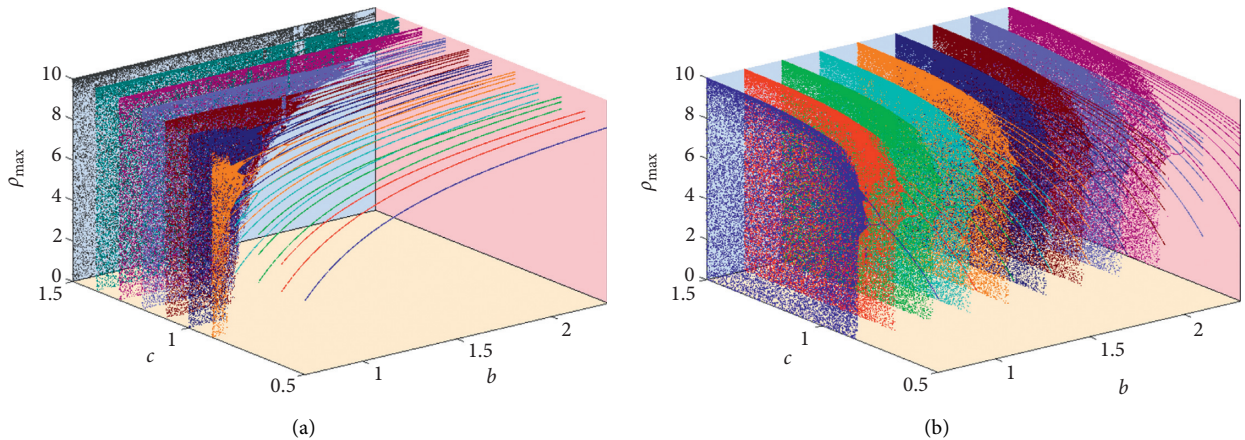

(a)

(b)

FIGURE 3: Two 3D bifurcation diagrams of system (1) concerning the changes of parameter b and c with the different horizontal resolution by assuming $a = 2$ and initial condition of $(\rho_0, \theta_0, \varphi_0) = (-2, 3, 0)$. (a) Eleven bifurcation diagrams corresponding to the variation of b parameter and eleven values of c parameter. (b) Nine bifurcation diagrams corresponding to the variation of c parameter and nine values of b parameter. Dynamic changes of the system are noticeable for simultaneous changes of b and c parameters.

the basin of attraction can help to select proper initial conditions for a system to exhibit chaos. Figure 4 shows two 2D basins of attraction of the introduced system in the ρ-θ plane with the $\varphi_1 = 2$ and $\varphi_2 = 0$. The initial value for φ variable is selected in a way that the system's equilibria can

be depicted in each basin of attraction. As represented in Figure 4(a), the second equilibrium of the system, i.e., $(\rho_2^*, \theta_2^*, \varphi_2^*) = (8, 2, 2)$, can be observed within the attractor's basin of attraction. Also, the first equilibrium $(\rho_1^*, \theta_1^*, \varphi_1^*) = (10, 0, 0)$ is located on the sphere in Figure 4(b). Since the

(a)

(b)
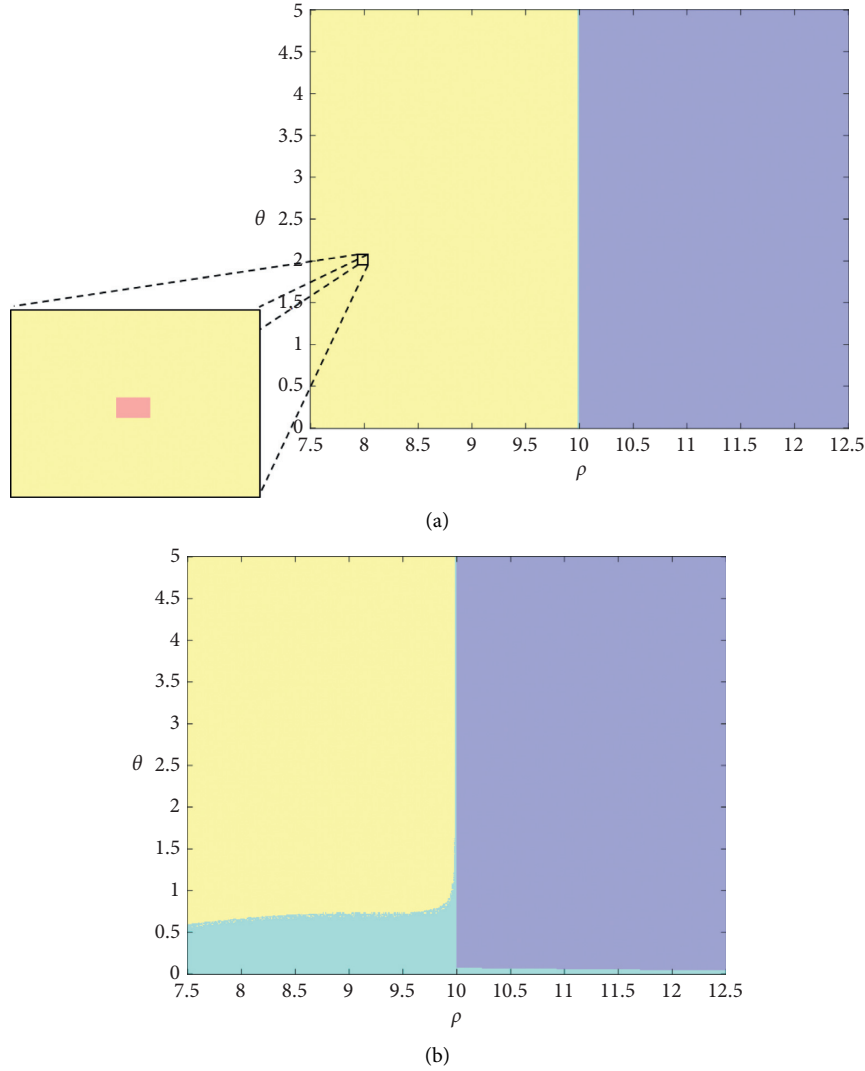
FIGURE 4: Basin of attraction of system (1) with $a = 2, b = 1$, and $c = 1$ in the ρ-θ plane with the fixed initial value of (a)$\varphi = 2$ and (b)$\varphi = 0$. All initial values of yellow color lead to the strange attractor of the system, and the purple ones lead to the unbounded orbits. The point which is shown in pink color leads to the equilibrium $(\rho_2^*, \theta_2^*, \varphi_2^*) = (8, 2, 2)$. The points represented in cyan color remain on the sphere of radius 10. Each unstable equilibria of the system can be seen in each represented basin of attraction. This helps to decide whether the attractor is self-excited or hidden.

unstable equilibrium $(\rho_2^*, \theta_2^*, \varphi_2^*) = (8, 2, 2)$ is in the chaotic basin of attraction, it can be expressed that the proposed system owns a self-excited strange attractor. Moreover, as illustrated in Figure 4, the sphere owns a basin of attraction, which means that there are some initial conditions that are attracted to the sphere, not to the strange attractor.

It is worth mentioning that the basins of attraction demonstrated in Figure 4 are obtained by identifying different system's behavior and specifying a distinctive color to each attractor. More generally, the infinite unstable behavior, which crosses a threshold, is identified in the first step. If the system behavior is constant, it will be investigated whether it is a fixed point or not. The next step is to calculate the period of the signal. If we can find a finite period for a signal, we will label the attractor as a periodic attractor. Otherwise, we will determine it as a strange

attractor. After identifying the system's attractors, the system should be run for a range of initial conditions, and the ultimate attractor they reach should be marked with a specific color of that attractor.

2.1. Connecting Curves. Vortex core curves, known as connecting curves, were first studied by Roth and Peikert [45] and then were widely investigated by Gilmore et al. [46]. Connecting curves are 1D sets that provide further information about the system's dynamics compared to equilibria, defined as 0D sets. While the fixed points provide limited information about the system's trajectory, connecting curves provide extensive information about it. In other words, fixed points only provide local information about the nature of the flows. On the contrary, connecting curves can help in obtaining more general information
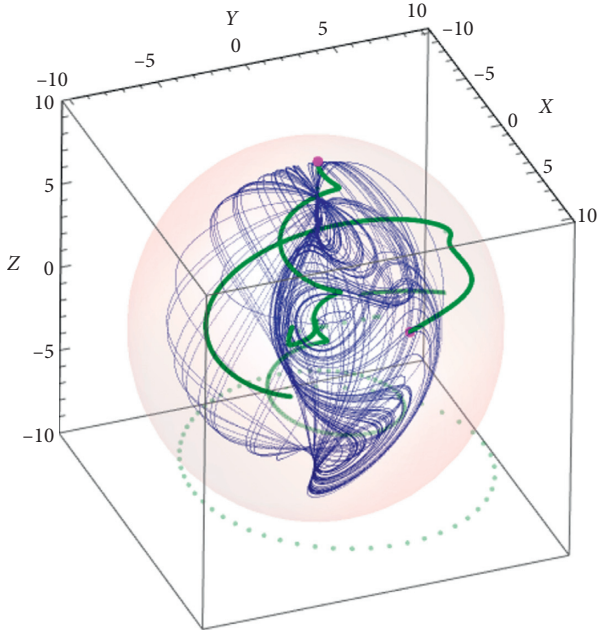
FIGURE 5: The 3D strange attractor of system (1) in Cartesian coordinates along with its connecting curves, which are shown in green, considering variable φ as the phase space coordinate. The two unstable equilibria of system (1), i.e., $(\rho_1^*, \theta_1^*, \varphi_1^*) = (10, 0, 0)$ and $(\rho_2^*, \theta_2^*, \varphi_2^*) = (8, 2, 2)$ are represented in magenta color. Connecting curves of the system connect the equilibria of the system and approximately define how trajectory changes.

about the flow's nature and the system's trajectory. So, they might be promising to identify chaotic system dynamics. According to [46], connecting curves can be obtained based on the system's dynamics and geometric theories. Based on the system's dynamics, connecting curves are the curves around which the direction of velocity and acceleration are the same. Similarly, based on geometric theories, connecting curves are zero curvatures which mean that the cross product of velocity and acceleration must be zero. Both approaches would lead to the same concept, which is connecting curves. Moreover, connecting curves should necessarily cross all the equilibria of the system; however, they are not dependent on the equilibria's existence. In fact, connecting curves connect the fixed points of a system in a meaningful way, guiding how trajectory alters. Based on the system's dynamic, which refers to the second method proposed in [46], the connecting curves of any systems can be obtained from the points satisfying the following condition:

$$J\overrightarrow{V} - \lambda\overrightarrow{V} = 0. \tag{4}$$

Here, $\overrightarrow{V}$ denotes the velocity vector consisting of the velocity of each phase space variable. Also, J and λ refer to the system's Jacobian matrix and its eigenvalues, respectively. For an nD system, using equation (4), n equations can be obtained with $n + 1$ variables: phase space variables plus eigenvalue λ. 1D set can be obtained by considering a primary phase space variable and

obtaining other variables in terms of the selected primary variable and λ using n equations.

In order to implement the connecting curves of system (1), first, three main equations with four variables, namely, ρ, θ, φ, and λ, are obtained using equation (4). Then, considering the variable φ as the primary phase space variable, two other variables, i.e., ρ and θ can be written down in terms of φ and λ: $\rho(\varphi, \lambda)$ and $\theta(\varphi, \lambda)$. Next, λ is written down in terms of φ: $\lambda(\varphi)$. The solution of $\lambda(\varphi) = 0$ leads to 5 roots for each value of φ. Obtaining the real eigenvalues for each value of φ, other variables can be easily calculated, and the connecting curves of the system can be finally plotted. The implementation of connecting curves for system (1) in Cartesian coordinates is illustrated in Figure 5. According to Figure 5, it can be seen that the connecting curves pass through the two unstable equilibria of the system, i.e., $(\rho_1^*, \theta_1^*, \varphi_1^*) = (10, 0, 0)$ and $(\rho_2^*, \theta_2^*, \varphi_2^*) = (8, 2, 2)$. Since connecting curves are calculated based on the system's dynamics, they can have a nonuniform resolution. As a result, The separate points in Figure 5 are also connecting curves of the proposed system.

3. Conclusion

In this paper, a new chaotic system defined in the spherical coordinates was presented. The dynamic properties of the proposed system were investigated using the 1D and 2D bifurcation diagrams and also the Lyapunov exponents. Both bifurcation diagrams and Lyapunov exponents confirmed the existence of chaos in the introduced system. Moreover, the inverse period-doubling route to chaos and period-doubling route to the chaos was observed in the system's bifurcation for some parameters' values. The initial condition for plotting the system's attractor, bifurcation diagrams, and Lyapunov exponents was considered the same and was obtained using a comprehensive search. Furthermore, the initial condition was considered constant for each bifurcation parameter to plot the system's bifurcation diagrams. It was found that the proposed system owns two equilibria. Stability analysis of the system's equilibria demonstrated that both system's equilibria are unstable. Besides, investigation of the system's basin of attraction specified the regions where the initial values led to the strange attractor or the sphere. In order to investigate whether the strange attractor is hidden or not, two basins of attraction with the initial φ values equal to the φ values of the system's equilibria were plotted. It turned out that the introduced system owns a self-excited strange attractor, which is captivated in an insurmountable sphere since one unstable equilibrium was observed in the basin of attraction of the strange attractor. So, when the system solution touches the sphere, it remains on it. Ultimately, the connecting curves of the proposed system were implemented using a parameterized method to provide general information about the system's trajectory. Generally, investigating a new chaotic system with a typical feature helps to understand chaos better and define systems that can lead to this comprehension. The proposed system can be used in some applications, such as image encryption or generating random numbers in future works.

Data Availability

The data used to support the findings of the study are available within the article.

Conflicts of Interest

The authors declare that they have no conflicts of interest.

Acknowledgments

References

[1] J. Kengne, A. N. Negou, and D. Tchiotsop, "Antimonotonicity, chaos and multiple attractors in a novel autonomous memristor-based jerk circuit," *Nonlinear Dynamics*, vol. 88, no. 4, pp. 2589–2608, 2017.

[2] J. C. Sprott, "Some simple chaotic flows," *Physical Review E*, vol. 50, no. 2, pp. R647–R650, 1994.

[3] D. Ghosh, A. R. Chowdhury, and P. Saha, "Multiple delay Rössler system-Bifurcation and chaos control," *Chaos, Solitons & Fractals*, vol. 35, no. 3, pp. 472–485, 2008.

[4] M. Sayeed Anwar, G. K. Sar, A. Ray, and D. Ghosh, "Behavioral study of a new chaotic system," *The European Physical Journal Special Topics*, vol. 229, no. 6-7, pp. 1343–1350, 2020.

[5] A. Ray and D. Ghosh, "Another new chaotic system: bifurcation and chaos control," *International Journal of Bifurcation and Chaos*, vol. 30, no. 11, Article ID 2050161, 2020.

[6] H. Bao, Z. Hua, N. Wang, L. Zhu, M. Chen, and B. Bao, "Initials-boosted coexisting chaos in a 2-D sine map and its hardware implementation," *IEEE Transactions on Industrial Informatics*, vol. 17, no. 2, pp. 1132–1140, 2020.

[7] B. Bao, Y. Zhu, C. Li, H. Bao, and Q. Xu, "Global multistability and analog circuit implementation of an adapting synapse-based neuron model," *Nonlinear Dynamics*, vol. 101, no. 2, pp. 1105–1118, 2020.

[8] A. Ray, D. Ghosh, and A. R. Chowdhury, "Topological study of multiple coexisting attractors in a nonlinear system," *Journal of Physics A: Mathematical and Theoretical*, vol. 42, no. 38, Article ID 385102, 2009.

[9] A. Bayani, K. Rajagopal, A. J. M. Khalaf, S. Jafari, G. D. Leutcho, and J. Kengne, "Dynamical analysis of a new multistable chaotic system with hidden attractor: antimonotonicity, coexisting multiple attractors, and offset boosting," *Physics Letters A*, vol. 383, no. 13, pp. 1450–1456, 2019.

[10] J. C. Sprott, S. Jafari, A. J. M. Khalaf, and T. Kapitaniak, "Megastability: coexistence of a countable infinity of nested attractors in a periodically-forced oscillator with spatially-periodic damping," *The European Physical Journal Special Topics*, vol. 226, no. 9, pp. 1979–1985, 2017.

[11] G. D. Leutcho, A. J. M. Khalaf, Z. Njitacke Tabekoueng et al., "A new oscillator with mega-stability and its Hamilton energy: infinite coexisting hidden and self-excited attractors," *Chaos: An Interdisciplinary Journal of Nonlinear Science*, vol. 30, no. 3, Article ID 033112, 2020.

[12] G. D. Leutcho, S. Jafari, I. I. Hamarash, J. Kengne, Z. Tabekoueng Njitacke, and I. Hussain, "A new megastable nonlinear oscillator with infinite attractors," *Chaos, Solitons & Fractals*, vol. 134, Article ID 109703, 2020.

[13] Y. Zhang, Z. Liu, H. Wu, S. Chen, and B. Bao, "Two-memristor-based chaotic system and its extreme multistability reconstitution via dimensionality reduction analysis," *Chaos, Solitons & Fractals*, vol. 127, pp. 354–363, 2019.

[14] Y. Zhang, Z. Liu, H. Wu, S. Chen, and B. Bao, "Extreme multistability in memristive hyper-jerk system and stability mechanism analysis using dimensionality reduction model," *The European Physical Journal Special Topics*, vol. 228, no. 10, pp. 1995–2009, 2019.

[15] H. Li, H. Bao, L. Zhu, B. Bao, and M. Chen, "Extreme multistability in simple area-preserving map," *IEEE Access*, vol. 8, pp. 175972–175980, 2020.

[16] C. Li and J. C. Sprott, "Variable-boostable chaotic flows," *Optik*, vol. 127, no. 22, pp. 10389–10398, 2016.

[17] V.-T. Pham, A. Akgul, C. Volos, S. Jafari, and T. Kapitaniak, "Dynamics and circuit realization of a no-equilibrium chaotic system with a boostable variable," *AEU - International Journal of Electronics and Communications*, vol. 78, pp. 134–140, 2017.

[18] R. Zhang, A. Wu, S. Zhang, Z. Wang, and S. Cang, "Dynamical analysis and circuit implementation of a DC/DC single-stage boost converter with memristance load," *Nonlinear Dynamics*, vol. 93, no. 3, pp. 1741–1755, 2018.

[19] H. Bao, Y. Zhang, W. Liu, and B. Bao, "Memristor synapse-coupled memristive neuron network: synchronization transition and occurrence of chimera," *Nonlinear Dynamics*, vol. 100, no. 1, pp. 937–950, 2020.

[20] M. Chen, M. Sun, H. Bao, Y. Hu, and B. Bao, "Flux–charge analysis of two-memristor-based chua's circuit: dimensionality decreasing model for detecting extreme multistability," *IEEE Transactions on Industrial Electronics*, vol. 67, no. 3, pp. 2197–2206, 2019.

[21] S. Cang, Z. Kang, and Z. Wang, "Pseudo-random number generator based on a generalized conservative Sprott-A system," *Nonlinear Dynamics*, vol. 104, no. 1, pp. 827–844, 2021.

[22] Y. Li, S. Cang, Z. Kang, and Z. Wang, "A new conservative system with isolated invariant tori and six-cluster chaotic flows," *The European Physical Journal Special Topics*, vol. 229, no. 6-7, pp. 1335–1342, 2020.

[23] S. Cang, Y. Li, W. Xue, Z. Wang, and Z. Chen, "Conservative chaos and invariant tori in the modified Sprott A system," *Nonlinear Dynamics*, vol. 99, no. 2, pp. 1699–1708, 2020.

[24] S. Cang, Y. Li, Z. Kang, and Z. Wang, "Generating multi-cluster conservative chaotic flows from a generalized Sprott-A system," *Chaos, Solitons & Fractals*, vol. 133, Article ID 109651, 2020.

[25] C. Li, J. C. Sprott, Y. Liu, Z. Gu, and J. Zhang, "Offset boosting for breeding conditional symmetry," *International Journal of Bifurcation and Chaos*, vol. 28, no. 14, Article ID 1850163, 2018.

[26] C. Li, Y. Xu, G. Chen, Y. Liu, and J. Zheng, "Conditional symmetry: bond for attractor growing," *Nonlinear Dynamics*, vol. 95, no. 2, pp. 1245–1256, 2019.

[27] C. Li, J. C. Sprott, and H. Xing, "Constructing chaotic systems with conditional symmetry," *Nonlinear Dynamics*, vol. 87, no. 2, pp. 1351–1358, 2017.

[28] G. D. Leutcho and J. Kengne, "A unique chaotic snap system with a smoothly adjustable symmetry and nonlinearity: chaos, offset-boosting, antimonotonicity, and coexisting multiple attractors," *Chaos, Solitons & Fractals*, vol. 113, pp. 275–293, 2018.

[29] V.-T. Pham, S. Vaidyanathan, and T. Kapitaniak, "Complexity, dynamics, control, and applications of nonlinear systems with multistability," *Complexity*, vol. 2020, Article ID 8510930, 2020.

[30] J. Ruan, K. Sun, J. Mou, S. He, and L. Zhang, "Fractional-order simplest memristor-based chaotic circuit with new derivative," *The European Physical Journal Plus*, vol. 133, no. 1, p. 3, 2018.

[31] S. Jafari, J. C. Sprott, and S. M. R. Hashemi Golpayegani, "Elementary quadratic chaotic flows with no equilibria," *Physics Letters A*, vol. 377, no. 9, pp. 699–702, 2013.

[32] M. Molaie, S. Jafari, J. C. Sprott, and S. M. R. H. Golpayegani, "Simple chaotic flows with one stable equilibrium," *International Journal of Bifurcation and Chaos*, vol. 23, no. 11, Article ID 1350188, 2013.

[33] S. Ren, S. Panahi, K. Rajagopal, A. Akgul, V.-T. Pham, and S. Jafari, "A new chaotic flow with hidden attractor: the first hyperjerk system with No equilibrium," *Zeitschrift für Naturforschung A*, vol. 73, no. 3, pp. 239–249, 2018.

[34] C. Wang, C. Hu, J. Han, and S. Cang, "A new no-equilibrium chaotic system and its topological horseshoe chaos," *Advances in Mathematical Physics*, vol. 2016, Article ID 3142068, 6 pages, 2016.

[35] S. Nag Chowdhury and D. Ghosh, "Hidden attractors: a new chaotic system without equilibria," *The European Physical Journal Special Topics*, vol. 229, no. 6-7, pp. 1299–1308, 2020.

[36] Z. Wei, J. C. Sprott, and H. Chen, "Elementary quadratic chaotic flows with a single non-hyperbolic equilibrium," *Physics Letters A*, vol. 379, no. 37, pp. 2184–2187, 2015.

[37] C.-L. Li and J.-B. Xiong, "A simple chaotic system with non-hyperbolic equilibria," *Optik*, vol. 128, pp. 42–49, 2017.

[38] X. Wang and G. Chen, "A chaotic system with only one stable equilibrium," *Communications in Nonlinear Science and Numerical Simulation*, vol. 17, no. 3, pp. 1264–1272, 2012.

[39] V.-T. Pham, S. Jafari, T. Kapitaniak, C. Volos, and S. T. Kingni, "Generating a chaotic system with one stable equilibrium," *International Journal of Bifurcation and Chaos*, vol. 27, no. 4, Article ID 1750053, 2017.

[40] S. Jafari and J. C. Sprott, "Simple chaotic flows with a line equilibrium," *Chaos, Solitons & Fractals*, vol. 57, pp. 79–84, 2013.

[41] T. Gotthans and J. Petržela, "New class of chaotic systems with circular equilibrium," *Nonlinear Dynamics*, vol. 81, no. 3, pp. 1143–1149, 2015.

[42] S. Panahi, Z. Aram, S. Jafari, V.-T. Pham, C. Volos, and K. Rajagopal, "A new transiently chaotic flow with ellipsoid equilibria," *Pramana*, vol. 90, no. 3, p. 31, 2018.

[43] S. Jafari, J. C. Sprott, and M. Molaie, "A simple chaotic flow with a plane of equilibria," *International Journal of Bifurcation and Chaos*, vol. 26, no. 6, Article ID 1650098, 2016.

[44] S. Jafari, J. C. Sprott, V.-T. Pham, C. Volos, and C. Li, "Simple chaotic 3D flows with surfaces of equilibria," *Nonlinear Dynamics*, vol. 86, no. 2, pp. 1349–1358, 2016.

[45] M. Roth and R. Peikert, "A higher-order method for finding vortex core lines," in *Proceedings Visualization'98 (Cat. No. 98CB36276)*, pp. 143–150, IEEE, Research Triangle Park, NC, USA, October 1998.

[46] R. Gilmore, J.-M. Ginoux, T. Jones, C. Letellier, and U. S. Freitas, "Connecting curves for dynamical systems," *Journal of Physics A: Mathematical and Theoretical*, vol. 43, no. 25, Article ID 255101, 2010.

[47] J. C. Sprott, *Elegant Chaos: Algebraically Simple Chaotic Flows*, World Scientific, Singapore, 2010.

[48] Z. Wei, V.-T. Pham, T. Kapitaniak, and Z. Wang, "Bifurcation analysis and circuit realization for multiple-delayed Wang-Chen system with hidden chaotic attractors," *Nonlinear Dynamics*, vol. 85, no. 3, pp. 1635–1650, 2016.

[49] S. Jafari and J. C. Sprott, "Simple chaotic flows with a line equilibrium," *Chaos, Solitons & Fractals*, vol. 57, pp. 341-342, 2015.

[50] S. Cang, Y. Li, R. Zhang, and Z. Wang, "Hidden and self-excited coexisting attractors in a Lorenz-like system with two equilibrium points," *Nonlinear Dynamics*, vol. 95, no. 1, pp. 381–390, 2019.

[51] M. Chen, C. Wang, H. Bao, X. Ren, B. Bao, and Q. Xu, "Reconstitution for interpreting hidden dynamics with stable equilibrium point," *Chaos, Solitons & Fractals*, vol. 140, Article ID 110188, 2020.

[52] M.-F. Danca, N. V. Kuznetsov, and G. Chen, "Approximating hidden chaotic attractors via parameter switching," *Chaos: An Interdisciplinary Journal of Nonlinear Science*, vol. 28, no. 1, Article ID 013127, 2018.

[53] M.-F. Danca, P. Bourke, and N. Kuznetsov, "Graphical structure of attraction basins of hidden chaotic attractors: the Rabinovich-Fabrikant system," *International Journal of Bifurcation and Chaos*, vol. 29, no. 1, Article ID 1930001, 2019.

[54] M.-F. Danca and M. Fečkan, "Hidden chaotic attractors and chaos suppression in an impulsive discrete economical supply and demand dynamical system," *Communications in Nonlinear Science and Numerical Simulation*, vol. 74, pp. 1–13, 2019.

[55] G. A. Leonov, N. V. Kuznetsov, and T. N. Mokaev, "Homoclinic orbits, and self-excited and hidden attractors in a Lorenz-like system describing convective fluid motion," *The European Physical Journal Special Topics*, vol. 224, no. 8, pp. 1421–1458, 2015, in English.

[56] N. V. Kuznetsov and G. A. Leonov, "Hidden attractors in dynamical systems: systems with no equilibria, multistability and coexisting attractors," *IFAC Proceedings Volumes*, vol. 47, no. 3, pp. 5445–5454, 2014.

[57] S. Jafari, S. Dehghan, G. Chen, S. T. Kingni, and K. Rajagopal, "Twin birds inside and outside the cage," *Chaos, Solitons & Fractals*, vol. 112, pp. 135–140, 2018.

[58] F. Nazarimehr, V.-T. Pham, K. Rajagopal, F. E. Alsaadi, T. Hayat, and S. Jafari, "A new imprisoned strange attractor," *International Journal of Bifurcation and Chaos*, vol. 29, no. 13, Article ID 1950181, 2019.

[59] L. Chen, E. Tlelo-Cuautle, I. I. Hamarash, V.-T. Pham, and H. R. Abdolmohammadi, "A novel chaotic system in the spherical coordinates," *The European Physical Journal Special Topics*, vol. 229, no. 6-7, pp. 1257–1263, 2020.

[60] A. Wolf, J. B. Swift, H. L. Swinney, and J. A. Vastano, "Determining Lyapunov exponents from a time series," *Physica D: Nonlinear Phenomena*, vol. 16, no. 3, pp. 285–317, 1985.

WILEY | Hindawi

Research Article

Dynamic Analysis and Degenerate Hopf Bifurcation-Based Feedback Control of a Conservative Chaotic System and Its Circuit Simulation

Xiaojuan Zhang, **Mingshu Chen**, **Yang Wang**, **Huaigu Tian**, and **Zhen Wang**

Shaanxi International Joint Research Center for Applied Technology of Controllable Neutron Source School of Science, Xijing University, Xi'an 710123, China

Correspondence should be addressed to Zhen Wang; williamchristian@163.com

A novel conservative chaotic system with no equilibrium is investigated in this study. Various dynamics such as the conservativeness, coexistence, symmetry, and invariance are presented. Furthermore, a partial-state feedback control scheme is proposed, and the stable domain of control parameters is analyzed based on the degenerate Hopf bifurcation. In order to verify the numerical simulation analysis, an analog circuit is designed. The simulation results show that the output of the analog circuit system can reproduce the numerical simulation results and verify the correctness of the theoretical analysis.

1. Introduction

Since Lorenz first found the chaotic attractor in the quadratic polynomial ODEs in 1963 [1], many typical chaotic attractors including Rössler attractor [2], Chen and Ueta attractor [3], and Lü attractor [4] were discovered in many nonlinear systems [5,6] in the following decades. However, the attractors of most of them are Shilnikov type, and the corresponding systems have saddle-foci equilibria [7]. In 2011, Leonov first discovered the hidden attractors in Chua's chaotic circuit [8]; unlike the Shilnikov-type attractors, these hidden attractors are with a basin of attraction which does not contain neighborhoods of equilibria and cannot be determinated by the Shilnikov condition. In the last decade, the systems with hidden attractors mainly include chaotic systems without equilibrium [9], with infinite equilibrium [10, 11], and with only one stable equilibrium [12–17]. Although many chaotic systems with hidden attractors have been proposed, most of them are mainly studied by numerical simulation, and the main dynamic behaviors studies are focused on the local structures, while the studies on the global dynamics are relatively rare; hence, it is necessary to study the global dynamics and bifurcation of chaotic systems with hidden attractors to reveal the mechanism of chaos.

In recent years, in the field of hidden attractors, many researchers have paid attention to the coexisting hidden attractors which have more complex hidden characteristics than the ordinary hidden attractors. A modified Chua's circuit is implemented using a 5-segment piecewise-linear Chua's diode, and the coexistence of hidden attractors with other three attractors is presented [18]. In 2018, V.T. Pham and his coauthors presented a simple fractional-order 3D chaotic system without equilibrium and explored the coexistence of various attractors [19]. Li [20] constructed a 4D simplified Lorenz system which can generate a variety of coexisting hidden attractors, including the symmetric hidden attractors and the hyperchaotic attractors. It should be noted that most of the above systems are dissipative, so how to construct a conservative system with hidden attractors has become a hot issue in chaos theory. Moreover, according to Liouville's theorem, for these conservative dynamical systems, the volume of phase space is conservative and the flow is incompressible. Allan and Michael constructed a system with coexisting quasiperiodic and coexisting chaotic flows in

2013 [21]. 3D/4D conservative chaotic systems were constructed by Cang [22, 23]; meanwhile, the dynamics and conservative flows were also researched. Furthermore, conservative chaotic mapping has been revealed in [24, 25].

In addition, there are coexisting chaotic flows in conservative chaotic systems, which may be chaotic flows coexisting with torus [26] or one or more limit cycles [27–31] and so on. What causes the coexisting chaotic flows in chaotic systems? While some are caused by offset boosting, Li explored a new regime of chaotic flow, in which one of the variables has the freedom of offset boosting, and a different symmetry was obtained by using a new boosting controller, thereby retaining any existing multistability [32]. Some of them are caused by the symmetry of conditions, different initial values will produce different chaotic flows, and the conditional symmetry may also produce coexisting symmetric chaotic flows [33, 34]. Some are from the structure of hypogenetic Jerk [35]. Such nonequilibrium conservative chaotic systems with coexisting symmetric chaotic flows are very important in engineering applications and may have problems, so it is necessary to study the types and characteristics of their coexisting chaotic flows. Based on the complex characteristics, the conservative coexisting chaotic flows have been applied to many engineering systems, such as tank circuit, chaotic communication, image, video and audio encryption [36], control system, and pseudorandom number generator [37].

On the other hand, the Hopf bifurcation of nonlinear dynamical systems has attracted more and more attention, which is the critical point of stability switching and periodic solution of a system. In order to eliminate saddle node bifurcation or reduce the generated amplitude, it is necessary to design a reasonable nonlinear controller, in which earliest can be traced back that Abed studied the control of Hopf bifurcation [38]. Subsequently, a general explicit formula is derived [39]; this method does not increase the size of the system and can be used to delay (determine) existing forks or change the stability of the fork solution. Ding proposed a time-delayed feedback controller in order to control the fractional-order memristor based chaotic system with time-delay [40]. Now, the work of bifurcation control involves the engineering fields such as aviation [41], electrical machinery [42], and bioengineering [43]. The main feature of conservative systems is that they have chaotic flow instead of the attractor, which means that these systems have complex dynamic characteristics. Thus, it is necessary to analyze the chaotic dynamics of conservative systems. Motivated by this, a new conservative chaotic system with no equilibrium is introduced, and the dynamic characteristics of this new system are analyzed in detail. A feedback control scheme based on the degenerate Hopf bifurcation method is proposed. Finally, the simulation results are illustrated by using the analog circuit.

The main contributions of this study lie in the following aspects:

(1) A novel conservative chaotic system with no equilibrium is investigated. Since the investigated system does not have equilibrium, it is very challenging to analyze its dynamics. We analyzed the conservativeness, coexistence, symmetry, and invariance.

(2) A new partial-state feedback control by using one-dimensional state for the investigated conservative chaotic system is proposed. Compared with the full-state feedback control methods, the proposed scheme is required to measure less states and provides a simpler controller structure. Thus, the proposed partial-state feedback control scheme can be easily applied in the practical engineering. Furthermore, degenerate Hopf bifurcation was analyzed to illustrate the parametric stability range of the state feedback control system.

The structure of this study is as follows: in Section 2, the conservative chaotic system and the dynamics analysis are presented, including the conservativeness, the symmetry and invariance, and coexisting chaotic behaviors. In Section 3, a partial-state feedback control for the investigated system is proposed, and the stable domain of control parameters is analyzed based on the degenerate Hopf bifurcation method. In Section 4, the numerical simulation results are illustrated by using the analog circuit. Finally, the conclusion is presented in Section 5.

2. Dynamics Analysis

The new conservative chaotic system is given as follows:

$$\begin{aligned}
\dot{x} &= y, \\
\dot{y} &= -x - yz, \\
\dot{z} &= a - bx^2 + cy^2.
\end{aligned} \tag{1}$$

Let $\dot{x} = 0$, $\dot{y} = 0$, $\dot{z} = 0$, system (1) has a line equilibrium $(0, 0, z)$ when $a = 0$ or with no equilibrium when $a \neq 0$. In order to further study the dynamics of system (1), the numerical simulation analysis will be carried out in the following subsections.

*2.1. Conservativeness.* The conservativeness of system (1) can be testified by the divergence

$$\nabla V = \frac{\partial \dot{x}}{\partial x} + \frac{\partial \dot{y}}{\partial y} + \frac{\partial \dot{z}}{\partial z} = -z(t). \tag{2}$$

Obviously, the conservativeness is not obvious since the dissipation is given by the time-averaged value of $-z(t)$ along the trajectory. Following the definition, the average value of a variable $s(t)$ is given by $\bar{s}(t) = \lim_{t \to \infty} (\int_{t_0}^{t} s(t)dt/t - t_0)$, and the average of $z(t)$ of system (1) with special parameters (from Table 1, we can see that system (1) is chaotic for these parameters.) is shown in Figure 1. It can be seen that the average values of $z(t)$ for system (1) will be zero.

In fact, when $b = 0, c = 1$, system (1) is a special case of the Nose–Hoover oscillator [44], which is invariant to the transformation $t \longrightarrow -t$. Furthermore, we can provide a positive definite energy function which has a quadratic form

TABLE 1: Motion states of system (1) for different values of the parameters a, b under $c = 1$ with initial value $(0, 5, 0)$.

Parameter	Lyapunov exponents	Lyapunov dimension	Motion states	Phase portrait
$a = -5, b = 0$	$(0.003, 0, -0.003)$	3	Rotationally symmetric chaotic flow	Figure 2(a)
$a = -4, b = 0$	$(0.003, 0, -0.003)$	3	Rotationally symmetric chaotic flow	Figure 2(b)
$a = -0.8, b = 0$	$(0.013, 0, -0.013)$	3	Symmetric pair of chaotic flow	Figure 2(c)
$a = -0.5, b = 0$	$(0.003, 0, -0.003)$	3	Rotationally symmetric chaotic flow	Figure 2(d)
$a = -0.2, b = 0$	$(0.004, 0, -0.004)$	3	Symmetric pair of chaotic flow	Figure 2(e)
$a = -0.15, b = 0$	$(0.003, 0, -0.003)$	3	Symmetric pair of chaotic flow	Figure 2(f)
$a = -6.17, b = -1$	$(0.004, 0, -0.005)$	2.8	Rotationally symmetric chaotic flow	Figure 2(g)
$a = -4.5, b = -1$	$(0, -0.37, -0.95)$	1	Symmetric limit cycle	Figure 2(h)
$a = -0.8, b = -1$	$(0, -0.01, -26.94)$	1	Symmetric pair of limit cycles	Figure 2(i)
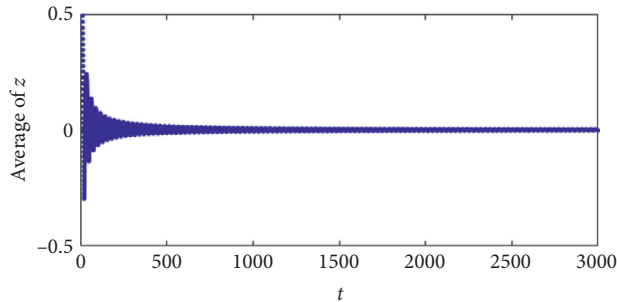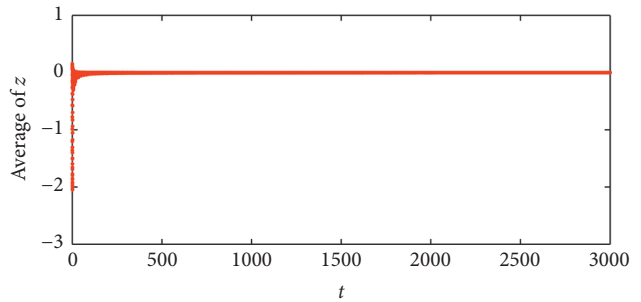
FIGURE 1: Time-averaged value of $z(t)$ for system (1) with different parameters a, b, c. (a) $a = 0.2$, $b = 0$, $c = 1$. (b) $a = -4$, $b = 0$, $c = 1$.

$$H = \frac{1}{2}\left(x^2 + y^2 + z^2\right). \tag{3}$$

Taking the time derivative of H, we have

$$\dot{H} = x\dot{x} + y\dot{y} + z\dot{z} = az. \tag{4}$$

If the average of z is zero, we know that the energy of system (1) is invariable. Therefore, the system has a conservative nature (Table 1).

2.2. Symmetry and Invariance.

It is obviously that system (1) is invariant under the transformation $(x, y, z) \longrightarrow (-x, -y, z)$, i.e., system (1) is symmetrical about the coordinate axis z. Interestingly, it is time reversible with LEs that are symmetric about zero for $b = 0$ (Table 1).

When the initial value is $(0, 5, 0)$, the parameter c is fixed and the parameters a and b are changed, and the phase diagrams with different parameters are shown in Figure 2 and summarized in Table 1. It can be seen from Figure 2 that when the Lyapunov dimension is 3, there are chaotic motions, but there are no obvious chaotic attractors.

From Table 1, when the Lyapunov dimension equals the system dimension and the sum of finite-time local Lyapunov exponents is approximately zero, system (1) has a conservative solution (Figures 2(a)–2(f)). In addition, system (1) also has symmetric limit cycles (Figures 2(h)–2(i)). Moreover, when the values of parameters are changed, the classic butterfly attractor is broken into a symmetric pair of strange attractors, or shrinks into a small attractor basin, which is intertwined with a pair of symmetrical limit cycle basins, resulting in symmetry broken

[45, 46]. Under the different initial values $(0, 5, 0)$ and $(0, -5, 0)$, when $a = -0.8, b = 0, c = 1$, we can find coexistence of symmetric pair of chaotic flow as shown in Figure 2(c). The two chaotic domains are represented by red and light blue, respectively. Similarly, in Figure 2(e), $a = -0.2$, and it shows a typical symmetric pair of chaotic flow in the region, where a is relatively small. As a increases, a new pair of nearly touching chaotic flows appears, as in Figure 2(f) ($a = -0.15$).

2.3. Coexistence.

From Section 2.2, we can see that system (1) has some chaotic flows. Moreover, since the sum of Lyapunov exponents is approximately zero for system (1) with special parameters, the conservative solution and chaotic flows will coexist in this system (Figure 3(a), chaotic flow coexists a torus). Indeed, there is a limit cycle for some initial points from $a - bx^2 + cy^2 = 0, z = 0$ under $a < 0$, $-b = c = 1$. Following these conditions, if an initial point starts from a limit cycle $x^2 + y^2 = -a, z = 0$, we have $\dot{z} = 0$, and the variable z will be fixed. Hence, when $z \equiv 0$, system (1) will become

$$\begin{aligned} \dot{x} &= y, \\ \dot{y} &= -x. \end{aligned} \tag{5}$$

The system (5) is a Hamiltonian system (conservative system). All orbits starting from $x^2 + y^2 = -a$ will stay in this circle. So we claim that system (1) will have a limit cycle (green cycle shown in Figures 3(b)–3(d)) which coexists with other attractors (including chaotic flow) under the condition of $a < 0$, $-b = c = 1$.
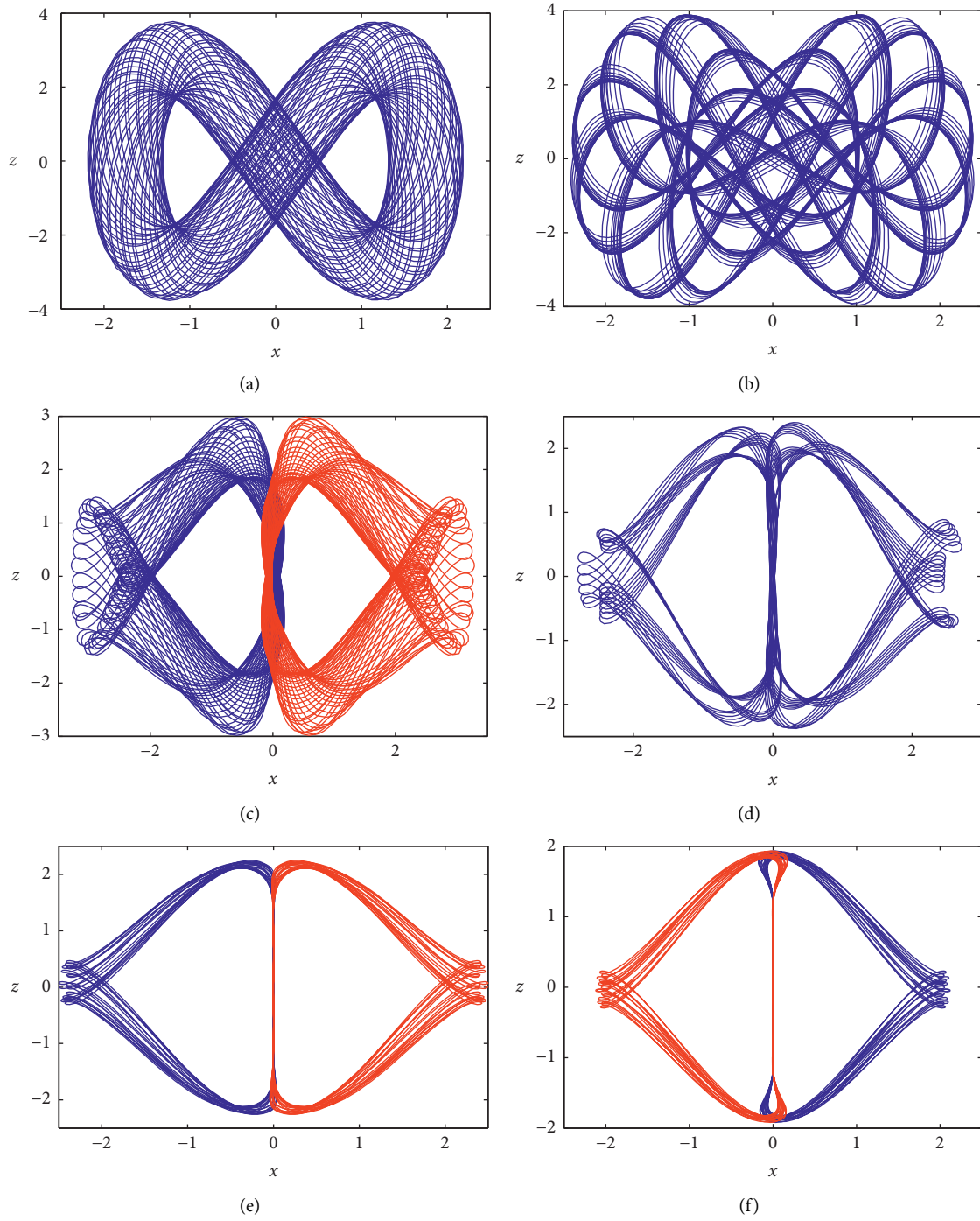
(a)

(b)

(c)

(d)

(e)

(f)

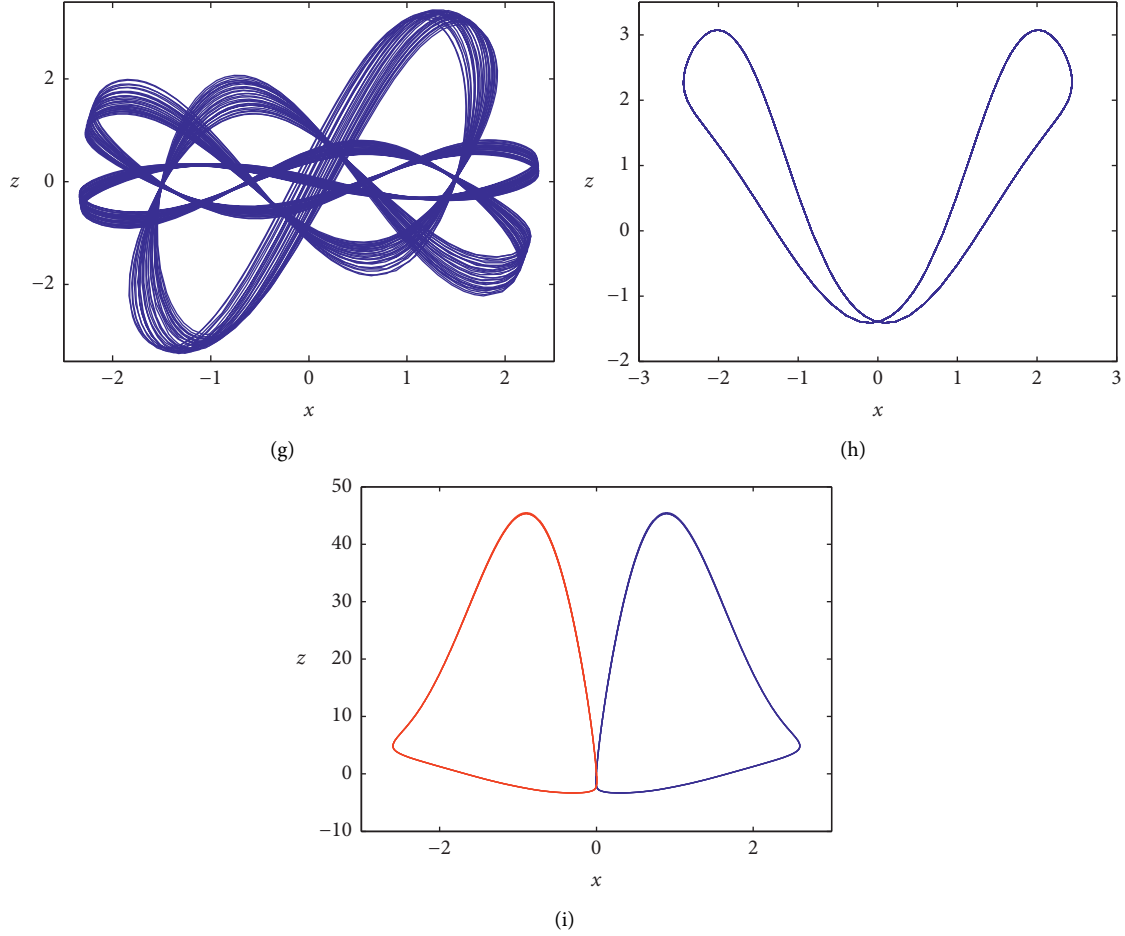Figure 2: Continued.

(g)

(h)

(i)

FIGURE 2: Chaotic flows from system (1) at various values of a and b. (a) $a = -5$, $b = 0$. (b) $a = -4$, $b = 0$. (c) $a = -0.8$, $b = 0$. (d) $a = -0.5$, $b = 0$. (e) $a = -0.2$, $b = 0$. (f) $a = -0.15$, $b = 0$. (g) $a = -6.17$, $b = -1$. (h) $a = -4.5$, $b = -1$. (i) $a = -0.8$, $b = -1$.

Figure 3 shows some coexisting chaotic flows of system (1) for some special a. From this figure, we can see that a chaotic flow coexists with a limit cycle (Figure 3(b)), two limit cycles coexist (Figure 3(c)), and three limit cycles (a pair of symmetric limit cycles) coexist (Figure 3(d)). The results show that in phase space, there are independent chaotic and quasiperiodic attractive basins, i.e., chaotic flows coexist with periodic limit cycle. Moreover, we plot the basin attractors as shown in Figure 4. The blue area represents the stable domain of system parameters, and the red area represents the unstable domain of system parameters.

3. Design of Bifurcation-Based Partial-State Feedback Controller

3.1. Partial-State Feedback Controller. In this section, we will consider system (1) subjected to linear feedback control with desired periodic motions. As far as we know, the simplest way to get a period orbit is through Hopf bifurcation. By using the projection method for the calculation of the first and second Lyapunov coefficients associated to the Hopf bifurcation, the generic and degenerate Hopf bifurcation in the controlled system are studied. Consider the controlled system

$$
\begin{aligned}
\dot{x} &= y, \\
\dot{y} &= -x - yz, \\
\dot{z} &= a - bx^2 + cy^2 + ez.
\end{aligned}
\tag{6}
$$

When $e \neq 0$, system (6) has only one equilibrium $(0, 0, -(a/e))$. Let $\overline{x} = x$, $\overline{y} = y$, $\overline{z} = z + (a/e)$, then system (6) will become

$$
\begin{aligned}
\dot{\overline{x}} &= \overline{y}, \\[4pt]
\dot{\overline{y}} &= -\overline{x} - \overline{y}\left(\overline{z} - \frac{a}{e}\right), \\[4pt]
\dot{\overline{z}} &= -b\overline{x}^2 + c\overline{y}^2 + e\overline{z},
\end{aligned}
\tag{7}
$$

and the equilibrium will become an origin O; the Jacobian matrix of system (7) at O is

$$
\begin{pmatrix}
0 & 1 & 0 \\[6pt]
-1 & \dfrac{a}{e} & 0 \\[6pt]
0 & 0 & e
\end{pmatrix}.
\tag{8}
$$

(a)

(b)

(c)

(d)
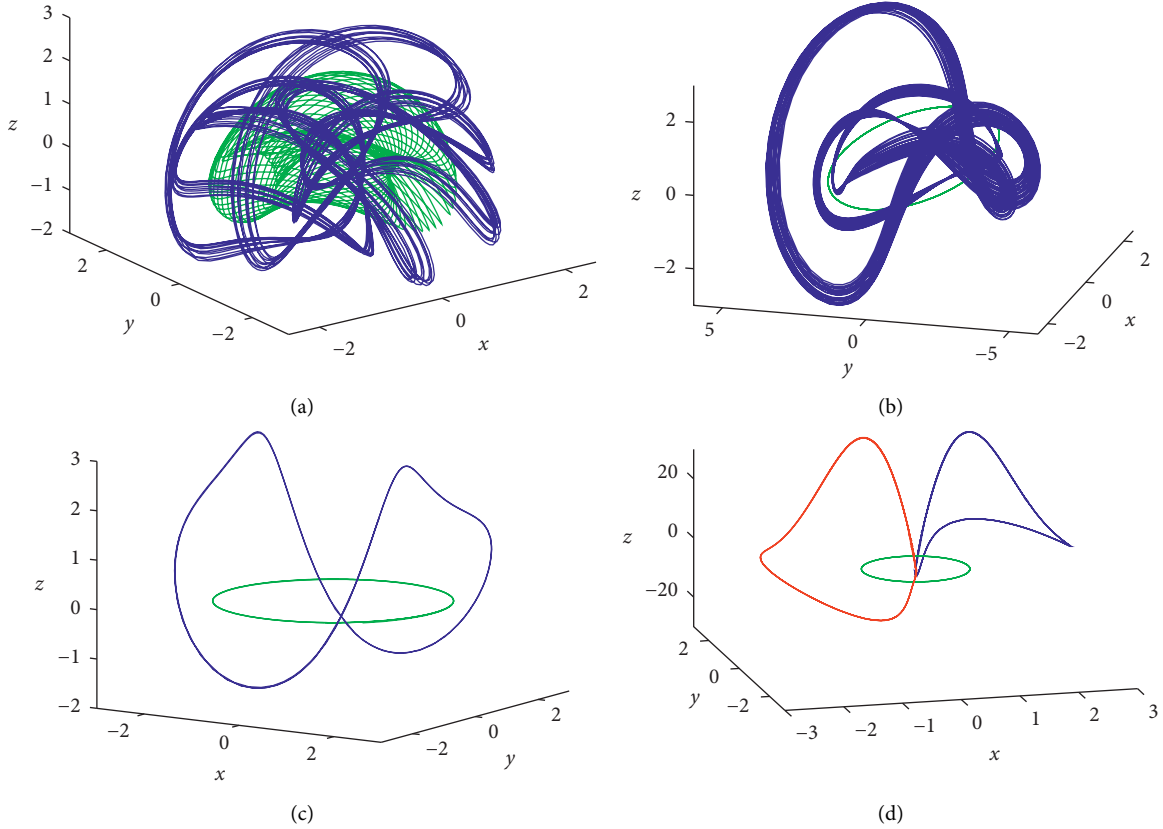
FIGURE 3: Coexisting chaotic flow of system (1) for $c = 1$ at various values of a. (a) Chaotic flow coexists a torus for system (1) with $a = -1$, $b = 0$. (b) Chaotic flow coexists limit cycle for system (1) with $a = -6.17$, $b = -1$. (c) Two limit cycles coexisting for system (1) with $a = -4.5$, $b = -1$. (d) Three limit cycles coexisting for system (1) with $a = -0.8$, $b = -1$.
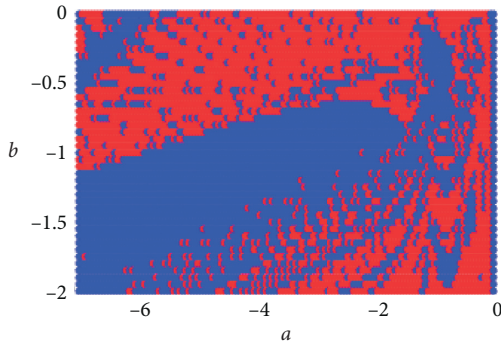
FIGURE 4: Basin attractors of system (1) for $c = 1$ at various values of a and b.

Meanwhile, the corresponding characteristic equation is

$$\lambda^3 - \left(e + \frac{a}{e}\right)\lambda^2 + (a + 1)\lambda - e = 0, \tag{9}$$

and the eigenvalues are

$$\lambda_1 = e,$$

$$\lambda_{2,3} = \frac{a \pm \sqrt{a^2 - 4e^2}}{2e}. \tag{10}$$

Obviously, when $a = a_0 \stackrel{\text{def}}{=} 0$, system (9) has a pair of pure imaginary roots $\pm i$, and the corresponding eigenvalues are

$$\lambda_1 = e,$$

$$\lambda_{2,3} = \pm i. \tag{11}$$

Taking a as the Hopf bifurcation parameter, according to equation (9), we have

$$\frac{d\lambda}{da} = \frac{(1/e)\lambda^2 - 1}{3\lambda^2 - 2(e + (a/e))\lambda + (a + 1)}. \tag{12}$$

Hence,

$$\text{Re} \frac{d\lambda}{da}\Big|_{a=0,\lambda=i} = \frac{1 + e}{2e(1 + e^2)},$$

$$\tag{13}$$

$$\text{Im} \frac{d\lambda}{da}\Big|_{a=0,\lambda=i} = -\frac{1 + e}{2(1 + e^2)}.$$

When $e < 0, e \neq -1$, the transversally condition $\text{Re}(d\lambda/da)|_{a=0,\lambda=i} \neq 0$ is satisfied.

Proposition 1. *Define the Hopf surface*

$$\mathcal{S}_h = \{(a, b, c, e)|a = a_0, e < 0, e \neq -1\}. \tag{14}$$

If $(a, b, c, e) \in \mathcal{S}_h$, then the Jacobian matrix of (7) at O has one negative real eigenvalue $\lambda_1 = e$ and a pair of purely imaginary eigenvalues $\lambda_{2,3} = \pm i$.

Meanwhile, we have the following proposition.

Proposition 2. *If $(a, b, c, e) \in \mathcal{S}_h$, the Hopf bifurcation is at the origin O when a varies and passes through the critical value a_0.*

The following of this section is a review of the projection method for the degenerate Hopf bifurcation.

Consider the differential equation

$$\dot{X} = f(X, \mu), \tag{15}$$

where $X \in \mathbb{R}^3$ and $\mu \in \mathbb{R}^4$. Suppose system (15) has a zero equilibrium when $\mu = \mu_0$ and let

$$F(X) = f(X, \mu_0) = AX + \frac{1}{2!}B(X, X) + \frac{1}{3!}C(X, X, X)$$

$$+ \frac{1}{4!}D(X, X, X, X) + \frac{1}{5!}E(X, X, X, X, X) + \frac{1}{6!}K(X, X, X, X, X, X) \tag{16}$$

$$+ \frac{1}{7!}L(X, X, X, X, X, X, X) + O(\|X\|^8),$$

where

$$A = f_X(X, \mu_0),$$

$$B_i(X, Y) = \sum_{j,k=1}^{3} \left. \frac{\partial^2 F_i(\xi)}{\partial \xi_j \partial \xi_k} \right|_{\xi=0} X_j Y_k, \tag{17}$$

$$C_i(X, Y, Z) = \sum_{j,k=1}^{3} \left. \frac{\partial^3 F_i(\xi)}{\partial \xi_j \partial \xi_k \partial \xi_l} \right|_{\xi=0} X_j Y_k Z_l,$$

for $i = 1, 2, 3$ and so on for D, E, K, L.

Suppose A has a pair of purely imaginary eigenvalues $\lambda_{2,3} = \pm \omega_0 i, \omega_0 > 0$, let T^c be the generalized eigenspace of A corresponding to $\lambda_{2,3}$ and $p, q \in \mathbb{R}^3$ be vectors, such that

$$Aq = i\omega_0 q, A^T p = -i\omega_0 p, \langle p, q \rangle = \sum_{i=1}^{3} \overline{p}_i q_i = 1, \tag{18}$$

where A^T is the transpond of A.

Any vector $y \in T^c$ can be represented as

$$y = wq + \overline{wq}, \tag{19}$$

where $w = \langle p, y \rangle \in \mathbb{C}$.

The 2D center manifold associated to the eigenvalues $\lambda_{2,3} = \pm \omega_0 i$ can be parameterized by the variables w and $\overline{w}$ by means of an immersion of the form

$$X = H(w, \overline{w}), \tag{20}$$

where $H: \mathbb{C}^2 \longrightarrow \mathbb{R}^2$ has a Taylor expansion of the form

$$H(w, \overline{w}) = wq + \overline{wq} + \sum_{2 \le j+k \le 7} \frac{1}{j!k!} h_{jk} w^j \overline{w}^k + O(|w|^8), \tag{21}$$

with $h_{jk} \in \mathbb{C}$ and $h_{jk} = \overline{h}_{kj}$. Substituting this expression into (16), we have

$$H_w \dot{w} + H_{\overline{w}} \dot{\overline{w}} = F(H(w, \overline{w})). \tag{22}$$

The complex vectors h_{jk} are obtained solving system (22). Taking into account the coefficients of F, system (22) can be written as

$$\dot{w} = i\omega_0 w + \frac{1}{2} G_{21} w|w|^2 + \frac{1}{12} G_{32} w|w|^4 + \frac{1}{144} G_{43} w|w|^6 + O(|w|^8). \tag{23}$$

The first Lyapunov coefficient l_1 is defined by

$$l_1 = \frac{1}{2} \operatorname{Re}(G_{21}), \tag{24}$$

where $G_{21} = \langle p, \mathcal{H}_{21} \rangle$, and $\mathcal{H}_{21} = C(q, q, \overline{q}) + B(\overline{q}, h_{20}) - 2B(q, h_{11})$.

Define $\mathcal{H}_{32}$ as

$$\mathcal{H}_{32} = 6B(h_{11}, h_{21}) + B(\overline{h}_{20}, h_{30}) + 3B(\overline{h}_{12}, h_{20}) + 3B(q, h_{22}) + 2B(\overline{q}, h_{31}) + 6C(q, h_{11}, h_{11}) + 3C(q, \overline{h}_{20}, h_{20})$$

$$+ 3C(q, q, \overline{h}_{21}) + 6C(q, \overline{q}, h_{21}) + 6C(\overline{q}, h_{20}, h_{11}) + C(\overline{q}, \overline{q}, h_{30}) + D(q, q, q, \overline{h}_{20}) \tag{25}$$

$$+ 6D(q, q, \overline{q}, h_{11}) + 3D(q, \overline{q}, \overline{q}, h_{20}) + E(q, q, q, \overline{q}, \overline{q}) - 6G_{21} h_{21} - 3\overline{G}_{21} h_{21}.$$

The second Lyapunov coefficient l_2 is defined by

$$l_2 = \frac{1}{12} \operatorname{Re}(G_{32}), \tag{26}$$

where $G_{21} = \langle p, \mathscr{H}_{32} \rangle$.

The third Lyapunov coefficient l_3 is defined by

$$l_3 = \frac{1}{144} \operatorname{Re}(G_{43}), \tag{27}$$

where $G_{43} = \langle p, \mathscr{H}_{43} \rangle$. The expression for $\mathscr{H}_{43}$ is too large to be put in print and can be found in [47].

3.2. Hopf Bifurcation Analysis.
In this section, we study the stability of O for parameters in $\mathscr{S}_h$. Using the notation of the previous section, system (7) can be written as

$$\dot{X} = AX + \frac{1}{2}B(X, X), \tag{28}$$

where

$$
A = \begin{pmatrix} 0 & 1 & 0 \\ -1 & 0 & 0 \\ 0 & 0 & e \end{pmatrix},
$$
$$
X = \begin{pmatrix} \overline{x} \\ \overline{y} \\ \overline{z} \end{pmatrix}, \tag{29}
$$

and the multilinear symmetric function

$$
B(X, Y) = \begin{pmatrix} 0 \\ -X_2 Y_3 - X_3 Y_2 \\ -2b X_1 Y_1 + 2c X_2 Y_2 \end{pmatrix}. \tag{30}
$$

Meanwhile, we can calculate q, p such that $\langle p, q \rangle = 1$ and

$$
q = \begin{pmatrix} -i & 1 & 0 \end{pmatrix}^T,
$$
$$
p = \begin{pmatrix} -\frac{1}{2}i & \frac{1}{2} & 0 \end{pmatrix}^T. \tag{31}
$$

The complex vectors h_{11}, h_{20}, and h_{30} are

$$
h_{11} = -A^{-1} B(q, \overline{q}) = \begin{pmatrix} 0 & 0 & \dfrac{2(b-c)}{e} \end{pmatrix}^T,
$$
$$
h_{20} = (2i\omega_0 I - A)^{-1} B(q, q) = \begin{pmatrix} 0 & 0 & \dfrac{2(b+c)}{2i-e} \end{pmatrix}^T,
$$
$$
h_{30} = 3(3i\omega_0 I - A)^{-1} B(q, h_{20}) = \begin{pmatrix} \dfrac{3(b+c)}{4(2i-e)} & \dfrac{9(b+c)i}{4(2i-e)} & 0 \end{pmatrix}^T. \tag{32}
$$

The complex number G_{21} has the form

$$G_{21} = -\frac{2(b-c)}{e} - \frac{b+c}{2i-e}. \tag{33}$$

Defining $b = b_0 \triangleq ((3e^2 + 8)c/(e^2 + 8))$ and the following subsets of the Hopf surface $\mathscr{S}_h$,

$$
\mathscr{U} = \left\{ (a,b,c,e) \,|\, a = a_0, b > \frac{3e^2 + 8}{e^2 + 8}c, e < 0, e \neq -1 \right\},
$$
$$
\mathscr{S} = \left\{ (a,b,c,e) \,|\, a = a_0, b < \frac{3e^2 + 8}{e^2 + 8}c, e < 0, e \neq -1 \right\}. \tag{34}
$$

Hence, we have the following theorem.

Theorem 1. *The first Lyapunov coefficient at O for parameters in $\mathscr{S}_h$ is given by*

$$l_1 = \frac{(3e^2 + 8)c - (e^2 + 8)b}{2e(e^2 + 4)}. \tag{35}$$

If $(3e^2 + 8)c - (e^2 + 8)b \neq 0$, system (7) has a transversal Hopf point at O for $(a,b,c,e) \in \mathscr{S}_h$. More specifically, if $(a,b,c,e) \in \mathscr{U}$, then the Hopf point at O is unstable (weak repelling focus), and for each $a < a_0$, but close to a_0, there exists an unstable limit cycle near the asymptotically stable equilibrium O; if $(a,b,c,e) \in \mathscr{S}$, then the Hopf point at O is stable (weak attractor focus), and for each $a > a_0$, but close to a_0, there exists a stable limit cycle near the unstable equilibrium point O.

If $a = -0.01, b = 1, c = 0, e = -2$, then $(3e^2 + 8)c - (e^2 + 8)b = -12 \neq 0$, and $b = 1 > ((3e^2 + 8)/(e^2 + 8))c = 0$, so $(a,b,c,e) \in \mathscr{U}$. According to Theorem 1, system (7) is unstable, and for each $a < a_0$, but close to a_0, there exists an unstable limit cycle near the asymptotically stable equilibrium O. We can get the numerical simulation results as shown in Figure 5(a); there exists an asymptotically stable equilibrium O.

If $a = 0.01, b = -1, c = 1, e = -2$, then $(3e^2 + 8)c - (e^2 + 8)b = 32 \neq 0$, and $b = -1 < ((3e^2 + 8)/(e^2 + 8))c = (20/12)$, so $(a,b,c,e) \in \mathscr{S}$. According to Theorem 1, system (7) is stable, and for each $a > a_0$, but close to a_0, there exists a stable limit cycle near the unstable equilibrium point O. We can get the numerical simulation results as shown Figure 5(b), and there exists an unstable equilibrium O.

The first Lyapunov coefficient vanishes on the straight line:

$$\mathscr{S}_l = \left\{ (a,b,c,e) \,|\, a = a_0, b = \frac{3e^2 + 8}{e^2 + 8}c, e < 0, e \neq -1 \right\}. \tag{36}$$

The second Lyapunov coefficient on the straight line $\mathscr{S}_l$ where the first Lyapunov coefficient vanishes will be calculated in the following.

The complex vector h_{21} can be solved by solving the following equation:

$$
\begin{pmatrix} iI - A & q \\ \overline{p}^T & 0 \end{pmatrix} \begin{pmatrix} h_{21} \\ s \end{pmatrix} = \begin{pmatrix} B(\overline{q}, h_{20}) + 2B(q, h_{11}) - G_{21}q \\ 0 \end{pmatrix}, \tag{37}
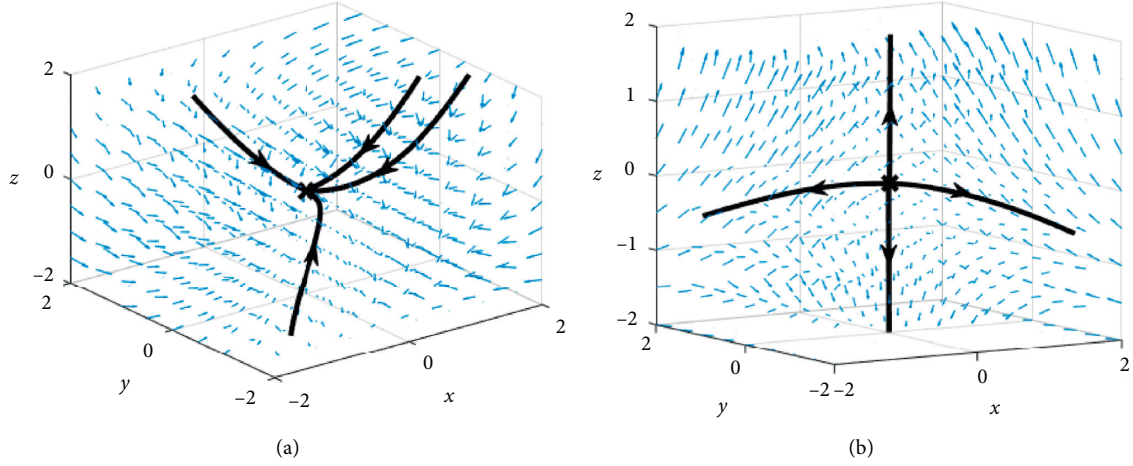$$

(a)

(b)

FIGURE 5: Stability of control parameters under the first Lyapunov exponent. (a) $a = -0.01$, $b = 1$, $c = 0$, $e = -2$. (b) $a = 0.01$, $b = -1$, $c = 1$, $e = -2$.

and we have

$$h_{21} = \left(-\frac{4c\,(ei+2)}{(e^2+8)\,(2i-e)} \quad \frac{4c\,(ei+2)i}{(e^2+8)\,(2i-e)} \quad 0 \right)^T. \quad (38)$$

From the coefficients of the term w^4, $w^3\overline{w}$, and $w^2\overline{w}^2$ in (22), we have

$$h_{40} = (4iI - A)^{-1}\left[3B\,(h_{20}, h_{20}) + 4B\,(q, h_{30})\right]$$

$$= \left(0 \quad 0 \quad \frac{48c^2\,(e^2+4)\,(3e^2+16)i}{(4i-e)\,(e^2+8)^2\,(2i-e)} \right)^T$$

$$h_{31} = (2iI - A)^{-1}\left[3B\,(q, h_{21}) + B\,(\overline{q}, h_{30}) + 3B\,(h_{20}, h_{11}) - 3G_{21}h_{20}\right]$$

$$= \left(0 \quad 0 \quad \frac{48c^2\,(16e^3 i - e^4 + 8ei + 8e^2 + 16)}{(e^2+8)^2\,(2i-e)^3} \right)^T$$

$$h_{22} = -A^{-1}\left[2B\,(h_{11}, h_{11}) + 2B\,(q, \overline{h}_{21}) + 2B\,(\overline{q}, h_{21}) + B\,(\overline{h}_{20}, h_{20})\right]$$

$$= \left(0 \quad 0 \quad -\frac{64\,(ue^6 + 20ue^4 + c^2 e^2 + 128e^2 u + 4c^2 + 256u)}{e\,(e^2+8)^2} \right)^T, \quad (39)$$

$$G_{32} = \frac{12}{(e^2+8)^2\,(2i-e)^3\,(ei+2)e} \begin{pmatrix} -512c^2 - 32768ui - 3ve^{13} - 88ue^9 + 24ive^{12} + 480ive^{10} \\ -12iue^{10} + 2688ive^8 - 16ic^2 e^4 - 1536ive^6 - 49152ive^4 \\ -9830ive^2 + 3136iue^6 + 25088iue^4 + 576ic^2 e^2 + 45056iue^2 \\ -49152ve + 73728ue + 11520ve^7 + 1056ve^9 - 1472ue^7 \\ +42240ve^5 - 5504ue^5 + 36864ve^3 + 14336ue^3 - 160c^2 e^3 + 896c^2 e \end{pmatrix},$$

where

$$u = \left| \frac{c^2 (ei + 2)^2}{\left(e^2 + 8\right)^2 (2i - e)^2} \right|,$$

$$v = \left| \frac{c^2}{\left(e^2 + 8\right)^2 (2i - e)^2} \right|. \tag{40}$$

Hence, we have the following theorem.

Theorem 2. *The second Lyapunov coefficient at O for parameter in $\mathscr{S}_l$ is given by*

$$l_2|_{\mathscr{S}_l} = \frac{4c^2 \left(3e^6 + 44e^4 + 192e^2 + 256 + 4\left(e^2 + 8\right)^2\right)}{e\left(e^2 + 4\right)\left(e^2 + 8\right)^3} < 0. \tag{41}$$

Moreover, the Hopf point at O is stable (weak attractor focus), and for each $a > a_0$, but close to a_0, there exists a stable limit cycle near the unstable equilibrium point O.

If $a = 0.01, b = 5, c = 3, e = -2$, then $b = ((3e^2 + 8)/(e^2 + 8))c = 5$, and $(a, b, c, e) \in S_l$. According to Theorem 2,

the Hopf point at O is unstable. We can get the numerical simulation results as shown in Figure 6.

4. Circuit Model Construction and Simulation

4.1. Circuit Model Construction. In this section, we adopted the analog circuit to illustrate the correctness of above analyzes. The chaotic system (1) can be rewritten as follows when $b = -1, c = 1$:

$$\begin{cases} \dot{x} = y, \\ \dot{y} = -x - yz, \\ \dot{z} = a + x^2 + y^2 + ez. \end{cases} \tag{42}$$

Then, according to system (42), the circuit principle diagram is designed as shown in Figure 7. The analog circuit is constructed by the AD633 analog multipliers, resistors, LM741 operational amplifiers, and capacitors. The parameters are set as that the gain of multiplier AD633 is 0.1, the voltage of the operational amplifier LM741 is bounded as 15 V, and the output saturated voltage of the operational amplifier LM741 is bounded as 13.5 V; the capacitors are chosen as $C_1 = C_2 = C_3 = 10$ nF. We let the time constant $\tau = t/10R_iC_i$; then, the corresponding circuit equations can be rewritten as

$$\begin{cases} \dfrac{dx}{d\tau} = -10\left(\dfrac{R_{12}}{R_{11}} \cdot (-y)\right), \\[3mm] \dfrac{dy}{d\tau} = -10\left(\dfrac{R_{23}}{R_{21}} \cdot x + \dfrac{R_{23}}{10R_{22}} \cdot yz\right), \\[3mm] \dfrac{dz}{d\tau} = -10\left(-\dfrac{eR_{35}}{100} \cdot (-z) + \dfrac{R_{35}}{10R_{32}} \cdot \left(-x^2\right) + \dfrac{R_{35}}{10R_{33}}\left(-y^2\right) + \dfrac{R_{35}}{R_{34}} \cdot (-a)\right). \end{cases} \tag{43}$$

In the circuit of the state equation x, the values of resistances are $R_{11} = 100 \text{ k}\Omega, R_{12} = R_{13} = R_{14} = R_{15} = 10 \text{ k}\Omega$. In the circuit of the state equation y, the values of resistances are $R_{21} = 100 \text{ k}\Omega, R_{22} = R_{23} = R_{24} = R_{25} = R_{26} = 10 \text{ k}\Omega$. In the circuit of the state equation z, the values of resistances are $R_{34} = 100 \text{ k}\Omega, R_{32} = R_{33} = R_{35} = R_{36} = R_{37} = R_{38} = 10 \text{ k}\Omega, R_{31} = (100/(-e)) \text{ k}\Omega$, and a can take different values. In order to set the initial value, we add a power supply and two switches at both ends of the capacitor C_2 and provide initial capacitance value by charging the capacitor C_2.

4.2. Circuit Simulation. We consider the following two cases. In the case A, we consider $e = 0$, and the dynamic behavior will be reproduced by the simulation results. Then, in the case B, the control term ez will be added to the system, and the simulation results will demonstrate the Hopf bifurcation analysis results are as follows:

Case A ($e = 0$): in this case, the control term ez is not considered. The simulation results of the digital oscilloscope are shown in Figure 8. From Figure 8, it can be observed different motion states of system (1) for different values of the parameter a, b under $c = 1$. From Figures 8(a) and 8(b), the rotationally symmetric chaotic flow can be observed under the parameters $a = 5, b = 0$ or $a = -4, b = 0$. From Figures 8(c) and 8(d), under the parameters $a = 5, b = 0$ or $a = -0.2, b = 0$, the symmetric pair of chaotic flows can be observed. From Figure 8(e), under the parameters $a = -4.5$ and $b = -1$, the symmetric limit cycle can be observed. From Figure 8(f), under the parameters $a = -0.8$ and $b = -1$, the symmetric pair of limit cycles can observed. Thus, the results of analog circuit verify the results of the numerical simulation as shown in Figure 2.

From Section 2.2, we know that system (1) has coexistence. In this section, we adopt the circuit simulation
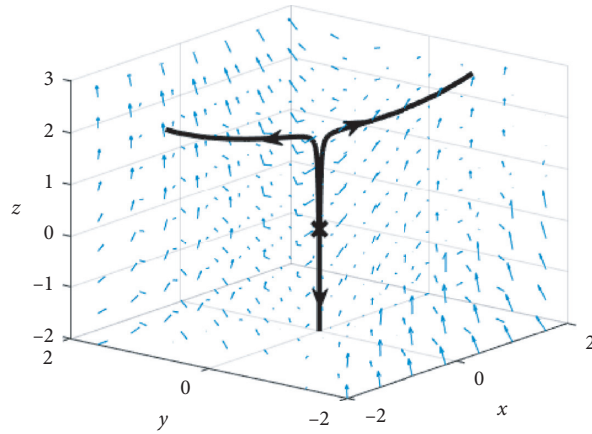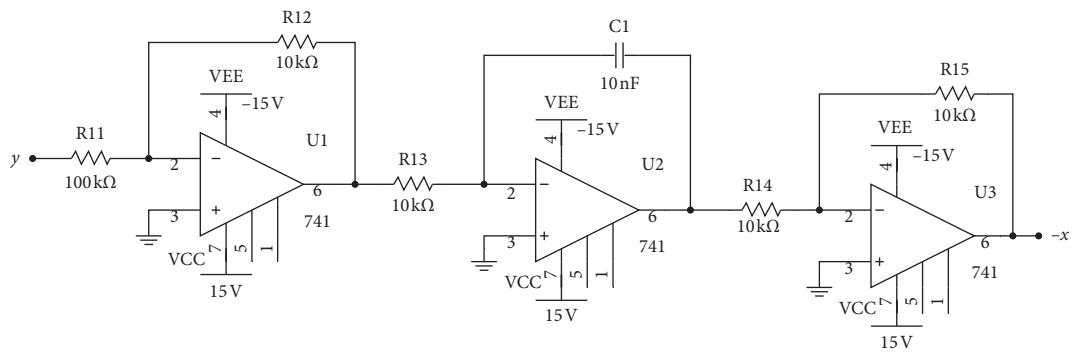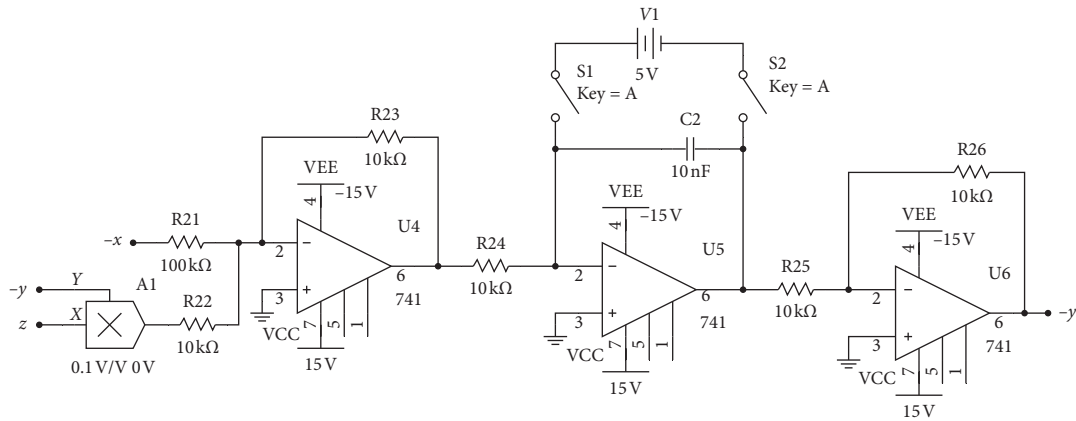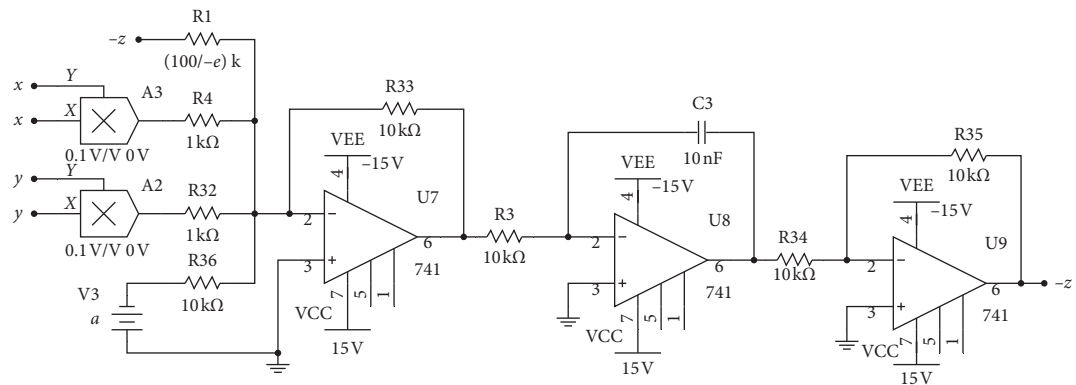
FIGURE 6: Stability of control parameters under the second Lyapunov exponent.

(a)

(b)

(c)

FIGURE 7: Circuit principle diagram. (a) Circuit principle diagram of state x. (b) Circuit principle diagram of state y. (c) Circuit principle diagram of state z.
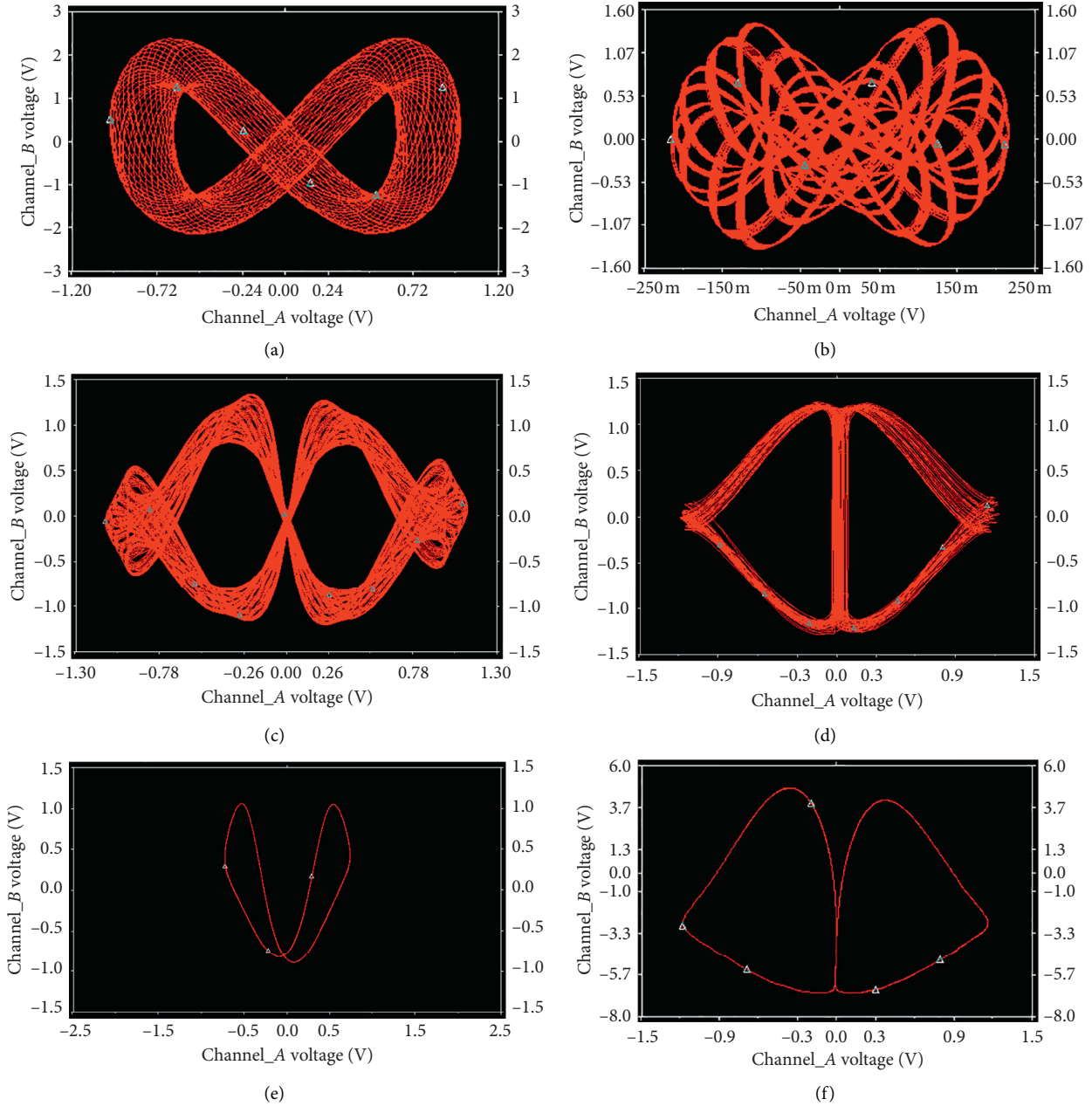
(a)

(b)

(c)

(d)

(e)

(f)

Figure 8: Circuit simulation results of case A. (a) $a = -5$, $b = 0$. (b) $a = -4$, $b = 0$. (c) $a = -0.8$, $b = 0$. (d) $a = -0.2$, $b = 0$. (e) $a = -4.5$, $b = -1$. (f) $a = -0.8$, $b = -1$.

to reproduce the coexistence as shown in Figure 3(c). The system parameters are $a = -4.5, b = -1, c = 1$, and the initial values are $(0, 5, 0)$ and $(0, 2.12, 0)$; we can get the circuit simulation results as shown in Figure 9. Since Figure 3(c) is the $x - y - z$ phase diagram, Figure 9 uses (a)–(d) to reproduce the diagram, where Figure 9(a) is the $x - y$ map of the blue limit cycle, Figure 9(b) is the $x - z$ map of the blue limit cycle, Figure 9(c) is the $x - y$ map of the green limit cycle, and Figure 9(d) is the $x - z$ map of the green limit cycle. We can see that the results of analog circuit verify the numerical simulation results as shown in Figure 3(c).

Case B ($e \neq 0$): when the control term $e = 0$, for $a = -0.2, b = 0, c = 1$ and $a = 0.001, b = 0, c = 1$, the simulation results are shown in Figures 10(a) and 10(c). From Figures 10(a) and 10(c), the chaotic phenomenon can be observed. Then, the control term ez is added into system, based on the analysis of Section 3, and we let $e = -2$. The simulation results of $e = -2$ are shown in Figures 10(b) and 10(d); obviously, the chaotic phenomenon in Figures 10(a) and 10(c) can be eliminated.

In the simulation experiment, we found an interesting phenomenon. Under the parameter $a = -0.05, b = 1, c = 0.5$,

(a)

(b)

(c)

(d)
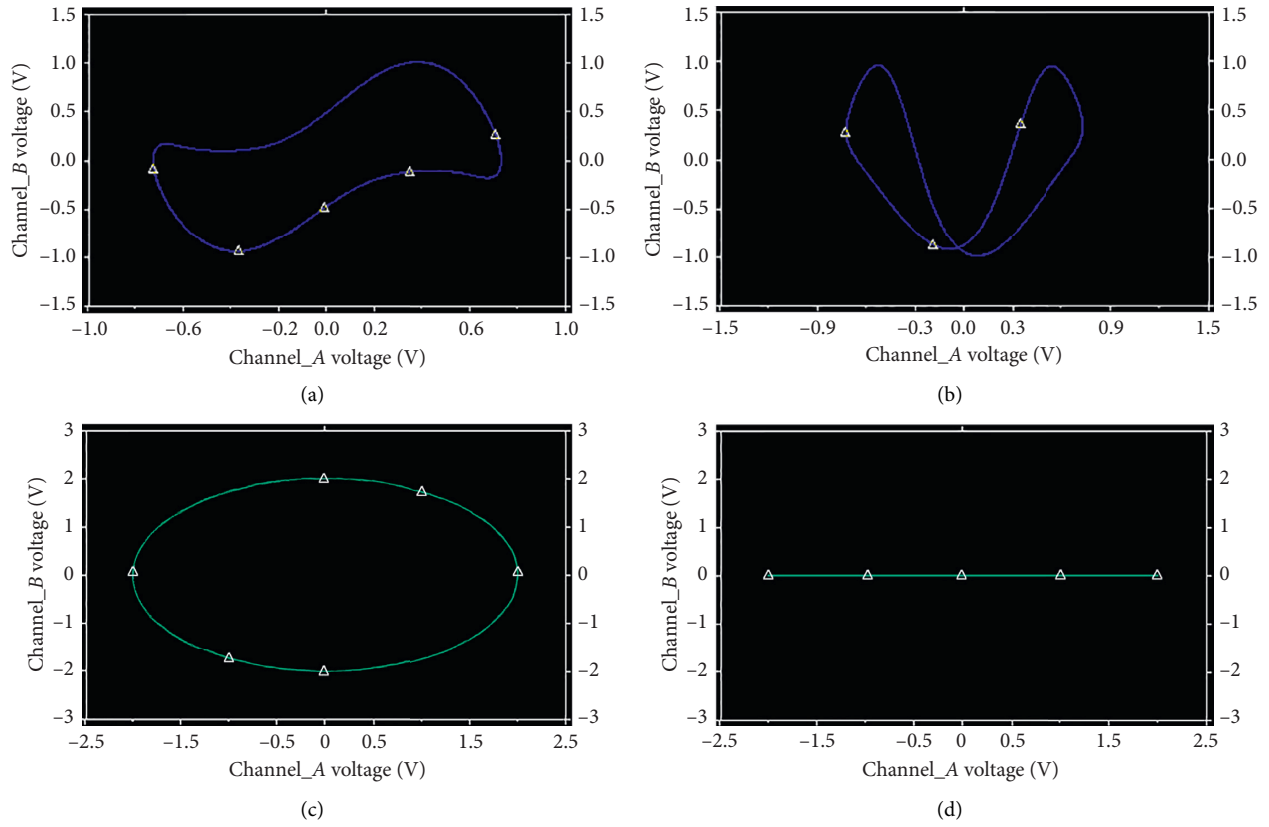
FIGURE 9: Circuit simulation results of coexisting symmetric chaotic flow for system (1). (a) $x - y$ map. Initial value is (0, 5, 0). (b) $x - z$ map. Initial value is (0, 5, 0). (c) $x - y$ map. Initial value is (0, 2.12, 0). (d) $x - z$ map. Initial value is (0, 2.12, 0).

(a)

(b)

(c)

(d)
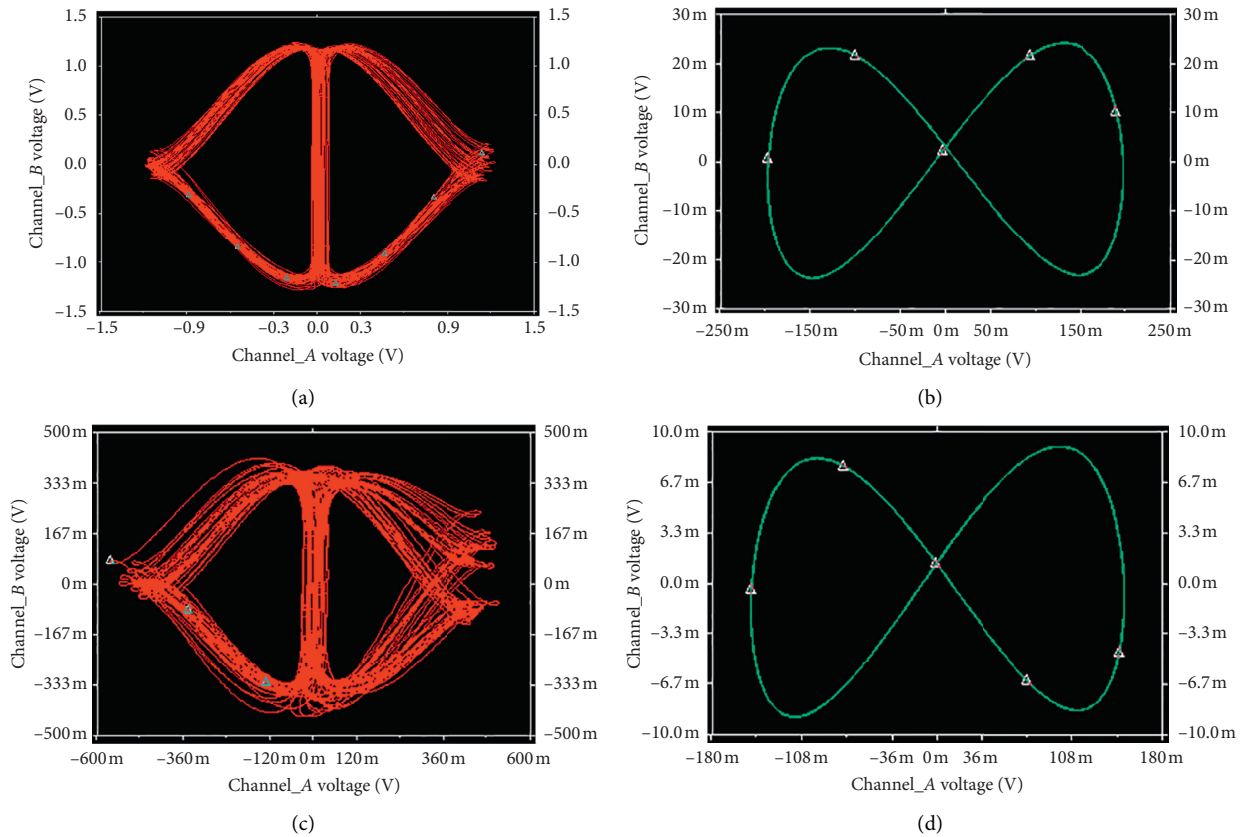
FIGURE 10: Circuit simulation results of case B. (a) $a = -0.2$, $b = 0$, $c = 1$, $e = 0$. (b) $a = -0.2$, $b = 0$, $c = 1$, $e = -2$. (c) $a = 0.001$, $b = 0$, $c = 1$, $e = 0$. (d) $a = 0.001$, $b = 0$, $c = 1$, $e = -2$.

(a)

(b)
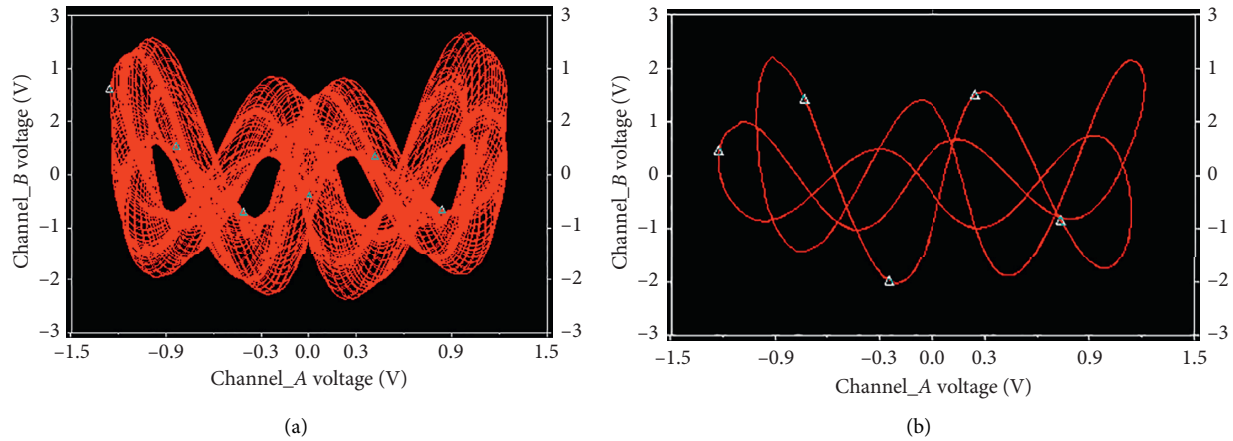
FIGURE 11: Circuit simulation results of rotationally symmetric chaotic flow with four-wing. (a) $a = -0.05$, $b = 1$, $c = 0.5$, $R22 = 1.55\,\text{k}\Omega$. (b) $a = -0.05$, $b = 1$, $c = 0.5$, $R22 = 1.53\,\text{k}\Omega$.

an interesting phenomenon can be observed by changing the value of resistance R_{22}. For $R_{22} = 1.55\,\text{k}\Omega$, the rotationally symmetric chaotic flow with four-wing can be observed (Figure 11(a)). Then, reducing the resistance R_{22} to $R_{22} = 1.53\,\text{k}\Omega$, the point symmetric limit cycle and axial symmetric limit cycle can be observed as shown in Figure 11(b).

5. Conclusion

In this study, a novel conservative chaotic system with no equilibria was investigated. Numerical analysis shows the various chaotic characteristics, including the analysis of the conservativeness, the symmetry and invariance, and coexisting chaotic behaviors. Based on one-dimensional state to feedback, a partial-state feedback controller was constructed. Then, the degenerate Hopf bifurcation method was adopted to illustrate the stable domain of control parameters. Finally, an analog circuit system was constructed to simulate the investigated chaotic system, and the circuit simulation results reproduced the numerical analysis results. Indeed, the global dynamics of this new chaotic system and the generation mechanism of chaos is still not fully explained, which is also the content of our future research.

Data Availability

The data generated or analyzed during this study are included within this article.

Conflicts of Interest

The authors declare that they have no conflicts of interest.

Acknowledgments

References

[1] E. N. Lorenz, "Deterministic nonperiodic flow," *Journal of the Atmospheric Sciences*, vol. 20, no. 2, pp. 130–141, 1963.
[2] O. E. Rossler, "An equation for hyperchaos," *Physics Letters A*, vol. 71, no. 2-3, pp. 155–157, 1979.
[3] G. Chen and T. Ueta, "Yet another chaotic attractor," *International Journal of Bifurcation and Chaos*, vol. 09, no. 07, pp. 1465-1466, 1999.
[4] L. Jinhu and G. Chen, "A new chaotic attractor coined," *International Journal of Bifurcation and Chaos*, vol. 12, no. 03, pp. 659–661, 2002.
[5] S. He, Y. Peng, and K. Sun, "Seir modeling of the covid-19 and its dynamics," *Nonlinear Dynamics*, vol. 101, no. 3, pp. 1667–1680, 2020.
[6] Y. Peng, S. He, and K. Sun, "A higher dimensional chaotic map with discrete memristor," *AEU—International Journal of Electronics and Communications*, vol. 129, Article ID 153539, 2021.
[7] C. P. Silva, "Shil'nikov's theorem-a tutorial," *IEEE Transactions on Circuits and Systems I: Fundamental Theory and Applications*, vol. 40, no. 10, pp. 675–682, 1993.
[8] G. A. Leonov, N. V. Kuznetsov, and V. I. Vagaitsev, "Localization of hidden Chua's attractors," *Physics Letters A*, vol. 375, no. 23, pp. 2230–2233, 2011.
[9] V.-T. Pham, C. Volos, S. Jafari, Z. Wei, and X. Wang, "Constructing a novel no-equilibrium chaotic system," *International Journal of Bifurcation and Chaos*, vol. 24, no. 5, Article ID 1450073, 2014.
[10] Z. Wang, I. Moroz, Z. Wei, and H. Ren, "Dynamics at infinity and a hopf bifurcation arising in a quadratic system with coexisting attractors," *Pramana*, vol. 90, no. 1, p. 12, 2018.
[11] Z. Wang, I. I. Hamarash, P. Sadeghi, and J. S. Shabestari, "A new megastable oscillator with rational and irrational parameters," *International Journal of Bifurcation and Chaos*, vol. 29, no. 13, 2019.
[12] X. Wang and G. Chen, "A chaotic system with only one stable equilibrium," *Communications in Nonlinear Science and Numerical Simulation*, vol. 17, no. 3, pp. 1264–1272, 2012.

[13] H. Tian, Z. Wang, P. Zhang, M. Chen, and Y. Wang, "Dynamic analysis and robust control of a chaotic system with hidden attractor," *Complexity*, vol. 2021, Article ID 8865522, 11 pages, 2021.

[14] Z. Wang, Z. Wei, K. Sun et al., "Chaotic flows with special equilibria," *The European Physical Journal Special Topics*, vol. 229, no. 6-7, pp. 905–919, 2020.

[15] Z. Wang, X. Xi, L. Kong, and Z. Wei, "Infinity dynamics and ddf control for a chaotic system with one stable equilibrium," *The European Physical Journal Special Topics*, vol. 229, no. 6-7, pp. 1319–1333, 2020.

[16] Z. Wang, Z. Xu, E. Mliki, A. Akgul, V.-T. Pham, and S. Jafari, "A new chaotic attractor around a pre-located ring," *International Journal of Bifurcation and Chaos*, vol. 27, no. 10, Article ID 1750152, 2017.

[17] S. Zhang, C. Zhang, Z. Wang, and W. Kong, "Combining sparse representation and singular value decomposition for plant recognition," *Applied Soft Computing*, vol. 67, pp. 164–171, 2018.

[18] N. Wang, G. Zhang, N. V. Kuznetsov, and B. Han, "Hidden attractors and multistability in a modified chua's circuit," *Communications in Nonlinear Science and Numerical Simulation*, vol. 92, Article ID 105494, 2021.

[19] V.-T. Pham, A. Ouannas, C. Volos, and T. Kapitaniak, "A simple fractional-order chaotic system without equilibrium and its synchronization," *AEU—International Journal of Electronics and Communications*, vol. 86, pp. 69–76, 2018.

[20] C. Li and J. C. Sprott, "Coexisting hidden attractors in a 4-d simplified lorenz system," *International Journal of Bifurcation and Chaos*, vol. 24, no. 3, Article ID 1450034, 2014.

[21] A. J. Lichtenberg and M. A. Lieberman, *Regular and Stochastic Motion*, Springer Science & Business Media, Berlin, Germany, 2013.

[22] S. Cang, A. Wu, Z. Wang, and Z. Chen, "Four-dimensional autonomous dynamical systems with conservative flows: two-case study," *Nonlinear Dynamics*, vol. 89, no. 4, pp. 2495–2508, 2017.

[23] S. Cang, Li Yue, Z. Kang, and Z. Wang, "A generic method for constructing *n*-fold covers of 3d conservative chaotic systems," *Chaos: An Interdisciplinary Journal of Nonlinear Science*, vol. 30, no. 3, Article ID 033103, 2020.

[24] R. Guesmi, M. A. B. Farah, A. Kachouri, and M. Samet, "A novel chaos-based image encryption using dna sequence operation and secure hash algorithm sha-2," *Nonlinear Dynamics*, vol. 83, no. 3, pp. 1123–1136, 2016.

[25] K. Georges, E. Soujeri, and Y. Nijsure, "Design of a short reference noncoherent chaos-based communication systems," *IEEE Transactions on Communications*, vol. 64, no. 2, pp. 680–689, 2016.

[26] S. Jafari, V.-T. Pham, and T. Kapitaniak, "Multiscroll chaotic sea obtained from a simple 3d system without equilibrium," *International Journal of Bifurcation and Chaos*, vol. 26, no. 02, Article ID 1650031, 2016.

[27] A. Bayani, K. Rajagopal, A. J. M. Khalaf, S. Jafari, G. D. Leutcho, and J. Kengne, "Dynamical analysis of a new multistable chaotic system with hidden attractor: antimonotonicity, coexisting multiple attractors, and offset boosting," *Physics Letters A*, vol. 383, no. 13, pp. 1450–1456, 2019.

[28] B. Munmuangsaen, J. Clinton Sprott, W. J.-C. Thio, A. Buscarino, and L. Fortuna, "A simple chaotic flow with a continuously adjustable attractor dimension," *International Journal of Bifurcation and Chaos*, vol. 25, no. 12, Article ID 1530036, 2015.

[29] Q. Lai, B. Norouzi, and F. Liu, "Dynamic analysis, circuit realization, control design and image encryption application of an extended Lü system with coexisting attractors," *Chaos, Solitons & Fractals*, vol. 114, pp. 230–245, 2018.

[30] N. Wang, G. Zhang, and B. Han, "Bursting oscillations and coexisting attractors in a simple memristor-capacitor-based chaotic circuit," *Nonlinear Dynamics*, vol. 97, no. 4, 2019.

[31] H. Jia, W. Shi, L. Wang, and G. Qi, "Energy analysis of sprott-a system and generation of a new Hamiltonian conservative chaotic system with coexisting hidden attractors," *Chaos, Solitons & Fractals*, vol. 133, Article ID 109635, 2020.

[32] C. Li and J. C. Sprott, "Variable-boostable chaotic flows," *Optik*, vol. 127, no. 22, pp. 10389–10398, 2016.

[33] C. Li, J. Clinton Sprott, Y. Liu, Z. Gu, and J. Zhang, "Offset boosting for breeding conditional symmetry," *International Journal of Bifurcation and Chaos*, vol. 28, no. 14, Article ID 1850163, 2018.

[34] T. Lu, C. Li, S. Jafari, and F. Min, "Controlling coexisting attractors of conditional symmetry," *International Journal of Bifurcation and Chaos*, vol. 29, no. 14, Article ID 1950207, 2019.

[35] C. Li, J. Clinton Sprott, and H. Xing, "Hypogenetic chaotic jerk flows," *Physics Letters A*, vol. 380, no. 11-12, pp. 1172–1177, 2016.

[36] SiC. Wang, C.H. Wang, and C. Xu, "An image encryption algorithm based on a hidden attractor chaos system and the knuth–durstenfeld algorithm," *Optics and Lasers in Engineering*, vol. 128, Article ID 105995, 2020.

[37] E. Dong, M. Yuan, S. Du, and Z. Chen, "A new class of Hamiltonian conservative chaotic systems with multistability and design of pseudo-random number generator," *Applied Mathematical Modelling*, vol. 73, pp. 40–71, 2019.

[38] H. A. Eyad and J.-H. Fu, "Local feedback stabilization and bifurcation control, i. hopf bifurcation," *Systems & Control Letters*, vol. 7, no. 1, pp. 11–17, 1986.

[39] Y. Pei and G. Chen, "Hopf bifurcation control using nonlinear feedback with polynomial functions," *International Journal of Bifurcation and Chaos*, vol. 14, no. 05, pp. 1683–1704, 2004.

[40] D. Ding, X. Qian, W. Hu, N. Wang, and L. Dong, "Chaos and hopf bifurcation control in a fractional-order memristor-based chaotic system with time delay," *The European Physical Journal Plus*, vol. 132, no. 11, p. 447, 2017.

[41] C. C. Jahnke and F. E. C. Culick, "Application of bifurcation theory to the high-angle-of-attack dynamics of the *f*-14," *Journal of Aircraft*, vol. 31, no. 1, pp. 26–34, 1994.

[42] S. Liu, H. Ai, Z. Pang, Z. Lin, and D. Zhao, "Hopf bifurcation control of nonlinear electromechanical coupling main drive system of rolling mill," *The European Physical Journal Plus*, vol. 135, no. 4, p. 365, 2020.

[43] D. Hu and H. Cao, "Bifurcation and chaos in a discrete-time predator-prey system of Holling and Leslie type," *Communications in Nonlinear Science and Numerical Simulation*, vol. 22, no. 1-3, pp. 702–715, 2015.

[44] N. Shuichi, "Constant temperature molecular dynamics methods," *Progress of Theoretical Physics Supplement*, vol. 103, pp. 1–46, 1991.

[45] C. Li, J. Sun, T. Lu, and T. Lei, "Symmetry evolution in chaotic system," *Symmetry*, vol. 12, no. 4, p. 574, 2020.

[46] C. Li and J. Clinton Sprott, "Multistability in the lorenz system: a broken butterfly," *International Journal of Bifurcation and Chaos*, vol. 24, no. 10, Article ID :1450131, 2014.

[47] J. Sotomayor, L. Fernando Mello, and B. Denis de Carvalho, "Bifurcation analysis of the watt governor system," *Computational & Applied Mathematics*, vol. 26, no. 1, pp. 19–44, 2007.

WILEY | Hindawi

Research Article

Assisted Diagnosis of Alzheimer's Disease Based on Deep Learning and Multimodal Feature Fusion

Yu Wang ⓘ, Xi Liu, and Chongchong Yu

Beijing Key Laboratory of Big Data Technology for Food Safety, School of Artificial Intelligence,
Beijing Technology and Business University, Beijing 100048, China

Correspondence should be addressed to Yu Wang; wangyu@btbu.edu.cn

With the development of artificial intelligence technologies, it is possible to use computer to read digital medical images. Because Alzheimer's disease (AD) has the characteristics of high incidence and high disability, it has attracted the attention of many scholars, and its diagnosis and treatment have gradually become a hot topic. In this paper, a multimodal diagnosis method for AD based on three-dimensional shufflenet (3DShuffleNet) and principal component analysis network (PCANet) is proposed. First, the data on structural magnetic resonance imaging (sMRI) and functional magnetic resonance imaging (fMRI) are preprocessed to remove the influence resulting from the differences in image size and shape of different individuals, head movement, noise, and so on. Then, the original two-dimensional (2D) ShuffleNet is developed three-dimensional (3D), which is more suitable for 3D sMRI data to extract the features. In addition, the PCANet network is applied to the brain function connection analysis, and the features on fMRI data are obtained. Next, kernel canonical correlation analysis (KCCA) is used to fuse the features coming from sMRI and fMRI, respectively. Finally, a good classification effect is obtained through the support vector machines (SVM) method classifier, which proves the feasibility and effectiveness of the proposed method.

1. Introduction

Magnetic resonance imaging (MRI) is a medical imaging technology with rapid development in recent years. It has many advantages such as high contrast for soft tissues, high resolution, and noninvasive way. It is widely used in various types of cardiovascular and cerebrovascular diseases and has promoted the progress and development of contemporary medicine. At present, structural MRI (sMRI) and functional MRI (fMRI) are widely used in the diagnosis of Alzheimer's disease (AD).

A complete and clear intracranial anatomical structure through hierarchical scanning using sMRI can be obtained, which is helpful to analyze the morphological structure of brain gray matter, white matter, and cerebrospinal fluid and to determine whether a disease or injury exists. The brain structure imaging analysis of patients with AD and normal people (normal control, NC) has found that the gray matter volume of AD patients was significantly lower than that of normal people, and the gray matter in the hippocampus, temporal poles, and temporal islands also has significant shrinkage [1]. Comparing the different stages of AD patients, it is found that hippocampus atrophy is significant in the initial stage. Then, the inferior lateral area of the temporal lobe changes obviously, and finally, the frontal lobe begins to shrink [2]. fMRI is used to measure the changes in hemodynamics caused by neuronal activity which can show the location and extent of brain activation and can detect dynamic changes in the brain over a period of time.

The application of artificial intelligence (AI) in medical treatment has become a research hotspot for scholars at home and abroad [3, 4]. AI combined with machine learning methods is applied to medical image processing to obtain biomarkers and to assist doctors in making correct diagnoses. Deep learning is an important branch of machine learning, and its application in the field of medical imaging has attracted widespread attention. Ehsan Hosseini-Asl [5] and Adrien Payan [6] used 3D convolutional neural

networks and autoencoders to capture AD biomarkers. Zhenbing Liu [7] used a multiscale residual neural network to collect multiscale information on a series of image slices and to classify AD, mild cognitive impairment (MCI), and NC. Ciprian D. Billones [8] improved the VGG-16 network for constructing classification model of AD, MCI, and NC. Deep learning algorithms are also widely used in fMRI-assisted diagnosis of brain diseases. Junchao Xiao [9] used stacked automatic encoders and functional connection matrices to classify migraine patients and normal people. Meszlényi Regina [10] proposed a dynamic time normalization distance matrix, Pearson correlation coefficient matrix, warping path distance matrix, and convolutional neural network to realize AD-assisted diagnosis.

With the development of deep learning research, the number of network layers has been continuously deepened. The network structure has gradually become more and more complex, and the requirements for the hardware environment have gradually increased. In order to reduce the environmental demand of the model and to promote the application and improvement of the model, lightweight network operations such as MobileNet [11] and ShuffleNet [12] were born. In this paper, the ShuffleNet model is improved and an AD-assisted diagnosis model based on 3DShuffleNet is proposed, which directly uses the sMRI image preprocessed by the VBM-DARTEL [13] method and uses the deep features of the image to classify AD, MCI, and NC. The proposed method not only reduces the voting link of the slicing method to obtain the test results but also is more conducive to the promotion and application of the model in a low computing power environment because of the use of a lightweight network.

The high-dimensional and small sample characteristics of datasets often bring difficulties of classification and modeling such as fMRI data. Therefore, in this paper, the anatomical automatic labeling (AAL) template is used to calculate the functional link matrix after preprocessing of the original image. Functional connection matrix is a universal and effective method to analyze the correlation characteristics of each brain and can greatly reduce the data dimension. The feature redundancy in the functional connection matrix exists. Thus, data dimensionality reduction and feature extraction are usually improved. Principal component analysis network (PCANet) is an unsupervised deep learning feature extraction algorithm, which can effectively solve the problem of insufficient experimental samples. In this study, PCANet network is used to extract the matrix features and support vector machine (SVM) classifier is used to classify.

In addition, kernel canonical correlation analysis (KCCA) is used to fuse the features of two different modalities to achieve complementary information before the classifier is used, so as to reduce the impact of inherent defects because of a single-modal feature.

2. Data Introduction and Preprocessing

sMRI data are helpful for observing the changes in brain structure during the course of illness. fMRI reflects the influence of illness on brain function by detecting brain activity. The sMRI and fMRI images come from the Alzheimer's Disease Neuroimaging Initiative (ADNI), and in order to facilitate the fusion of the two modal data information, the experimental data are required to contain both types and the data are obtained at close times. At the same time, because early MCI and late MCI belong to the MCI process and have only slight differences, so they are regarded as the same category. Datasets including 34 cases of AD, 36 cases of MCI (including 18 cases of early MCI, 18 cases of late MCI), and 50 cases of NC were finally selected as experimental data.

VBM-DARTEL [13] method is used to preprocess sMRI images including segmentation, generating specific templates generation, flow fields generation, and normalization. The above preprocessing steps are all implemented using SPM8 software. Medical image processing software DPABI is used to preprocess fMRI images including the data removal of the first 10 time points, slice timing, realignment, normalization, smoothing, detrending, filtering, and extracting time series to calculate function link matrix. Figure 1(a) shows the coronal, sagittal, and cross-sectional views of gray matter images obtained by sMRI preprocessing, and Figure 1(b) is an example of the functional connection matrix obtained by preprocessing fMRI.

3. Method

The amount of experiment data in this paper is very small; in order to avoid as much as possible the overfitting phenomenon that often occurs in convolutional deep neural networks, this paper uses a lightweight network ShuffleNet with fewer parameters and PCANet that does not require feedback adjustment parameters to implement deep features extraction and classification.

3.1. MRI Feature Extraction and ShuffleNet. ShuffleNet is a deep learning network designed especially for mobile devices with limited computing power. It uses point-by-point grouping convolution and channel shuffling to achieve its high-efficiency architecture [12]. It reduces computational complexity while ensuring that the network still has a good classification performance. The network consists of one convolution layer, one maximum pooling layer, three sets of ShuffleUnit structure, one global pooling layer, and one full connection (FC) layer. Each group of ShuffleUnit structure consists of one ShuffleUnit module like Figure 2(b) and several ShuffleUnit modules like Figure 2(c) connected, and the number of series units is set by the Repeat parameter. ShuffleNet has outstanding performance in image classification [15] and has been applied to face recognition [16]. This network integrates the strengths of many classic networks. It inherits the bottleneck module in the classic deep learning network ResNet [14], as shown in Figure 2(a). It uses the idea of residual learning to speed up model convergence and enhance model performance. It combines MobileNet's deep capabilities resulting from Separate
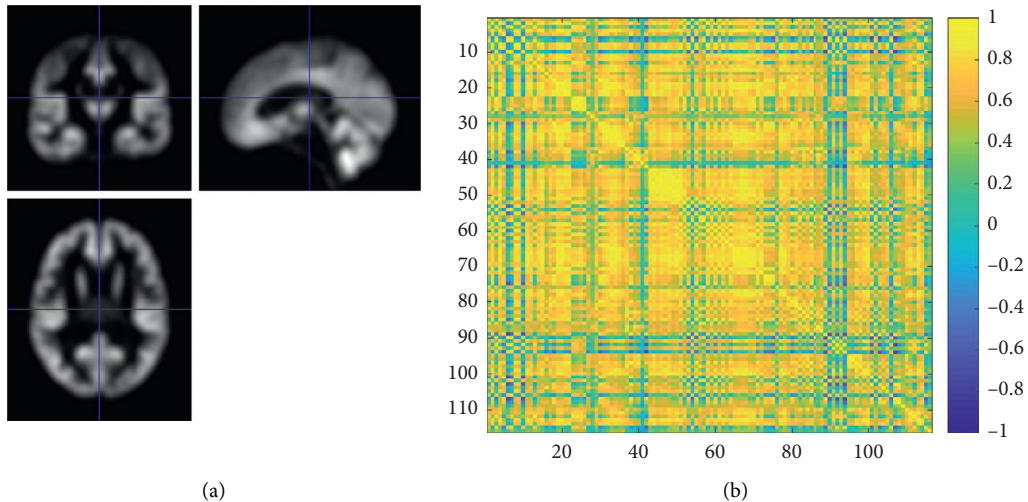
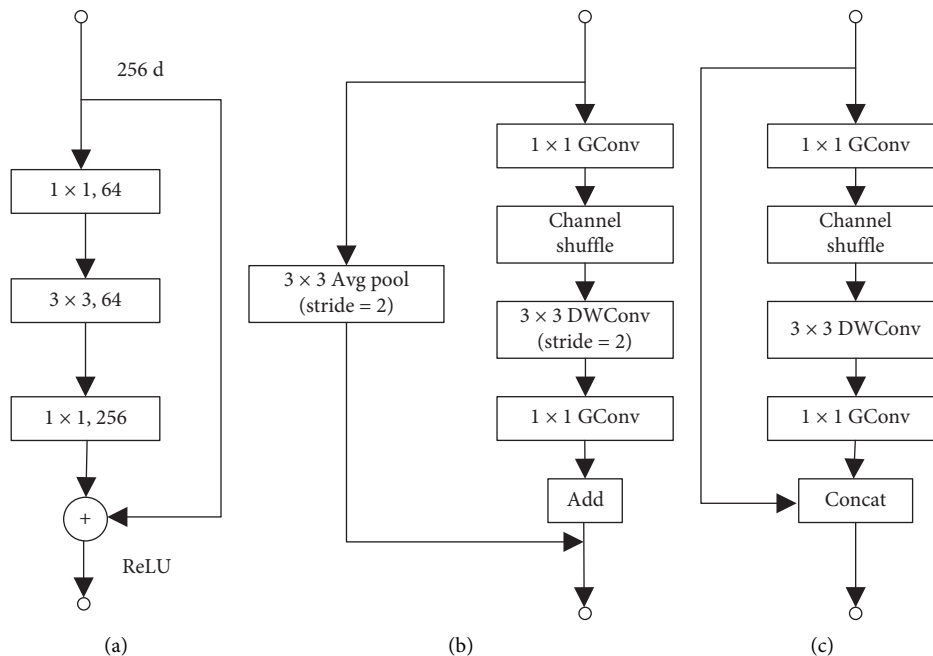FIGURE 1: Preprocessing results of (a) sMRI data and (b) fMRI data.

FIGURE 2: Bottleneck and ShuffleUnit [12, 14], (a) ResNet bottleneck, (b) ShuffleUnit1, and (c) ShuffleUnit2.

convolution and AlexNet [17] network grouping method to reduce computational complexity.

ShuffleUnit is shown in Figure 2, improved from bottleneck in the ResNet network, and the unit output uses the idea of residual learning. The residual learning unit learns the difference between the input layer and the output layer through the parameterized network layer during training process of the network. Reference [16] proves that residual learning is easier to train and classification accuracy of the model is higher than that which directly learns the mapping of input and output. ShuffleUnit not only uses the idea of summation to ensure the transmission of original information to the back layer but also proposes that the first unit

in each group of ShuffleUnit uses concat to increase the number of channels and to achieve the purpose of fusion of original information and global information.

The depth separable convolution mentioned by MobileNet is applied to the convolution of ShuffleUnit. Depth separable convolution splits the ordinary convolution process into two steps. First, each channel corresponding to a 3×3 convolution kernel is used to obtain a single channel feature map. Then, point-by-point convolution is used to combine full channel features. Depth separable convolution can obtain similar effects as ordinary convolution and at the same time greatly reduce the amount of calculation. The reduction factor of the calculation amount is shown in

$$\frac{H \times W \times 3 \times 3 \times C_{\text{in}} + H \times W \times C_{\text{in}} \times C_{\text{out}}}{H \times W \times C_{\text{in}} \times 3 \times 3 \times C_{\text{out}}} = \frac{1}{C_{\text{out}}} + \frac{1}{9}, \quad (1)$$

where $H \times W$ refers to the size of the feature map. C_{in} and C_{out}, respectively, represent the number of input channels and output channels of the convolutional layer.

The idea of grouped convolution was originally derived from the limitation of hardware resources when running the AlexNet network, and Hinton splits the information into two GPUs to run [17]. Considering that point-by-point convolution still has a large amount of calculation, ShuffleUnit adopts a grouping operation for point-by-point convolution to further reduce the amount of calculation. The reduction factor of the calculation amount is shown in formula (2). In order to strengthen the flow of information between groups, reduce the constraints between channels, and enhance the ability of information presentation, the channel shuffle method is used to realize information exchange between groups.

$$\frac{H \times W \times (\text{Cin}/g) \times (\text{Cout}/g) \times g}{H \times W \times \text{Cin} \times \text{Cout}} = \frac{1}{g}, \quad (2)$$

where g refers to the number of groups in point-by-point grouping convolution.

Most of the convolutional networks proposed at present are suitable for color images and use 2D convolution to extract image features. In order to adapt to the characteristics of the network, the slicing method is proposed in [5] and [6]. Although the slicing method is convenient for the training and application of existing 2D convolutional neural networks, the result can only represent the category of the corresponding slice of the brain, rather than the overall category. Therefore, the slicing method often requires the majority voting method to integrate the results of each part and further to evaluate the overall category. The process is complicated. In order to avoid the above-mentioned complicated process, the classification features of the entire sample are directly obtained, which facilitates subsequent fusion with fMRI features. Then, a 3D form of ShuffleNet is implemented, and it is also beneficial to retain more three-dimensional spatial information.

In 3DShuffleNet, the number of groups in grouped convolution is set to 3, and in order to adapt to the 3D structure of gray matter images, the 2D convolution is changed to 3D convolution. The parameters of the model structure are shown in Table 1.

Amyloid deposition and neurofibrillary tangles in the brain are typical pathological changes in patients with AD, which can cause brain nerve cell atrophy and death or abnormal signal transmission between cells. Experienced doctors can distinguish AD by observing the degree of atrophy of specific parts of the sMRI imaging. The gray matter of the brain is a dense part of neuronal cell bodies and is the center of information processing. Through it, the distribution and number of neuronal cells in the test patient can be analyzed to screen for AD. In this paper, the sMRI gray matter image obtained after preprocessing is read into this

TABLE 1: Model structure of 3DShuffleNet.

Layer	Ksize	Stride	Repeat	Output ($g = 3$)
Image				$1 * 121 * 145 * 121$
Conv1	$3 * 3 * 3$	2	1	$24 * 61 * 73 * 61$
MaxPool	$3 * 3 * 3$	2	1	$24 * 31 * 37 * 31$
Stage1		2,1	1,3	$240 * 16 * 19 * 16$
Stage2		2,1	1,7	$480 * 8 * 10 * 8$
Stage3		2,1	1,3	$960 * 4 * 5 * 4$
GlobalPool	$4 * 5 * 4$		1	$960 * 1 * 1 * 1$
FC			1	2

3DShuffleNet to obtain auxiliary diagnosis results, and the outputs of the penultimate layer and the inputs before the classification layer are regarded as classification features.

3.2. fMRI Feature Extraction. The changes in cerebral hemodynamics over a period of time are recorded in fMRI, so the characteristics of high-dimensional small samples are particularly prominent among them. How to effectively extract the information expressed by brain imaging and reduce the dimensionality has become the primary problem in establishing auxiliary diagnostic models. ALFF value analysis, functional connection matrix analysis, and local consistency analysis are included in the present fMRI data processing methods. Among them, the most common method is functional connection matrix. It measures the coordination and consistency of the work of two brain regions by calculating the Pearson correlation coefficient of the brain interval time series, and it can greatly reduce the data dimension. Because diseases can cause changes in the connection characteristics of certain brain areas, it retains the most AD diagnostic information. In this paper, the functional connection matrix obtained by fMRI preprocessing is used as the input of the auxiliary diagnosis network.

PCANet is a simple deep learning baseline proposed by Chang Tsung-Han [18] which consists of cascaded principal component analysis, binary hash, and block histogram and is widely used in face recognition [19], age evaluation [20], deception detection [21], and other fields. This network has good deep feature extraction capabilities. It can be roughly divided into three stages, among which the first and second stages are PCA convolution, and the third stage is the feature output stage [22].

In the first stage, PCA and convolution are used to achieve features. Suppose the number of input samples is N, the size of the sample matrix is $[m, n]$, and the size of the sliding window is $[k_1, k_2]$. $(m - k_1 + 1) \times (n - k_2 + 1)$ image blocks are obtained by sliding window as shown in the following equation:

$$X_i = \left[x_{i,1}, x_{i,2}, \ldots, x_{i,mn} \right] \in R^{k_1 k_2 \times (m-k_1+1)(n-k_2+1)}. \quad (3)$$

Then, the image matrix after removing the mean value of each dimension of all image blocks can be gotten by

$$\overline{X} = \left[\overline{X_1}, \overline{X_2}, \ldots, \overline{X_N} \right] \in R^{k_1 k_2 \times N (m-k_1+1)(n-k_2+1)}. \quad (4)$$

Assume that the number of convolution filters in the first step is L_1. PCA is used to learn the convolution filter, and the parameters of the convolution filter are

$$W_l^1 = \text{mat}_{k_1,k_2}\left(q_l\left(\overline{XX}^T\right)\right) \in R^{k_1 k_2}, \quad l = 1, 2, \ldots, L_1, \quad (5)$$

where $\text{mat}_{k,k}(q_l(\overline{XX}^T))$ represents the mapping from a vector of size $k1 \times k2$ to a matrix W_l^1 of size $[k1, k2]$ and $q_l(\overline{XX}^T)$ represents the eigenvector of the l-th principal component.

The second stage is similar to the first stage. Assume that the size of the second-stage filter is $[k_3, k_4]$ and the number is L_2. In the first stage, the output of the l-th convolution filter of the i-th image is

$$I_i^l = I_i * W_l^1, \quad (6)$$

where $l = 1, 2, \ldots, L_1$ and $i = 1, 2, \ldots, N$. The signal $*$ represents two-dimensional convolution.

Using the same operation like the first stage on the l-th convolution, the output of each sample is described as

$$\overline{X^l} = \left[\overline{X_1^l}, \overline{X_2^l}, \ldots, \overline{X_N^l}\right] \in R^{k_3 k_4 \times N (m-k_3+1)(n-k_4+1)}. \quad (7)$$

The results of each convolution kernel performing the operation shown in equation (7) are combined together; we can get

$$\overline{X} = \left[\overline{X^1}, \overline{X^2}, \ldots, \overline{X^{L_1}}\right] \in R^{k_3 k_4 \times L_1 N (m-k_3+1)(n-k_4+1)}. \quad (8)$$

Then, the convolution filter parameters can be obtained using the following equation:

$$W_r^2 = \text{mat}_{k_3,k_4}\left(q_r\left(\overline{XX}^T\right)\right) \in R^{k_3 k_4}, \quad r = 1, 2, \ldots, L_2. \quad (9)$$

The output of the second stage is

$$S_i^{l,r} = I_i^l * W_r^2, \quad (10)$$

where $r = 1, 2, ..., L_2$. In this way, each feature map of the input of the second stage produces L_2 outputs.

The third stage is the feature output stage which includes binary hash coding, block histograms for encoding, and downsampling operations.

The binarized image of outputted feature map in the second stage is obtained by the Heaviside function, and different weights are assigned to get the encoded decimal feature map as shown in the following equation:

$$T_i^l = \sum_{r=1}^{L_2} 2^{r-1} H\left(S_i^{l,r}\right), \quad (11)$$

where $H(.)$ represents the Heaviside function.

The feature map T is divided into several blocks with the same size, and histogram statistics are made for each block. All block histogram statistics are concatenated to obtain the output feature as described by

$$O_i = \left[B\left(T_i^1\right), B\left(T_i^2\right), \ldots, B\left(T_i^{L_1}\right)\right] \in R^{(2^{L_2})L_1 b}, \quad (12)$$

where $B(.)$ stands for block histogram statistics.

PCANet is applied to extract effective classification features of AD, and functional connection matrix is calculated as input, using linear SVM classifier to output auxiliary diagnosis results.

3.3. Multimodal Features Fusion Method.
sMRI and fMRI images have their own characteristics, which provide information for AD from different angles. The information can be complemented by feature fusion, so as to obtain a more accurate description of samples.

At present, there are few researches on feature fusion in the field of AD-assisted diagnosis and mainly through the concatenation of features to improve the diagnosis effect. In this paper, we take the features extracted from sMRI and fMRI data as the fusion object. Since the images are from the same subject and were obtained on very close dates, it can be considered that there are some certain correlations between the description of the disease in sMRI and fMRI, and the two can be fused by analyzing typical correlation relationship of two feature vectors. At the same time, considering that the correlation is not only linear but also nonlinear, these features from two modal data can be fused by KCCA [23] methods.

KCCA is similar to CCA. It is the promotion of the CCA method in kernel space. The difference is that the two sets of variables are first projected into high-dimensional space before CCA. Radial basis function (rbf) kernel function is usually chosen, as shown in equation (13), to realize the space mapping.

$$k\left(x_i, x_j\right) = \exp\left(-\mu\|x_i - x_j\|^2\right). \quad (13)$$

CCA [24] is a multivariate statistical analysis method which uses the correlation between the comprehensive variable pairs to reflect the overall correlation between the two sets of indicators. The specific implementation steps are as follows.

The first pair of linear combinations with the greatest correlation is found separately from each group of variables as typical variables and is described by

$$\begin{aligned} u_1 &= a_1^T Y, \\ v_1 &= b_1^T Z, \end{aligned} \quad (14)$$

where u_1 and v_1 represent typical variables and a_1 and b_1 are the canonical correlation coefficients.

The following constraints are required:

$$\begin{aligned} \text{Var}(u_1) &= a_1^T \text{Var}(Y)a_1 = 1, \\ \text{Var}(v_1) &= b_1^T \text{Var}(Z)b_1 = 1, \\ \max[\rho_{u_1 v_1}] &= \max[\text{cov}(u_1, v_1)] = \max[a_1^T \text{cov}(Y, Z)b_1], \end{aligned} \quad (15)$$

where Var represents the correlation coefficient matrix. $Y = [y_1, y_2, \ldots, y_n]$ and $Z = [z_1, z_2, \ldots, z_n]$, respectively,

represent a group of variables. $\text{cov}(Y, Z)$ represents the covariance matrix between the two groups of variables.

Secondly, the second pair of typical variables which are not related to the first pair of typical variables in this group are found, and it is a pair of linear combinations with the second largest correlation.

The process of finding canonical correlation variables is repeated, and the newly found canonical correlation variables are not correlated with the existing ones in the group until all the variables are extracted.

Assuming that Y and Z are sMRI data and fMRI data features, A and B are the corresponding kernel canonical correlation coefficients. Difference in the unit scale between the features of different modal data maybe exists. If the features of the two modalities are directly fused, the feature with a large unit scale will play a decisive role, while the function of the feature with a small scale may be ignored. In order to eliminate the influence of unit and scale differences between features and to achieve the goal of treating each dimension feature equally, the most common feature processing method, namely, z-score standardization, is used to map feature vectors to the same distribution.

$$x^* = \frac{x - \overline{x}}{\sigma}, \tag{16}$$

where $\overline{x}$ is the mean value of the data and σ is the standard deviation of the data.

Knowing that the several canonical correlation variables corresponding to each group of variables in KCCA are not correlated with each other, it can be known that the linear combination of the canonical correlation coefficients of the two groups of variables is also not correlated. The fusion of the two modal characteristics can be achieved by adding the canonical correlation variables corresponding to the two sets of variables as shown in the following equation:

$$F_1 = u + v = \begin{bmatrix} A^T & B^T \end{bmatrix} \begin{bmatrix} Y \\ Z \end{bmatrix}. \tag{17}$$

4. Experimental Setup and Model Evaluation

The experimental results in this paper are all obtained under the server equipped with Nvidia TITAN Xp GPU, 32 GB RAM, 256 GB SSD, 2 TB HDD, quad-core Intel Xeon E5-2620 v3 2.4 GHz processor, win10 system, and CUDA10.2 environment configuration. The experimental training set and testing set account for 70% and 30% of the data, respectively.

In sMRI feature extraction and classification experiments, the preprocessed gray matter images are input into the 3DShuffleNet network for training (classification). The model training batch size is set to 4. The Adam optimization algorithm is used. The weight decay value is set to 1e-3, the initial value of the learning rate is set to 1e-3, and it decays exponentially as the number of trainings increases. The total number of iterations is 50, and the attenuation rate is set to 0.9. The 3DShuffleNet model initializes the 3D convolution weights by the normal distribution method. The weights of

the BatchNorm3D layer are initialized to a fixed value of 1. The weights of the fully connected layer are initialized to a normal distribution with a mean value of 0 and a variance of 0.001. The bias values are all set to 0. In addition, in order to improve the reliability of the experimental results, the model in this paper and the comparative test model were repeatedly trained and tested for 10 times.

In fMRI feature extraction and classification experiments, by setting different size and number of PCA kernels and block size, the influence on the diagnosis results is explored.

In multimode data fusion experiment, we use the grid search method to adjust KCCA parameters. After that, the classification results of the proposed method in this paper and the experimental dataset in CCA and series fusion method are compared and analyzed.

In order to effectively evaluate the method proposed in this paper, Acc, Sen, Spec, Precision, Recall, F1 score, and AUC are calculated.

5. Experimental Results and Analysis

5.1. Classification Experiments of sMRI. In order to prove the superiority of the 3D model proposed in this paper, some classic models are compared, and the results on sMRI data using 3DShuffleNet are shown in Table 2.

It is found from Table 2 that the 3DShuffleNet proposed in this paper has significant advantages, and better classification results on AD versus NC and AD versus MCI are achieved. But the classification effect of MCI versus NC is poor. It is speculated that, on the one hand, because MCI is the early stage of the AD patient, the brain gray matter structure has not changed significantly, and the network is difficult to locate the disease characteristics. On the other hand, because the experimental samples are relatively scarce, the model is not fully trained. Similarly, because the difference between LMCI and EMCI is very slight, the result of LMCI versus EMCI is worst.

In addition, the complexity is evaluated with FLOPs and the number of floating-point multiplication adds. For proving the advantages of the 3DShuffleNet proposed in this paper over other networks, the experimental results of the proposed model on FLOPs are compared with those of the 3D forms of ResNet and DenseNet, which are widely used in image classification. 3DShuffleNet needs 0.79 GFLOPS of computational force, which is much smaller than the comparison models including 3DResNet network with 10 layers and 3DDenseNet network with 121 layers, which requires 38.97 and 89.71 GFLOPs. At the same time, the parameters amount of the network is obtained. 3DShuffleNet has 957.72 thousand parameters; 3DResNet with 10 layers and 3DDenseNet with 121 layers, respectively, have 14.36 and 11.24 million parameters. The proposed network has obtained relatively good classification results with a small computational cost.

5.2. Classification Experiments of fMRI. If the AAL template is used to calculate the function connection, a $90 * 90$ or

Table 2: Experimental results of sMRI data (%).

AD versus NC	Acc	Sen	Spec	Precision	Recall	f1-score	AUC
ResNet_10	80.4	77.0	82.7	74.9	77.0	75.8	80.9
DenseNet_121	74.0	53.0	88.0	77.1	53.0	61.0	79.5
3DShuffleNet	85.2	69.0	96.0	93.3	69.0	79.0	86.9
AD versus MCI	Acc	Sen	Spec	Precision	Recall	f1-score	AUC
ResNet_10	77.5	77.0	78.0	78.0	77.0	77.4	86.2
DenseNet_121	62.0	61.0	63.0	64.2	61.0	61.1	68.3
3DShuffleNet	84.0	84.0	84.0	84.9	84.0	84.1	91.9
MCI versus NC	Acc	Sen	Spec	Precision	Recall	f1-score	AUC
ResNet_10	64.8	38.0	82.7	61.6	38.0	45.8	65.5
DenseNet_121	53.6	52.0	54.6	47.5	52.0	47.1	55.5
3DShuffleNet	64.8	43.0	79.3	60.2	43.0	48.0	67.3
EMCI versus LMCI	Acc	Sen	Spec	Precision	Recall	f1-score	AUC
ResNet_10	54.0	56.0	52.0	53.7	56.0	54.1	65.2
DenseNet_121	54.0	28.0	80.0	62.5	28.0	36.7	48.2
3DShuffleNet	53.0	40.0	66.0	56.7	40.0	45.6	58.0

$116 * 116$ function connection matrix will be obtained, respectively, using 90 or 116 regions of cerebrum. Therefore two datasets with different sample sizes are obtained. The whole brain function connection matrix is selected as the experimental data, and the effects of three variables on the classification results are analyzed, respectively.

First of all, the impact of different PCA kernel sizes on the experimental results is compared and analyzed. The initial number of PCA kernels is set to $L1 = L2 = 8$, and the block size to 16. Because the data have unbalanced categories phenomenon, the average value of sensitivity and specificity is used as evaluation criterion. The detailed results are shown in Figure 3.

From Figure 3, we can see that, as the PCA kernel's size continues to increase, the classification result firstly becomes better and then worse. It is speculated that this phenomenon is related to the receptive field theory which is similar to traditional convolutional neural networks. The larger the receptive field is, the more image information can be obtained. So PCANet can obtain better expression ability. However, as the PCA kernel size continues to increase, the number of parameters soars, which reduces the computing efficiency.

Next, the impact of the number of PCA kernels on the classification results is discussed, and the results are shown in Figure 4. Considering that, in different classification combinations, the PCA kernel's size corresponding to the best classification effect is different, the size of PCA kernel in different classification combinations is set as $3 * 3$, $5 * 5$, $7 * 7$, and $3 * 3$, and the block size keeps unchanged.

The experimental results show that, in a certain range, the increase in the number of PCA kernels retains more data information as the dimension increases, which makes positioning of the disease more accurate. When the number of PCA kernels reaches a certain level, the experimental result decreases. The reason is that too many PCA kernels will cause the introduction of noise.
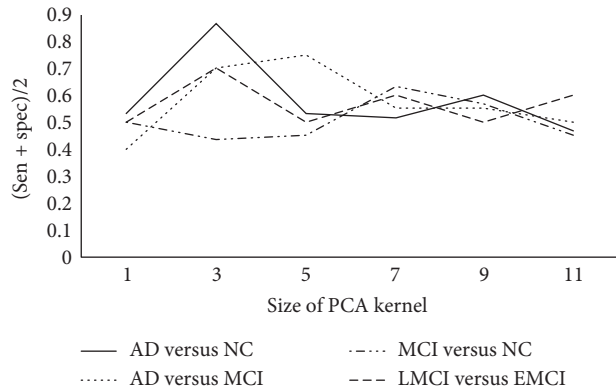

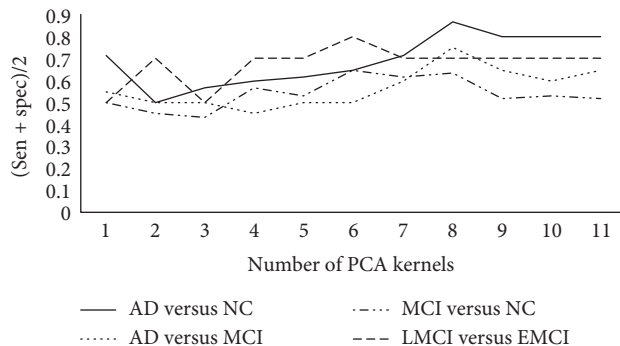Figure 3: Accuracy of different PCA kernel size.

Figure 4: Accuracy of different PCA kernel number.

Finally, the influence of block size (for histogram calculation) on the robustness of experimental results is analyzed. When the PCA kernel size is set to $3 * 3, 5 * 5, 7 * 7$, and $3 * 3$ and the number of PCA cores is set to 8, 8, 6, and 6, the experimental results in Figure 5 are obtained.

The results show that an appropriate block size provides better robustness, but blindly increasing the block size will sacrifice model performance. After the above-mentioned optimization method of control variables, the experimental results are shown in Table 3.

Considering that the size of the PCA kernel, the number of the PCA convolution kernels, and the block size of calculation histogram may affect each other, the grid search method is used for further experiments. The gradient of PCA kernel size is set as [3, 5, 7,...,11], and the gradient of the number of PCA kernels is [1, 2,...,11]. The side length of the block of histogram is set to a multiple of 4, and the maximum value is set to half of the side length of the function connection matrix. The experimental results are shown in Table 4.

The control variable method and the grid search method are used to adjust the parameters, and the global brain function connection matrix is used as the experimental data. It can be seen from Tables 3 and 4 that the grid search method is better than the control variable method in adjusting the parameters, because there is a close relationship between the three variables and they influence each other.
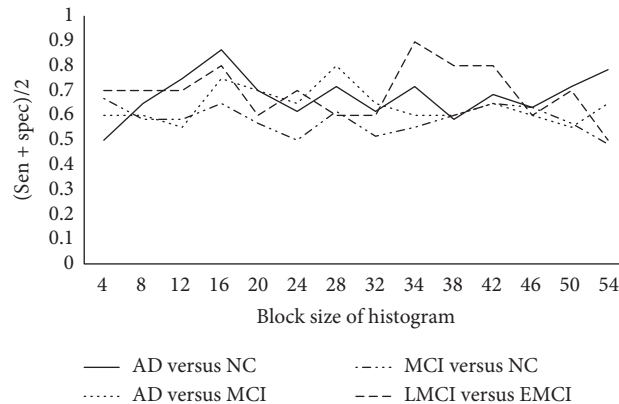
FIGURE 5: Accuracy of different block size.

TABLE 3: Experimental results of adjusting parameters by controlled variable method (%).

Class	Model	Acc	Sen	Spec	Precision	Recall	f1-score	AUC
AD versus NC	Global brain	88.0	80.0	93.3	88.9	80.0	84.2	88.7
AD versus MCI	Global brain	80.0	70.0	90.0	87.5	70.0	77.8	76.0
MCI versus NC	Global brain	68.0	60.0	73.3	60.0	60.0	60.0	66.7
LMCI versus EMCI	Global brain	90.0	80.0	100.0	100.0	80.0	88.9	96.0

TABLE 4: Experimental results of adjusting parameters by grid search method (%).

Class	Model	Acc	Sen	Spec	Precision	Recall	f1-score	AUC
AD versus NC	Cerebrum	84.00	80.0	86.7	80.0	80.0	80.0	86.0
AD versus MCI	Cerebrum	85.0	90.0	80.0	81.8	90.0	85.7	78.0
MCI versus NC	Cerebrum	76.0	80.0	73.3	66.7	80.0	72.7	84.0
EMCI versus LMCI	Cerebrum	100.0	100.0	100.0	100.0	100.0	100.0	100.0
AD versus NC	Global brain	88.0	80.0	93.3	88.9	80.0	84.2	88.7
AD versus MCI	Global brain	85.0	90.0	80.0	81.8	90.0	85.7	87.0
MCI versus NC	Global brain	80.0	80.0	80.0	72.7	80.0	76.2	83.3
EMCI versus LMCI	Global brain	100.0	100.0	100.0	100.0	100.0	100.0	100.0

The experimental results obtained from the global brain and cerebrum function connection matrix are compared and analyzed. In general, better performance can be obtained using the whole brain function connection matrix as an experimental sample. Among them, the classification accuracy of AD versus NC and MCI versus NC both increased by 4%, and the classification accuracy of AD versus MCI was equal. The presumed reason is that although AD focuses on appears in the part of cerebrum when one brain area is affected and the other brain areas are intact, the connection characteristics will also change. Therefore, by adding the cerebellum part to enrich the features information, a better diagnosis result can be obtained. In addition to the above results, we also apply our method to classify EMCI and LMCI. It can be seen from the results that the PCANet network is sensitive to the disease progresses from EMCI to LMCI, and functional characteristics changes in brain can be observed, which proves the feasibility and effectiveness of feature extraction using PCANet.

5.3. Classification Experiments of Feature Fusion. In this paper, the z-score standardization method is selected to normalize the features of the two modalities to the same scale, the KCCA feature fusion algorithm is selected to obtain the fused features of sMRI and fMRI, and SVM classifier is used for training and recognition.

In order to prove the effectiveness of the KCCA fusion algorithm, in addition to comparing the difference between the single-modal feature and the fusion feature classification effect, at the same time, the experimental results obtained by using CCA and the series method are compared. In the SVM classifier, the sigmoid kernel is used to train and obtain the recognition results. The experimental results are shown in Table 5. The sMRI features extracted by the 3DShuffleNet network are fused with the fMRI features extracted by the PCANet.

It can be seen from Table 5 that, compared with the CCA fusion method, the KCCA with rbf kernel has a significant improvement on the recognition results, and by this way,

TABLE 5: Comparison results of three feature fusion methods and single-modal method (%).

AD versus NC	Acc	Sen	Spec	Precision	Recall	f1-score	AUC
sMRI	88.0	70.0	100.0	100.0	70.0	82.4	86.0
fMRI	88.0	80.0	93.3	88.9	80.0	84.2	88.7
CCA	84.0	80.0	86.7	80.0	80.0	80.0	88.0
Series fusion	88.0	80.0	93.3	88.9	80.0	84.2	90.0
KCCA	96.0	100.0	93.3	90.9	100.0	95.2	99.3
AD versus MCI	**Acc**	**Sen**	**Spec**	**Precision**	**Recall**	**f1-score**	**AUC**
sMRI	90.0	90.0	90.0	90.0	90.0	90.0	97.5
fMRI	85.0	90.0	80.0	81.8	90.0	85.7	87.0
CCA	100.0	100.0	100.0	100.0	100.0	100.0	100.0
Series fusion	90.0	90.0	90.0	90.0	90.0	90.0	98.0
KCCA	100.0	100.0	100.0	100.0	100.0	100.0	100.0
MCI versus NC	**Acc**	**Sen**	**Spec**	**Precision**	**Recall**	**f1-score**	**AUC**
sMRI	76.0	50.0	93.3	83.3	50.0	62.5	63.3
fMRI	80.0	80.0	80.0	72.7	80.0	76.2	83.3
CCA	76.0	50.0	93.3	83.3	50.0	62.5	69.33
Series fusion	76.0	50.0	93.3	83.3	50.0	62.5	64.0
KCCA	100.0	100.0	100.0	100.0	100.0	100.0	100.0
LMCI versus EMCI	**Acc**	**Sen**	**Spec**	**Precision**	**Recall**	**f1-score**	**AUC**
sMRI	70.0	40.0	100.0	100.0	40.0	57.1	64.0
fMRI	100.0	100.0	100.0	100.0	100.0	100.0	100.0
CCA	100.0	100.0	100.0	100.0	100.0	100.0	100.0
Series fusion	80.0	80.0	80.0	80.0	80.0	80.0	72.0
KCCA	100.0	100.0	100.0	100.0	100.0	100.0	100.0

information complementary of two modal is realized. The KCCA algorithm considers the influence of nonlinear features during feature fusion, which makes the feature description more reasonable and enhances the identification ability of subsequent classifiers. This also explains why the effect of feature fusion using CCA is not satisfactory. Compared with the traditional serial fusion method, the KCCA fusion algorithm still has advantages in experiments.

6. Conclusions

Using deep learning algorithms to assist doctors in diagnosing AD has broad research prospects. Furthermore, the idea of features fusion can achieve an obvious improvement. In this paper, 3DShuffleNet is used to build an sMRI-assisted diagnosis model, and PCANet is used to build an fMRI-assisted diagnosis model. Both methods can achieve better results and can provide help on correct diagnosis and early detection of AD. At the same time, the features fusion of two kinds of data is realized, and compared with single modality, better classification results on multiple modalities are obtained. The addition of fMRI features not only further improves the diagnostic advantages of the sMRI-assisted diagnosis model on AD versus NC and AD versus MCI but

also avoids the disadvantages of sMRI on the MCI versus NC and LMCI versus EMCI experiments. In addition, multiple modalities methods overcome the shortcomings of single-modal recognition which cannot make full use of target features. The method proposed in this paper also has the characteristics of low requirements for equipment computing capabilities, which is helpful for its promotion in practical applications.

Data Availability

The data in this paper come from the Alzheimer's Disease Neuroimaging Initiative database, which is an open-source third-party database. The specific dataset of the experiment cannot be provided due to copyright reasons. For the experimental data in this paper, subjects who have both fMRI and sMRI are selected. The amount of experimental data is 34 cases of AD, 18 cases of early MCI, 18 cases of late MCI, and 50 cases of NC. ADNI database link: http://adni.loni.usc.edu/.

Conflicts of Interest

The authors declare that there are no conflicts of interest regarding the publication of this paper.

Acknowledgments

References

[1] G. Karas, P. Scheltens, S. Rombouts et al., "Precuneus atrophy in early-onset Alzheimer's disease: a morphometric structural MRI study," *Neuroradiology*, vol. 49, no. 12, pp. 967–976, 2007.

[2] Y. Chen, D. A. Wolk, J. S. Reddin et al., "Voxel-level comparison of arterial spin-labeled perfusion MRI and FDG-PET in Alzheimer disease," *Neurology*, vol. 77, no. 22, pp. 1977–1985, 2011.

[3] P. A. Feng, "Medical image classification algorithm based on weight initialization-sliding window fusion convolutional neural network," *Complexity*, vol. 2019, Article ID 9151670, 15 pages, 2019.

[4] F.-P. An and J.-E. Liu, "Medical image segmentation algorithm based on optimized convolutional neural network-adaptive dropout depth calculation," *Complexity*, vol. 2020, no. 7, 13 pages, Article ID 1645479, 2020.

[5] E. Hosseini-Asl, R. Keynto, and A. El-Baz, "Alzheimer's disease diagnostics by adaptation of 3D convolutional network," in *Proceedings of the 2016 IEEE International Conference on Image Processing (ICIP)*, Phoenix, Arizona, USA, September 2016.

[6] A. Payan and G. Montana, "Predicting Alzheimer's disease: a neuroimaging study with 3D convolutional neural networks," *Computer Science*, vol. 2, no. 4, pp. 355–362, 2015.

[7] C. B. Liu, X. S. Fang, H. H. Yang et al., "The diagnosis of Alzheimer's disease classification based on multi-scale

residual neutral network," *Journal of Shandong University (Engineering Science)*, vol. 48, no. 6, pp. 1–7, 2018.

[8] C. D. Billones, O. J. L. D. Demetria, D. E. D. Hostallero et al., "DemNet: A Convolutional Neural Network for the Detection of Alzheimer's Disease and Mild Cognitive Impairment," in *Proceedings of the TENCON 2016 - 2016 IEEE Region 10 Conference*, IEEE, Singapore, November 2016.

[9] J. C. Xiao, W. M. Zeng, J. J. Yang et al., "FMRI data analysis based on deeplearning in the application of migraine," *Computer Systems & Applications*, vol. 27, no. 4, pp. 249–253, 2018.

[10] R. Meszlényi, B. Krisztian, and Z. Vidnyánszky, "Resting state fMRI functional connectivity-based classification using a convolutional neural network architecture," *Frontiers in Neuroinformatics*, vol. 11, no. 10, pp. 61–86, 2017.

[11] A. G. Howard, M. Zhu, B. Chen et al., "MobileNets: efficient convolutional neural networks for mobile vision applications," 2017, https://arxiv.org/abs/1704.04861.

[12] X. Zhang, X. Zhou, M. Lin et al., "ShuffleNet: An Extremely Efficient Convolutional Neural Network for Mobile Devices," 2017, https://arxiv.org/abs/1707.01083.

[13] K. Zhou, J. Cai, and G. Q. Xiong, "VBM-DARTEL method applied in alzheimer's disease MRI image analysis," *Computer Applications and Software*, vol. 31, no. 3, pp. 462–446, 2014.

[14] K. He, X. Zhang, S. Ren et al., "Deep residual learning for image recognition," in *Proceedings of the IEEE conference on computer vision & pattern recognition*, Las Vegas, NV, USA, June 2016.

[15] Y. Liu, *Research on Image Content Automatic Classification Based on ShuffleNet Network model*, Henan University, Kaifeng, China, 2018.

[16] D. S. Yang and D. Ma, "Research on personnel safety management platform based on lightweight deep neural network," *Electric Power Information and Communication Technology*, vol. 17, no. 6, pp. 1–7, 2019.

[17] A. Krizhevsky, I. Sutskever, and G. E. Hinton, "ImageNet classification with deep convolutional neural networks," *Communications of the ACM*, vol. 60, no. 6, pp. 84–90, 2017.

[18] T.-H. Chan, K. Jia, S. Gao, J. Lu, Z. Zeng, and Y. Ma, "PCANet: a simple deep learning baseline for image classification?," *IEEE Transactions on Image Processing* vol. 24, no. 12, pp. 5017–5032, 2015.

[19] J. W. Huang and C. Yuan, "Weighted-PCANet for face recognition," *Journal of Mathematical Physics*, vol. 57, no. 2, pp. 4241–4248, 2015.

[20] D. P. Zheng, J. X. Du, W. T. Fan et al., *Deep Learning with PCANet for Human Age Estimation*, in *Proceedings of the International Conference on Intelligent Computing*, Lanzhou, China, August 2016.

[21] L. Y. Gu, W. Z. Lv, Y. Yang et al., "Deception detect study based on PCANet and support vector machine," *Acta Electronica Sinica*, vol. 44, no. 8, pp. 1969–1973, 2016.

[22] S. T. Li, B. Xiao, W. S. Li et al., "Diagnosis of Alzheimer's disease based on 3D-PCANet," *Computer Science*, vol. 45, no. 6, pp. 140–142, 2018.

[23] W. Zheng, X. Zhou, C. Zou, and L. Zhao, "Facial expression recognition using kernel canonical correlation analysis (KCCA)," *IEEE Transactions on Neural Networks*, vol. 17, no. 1, pp. 233–238, 2006.

[24] H. Harold, "Relations between two sets of variables," *Biometrika*, vol. 28, no. 3-4, pp. 321–377, 1936.